University of Calgary

PRISM Repository **https://prism.ucalgary.ca**

The Vault Open Theses and Dissertations

2019-01-03

Studies on Chemical and Electrochemical Stability of Li-stuffed Garnets for Next Generation Lithium Batteries

Hofstetter, Kyle

Hofstetter. K. (2019). Studies on Chemical and Electrochemical Stability of Li-stuffed Garnets for Next Generation Lithium Batteries (Master's thesis, University of Calgary, Calgary, Canada). Retrieved from https://prism.ucalgary.ca.

http://hdl.handle.net/1880/109418

Downloaded from PRISM Repository, University of Calgary

UNIVERSITY OF CALGARY

Studies on Chemical and Electrochemical Stability of Li-stuffed Garnets for Next Generation Lithium Batteries

by

Kyle Hofstetter

A THESIS

SUBMITTED TO THE FACULTY OF GRADUATE STUDIES

IN PARTIAL FULFILMENT OF THE REQUIREMENTS FOR THE

DEGREE OF MASTER OF SCIENCE

GRADUATE PROGRAM IN CHEMISTRY

CALGARY, ALBERTA

JANUARY, 2019

© Kyle Hofstetter 2019

Abstract

State-of-the-art lithium-ion batteries are responsible for the portable electronics revolution, enabling the use of cell phones, laptops, and other gadgets. However, even when fully developed, the energy density and safety are insufficient to meet the demands in electric vehicles and grid storage. Next generation batteries are projected to consist of a solid electrolyte, metallic Li anode and either O_2 or S cathode. Specifically, aqueous Li-O_2 batteries are very attractive due to their high theoretical energy density and increased safety. Among the solid Li-ion electrolytes, Li-stuffed garnets are deemed a very promising electrolyte due to their wide electrochemical window (> 6 V vs. Li/Li^+), chemical stability against metallic Li, and high ionic conductivity (~ 1 mS cm^{-1}) at room temperature. Even with these attributes, there is a lack of understanding towards the stability of Li-stuffed garnets with aqueous environment, CO_2, and moisture.

In this thesis, the chemical and electrochemical stability of various garnet-type ceramic electrolytes for next generation lithium batteries are reported. For next generation aqueous Li-O_2 batteries, garnet-type $Li_{6.5}La_{2.5}Ba_{0.5}ZrTaO_{12}$ was treated with H_2O, D_2O, 1 M LiOH, 1 M LiCl, or brine (0.1 M LiCl, 0.1 M $NaNO_3$, 0.1 M K_2CO_3) for up to 10 days to encourage a spontaneous H^+ or D^+/Li^+ ion-exchange reaction. In all cases, an increase in ionic conductivity was observed after the first 24 hours of submersion, while the crystal structure was unaltered. Samples were characterized with a variety of methods including powder X-Ray diffraction (PXRD), thermogravimetric analysis (TGA), scanning electron microscopy (SEM), transmission electron microscopy (TEM), and electrochemical impedance spectroscopy (EIS). With a more in depth understanding of the aqueous stability of lithium-garnets, $Li_{6.5}La_{2.5}Ba_{0.5}ZrTaO_{12}$ was employed as a protective Li anode material in a Li-O_2 cell, showing a promising and stable ~ 3 V.

Further gaseous stability of garnet-type $Li_7La_{2.75}Ca_{0.25}Zr_{1.75}Nb_{0.25}O_{12}$ with and without a thin Al_2O_3 layer under 3% H_2O and CO_2 rich atmospheres were investigated in regards to Li-ion conductivity. When exposed to CO_2 rich atmospheres, samples without the coating show an ~ 8 % increase in resistance over 1000 h, whereas coated samples only show ~ 1 % increase over the same environmental and time duration. However, in the presence of 3% H_2O, both coated and uncoated samples show large grain-boundary resistance, which is recoverable on removal of 3% H_2O. Complete stability characterization was carried out using EIS, PXRD, SEM, atomic force microscopy (AFM) and cyclic voltammetry (CV).

Acknowledgements

First and foremost, I would like to express my deepest gratitude to my supervisor, Dr. Venkataraman Thangadurai. Your endless support and encouragement allowed me to reach heights I never thought possible. You have been an amazing supervisor, without you this work would not have been possible. I would also like to thank my supervisory committee, Drs. Todd Sutherland and Greg Welch for your comments and suggestions on my research during annual meetings. I would also like to thank Dr. Kevin Thurbide for serving on my examination board.

A very special thanks to Dr. Alfred Samson, you continuously gave me the time and motivation to keep working, I feel lucky to have been given the opportunity to work with you. Dr. Suresh Mulmi (☕?), I will always be grateful for you encouraging me to start my graduate studies and helping every step of the way.

Thank you to all past and present members of the Thangadurai group. I would especially like to thank Sanoop Palakkathodi Kammampata for sharing many of the same challenges as me, helping me overcome all the little things. Thank you to Drs. Sumaletha Narayanan, Kalpana Singh, and Sourav Bag for answering all my out of the blue technical and research related questions. I thank Dr. Ali Darbandi for helping me with TEM and ED imaging and Dr. Chris Debuhr for help with the E-SEM images.

I would also like to thank all my friends and family who have supported me through my graduate studies adventure. Last but not least, Natalie Holland, you have been my rock each and every day. Without your support and encouragement, none of this would have been possible.

The US Department of Energy ARPA-E and Graduate Studies Scholarships at University of Calgary provided generous financial support that I greatly appreciate. I also acknowledge the

valuable help from our collaborators in the Eric Wachsman group form the University of Maryland Energy Research Center.

Dedication

I dedicate this work to my parents.

Table of Contents

Abstract ..... **ii**

Acknowledgements ..... **iv**

Dedication ..... **vi**

Table of Contents ..... **vii**

List of Tables ..... **x**

List of Figures ..... **xi**

List of Symbols ..... **xvi**

List of Abbreviations ..... **xvii**

Chapter One: Introduction **1**
- **1.1 Project overview** **1**
- **1.2 Research objectives** **3**
- **1.3 Thesis organization** **4**

Chapter Two: Background **6**
- **2.1 Introduction** **6**
- **2.2 Lithium-ion battery (LIB)** **7**
  - **2.2.1 Operation of lithium-ion batteries** **9**
  - **2.2.2 Challenges of LIBs** **11**
- **2.3 Next generation battery technology** **11**
- **2.4 Solid state lithium-ion conducting electrolytes** **13**
  - **2.4.1 NASICON and LISICON** **14**
    - ***2.4.1.1 NASICON*** ***14***
    - ***2.4.1.2 LISICON*** ***15***
  - **2.4.2 A-site deficient perovskite-type** **16**
  - **2.4.3 Lithium-stuffed Garnet-type** **17**
- **2.5 Stability of lithium-stuffed garnets in aqueous/moisture environments** **19**
- **2.6 Stability of lithium-stuffed garnets in CO_2 rich environments.** **22**
- **2.7 Stability of lithium-stuffed garnets with lithium.** **23**
  - **2.7.1. Chemical and electrochemical stability of lithium-garnets with lithium** **23**
  - **2.7.2 Lithium | Garnet interface** **24**

Chapter Three: Experimental methods **27**
- **3.1 Material preparation** **27**
  - **3.1.1 Material synthesis** **27**

3.1.2 Ion-exchanged samples ... **28**
3.2 Powder X-ray diffraction ... **29**
3.3 Electrochemical characterization ... **30**
3.3.1 Electrochemical impedance spectroscopy ... **30**
3.3.2 Cyclic voltammetry ... **33**
3.3.3 Hebb-Wagner polarization ... **34**
3.3.4 Plating and stripping DC polarization ... **35**
3.4 Thermogravimetric analysis and mass spectroscopy ... **35**
3.5 Microscopy imaging ... **36**
3.5.1 Scanning electron microscopy ... **36**
3.5.2 Transmission electron microscopy and selected area electron diffraction ... **37**
3.5.2 Atomic force microscopy ... **37**
3.6 Error considerations ... **38**

Chapter Four: Aqueous stability of lithium-garnet $Li_{6.5}La_{2.5}Ba_{0.5}ZrTaO_{12}$ ... **40**
4.1 General overview ... **40**
4.2 Results and discussion ... **41**
4.2.1 Condensed bulk $Li_{6.5}La_{2.5}Ba_{0.5}ZrTaO_{12}$ pellet stability in aqueous solution ... **41**
4.2.1.1 Phase characterization of protonated $Li_{6.5}La_{2.5}Ba_{0.5}ZrTaO_{12}$ in bulk pellet geometry ... ***41***
4.2.1.2 Ionic conductivity of protonated $Li_{6.5}La_{2.5}Ba_{0.5}ZrTaO_{12}$ in solution as a function of time ... ***43***
4.2.1.3 Ion-exchange extent in protonated $Li_{6.5}La_{2.5}Ba_{0.5}ZrTaO_{12}$ bulk pellets ... ***46***
4.2.1.4 Scanning electron images of protonated $Li_{6.5}La_{2.5}Ba_{0.5}ZrTaO_{12}$ bulk pellets ... ***52***
4.2.2 Powder form $Li_{6.5}La_{2.5}Ba_{0.5}ZrTaO_{12}$ stability in aqueous solution ... **54**
4.2.2.1 Phase characterization of protonated $Li_{6.5}La_{2.5}Ba_{0.5}ZrTaO_{12}$ powder form via X-Ray diffraction ... ***54***
4.2.2.2. Phase and crystallinity characterization of protonated $Li_{6.5}La_{2.5}Ba_{0.5}ZrTaO_{12}$ powder form via selected area electron diffraction and transmission electron microscopy ... ***56***
4.2.2.3 Ion-exchange extent in protonated $Li_{6.5}La_{2.5}Ba_{0.5}ZrTaO_{12}$ in powder form ... ***58***
4.3 Summary ... **59**

Chapter Five: Electrochemical stability of lithium garnets $Li_{6.5}La_{2.5}Ba_{0.5}ZrTaO_{12}$ and $Li_7La_{2.75}Ca_{0.25}Zr_{1.75}Nb_{0.25}O_{12}$ ... **60**
5.1 General overview ... **60**
5.2 Results and discussion ... **61**
5.2.1 Lithium plating and stripping across $Li_{6.5}La_{2.5}Ba_{0.5}ZrTaO_{12}$ and area specific resistance ... **61**
5.2.1.1 Plating and stripping lithium across $Li_{6.5}La_{2.5}Ba_{0.5}ZrTaO_{12}$ ... ***61***

5.2.1.2 Area specific resistance of lithium | $Li_{6.5}La_{2.5}Ba_{0.5}ZrTaO_{12}$ interface 63
5.2.2 $Li_{6.5}La_{2.5}Ba_{0.5}ZrTaO_{12}$ as a protective layer in aqueous Li-O_2 cells 65
5.2.3 Ionic and Electronic conductivity of $Li_7La_{2.75}Ca_{0.25}Zr_{1.75}Nb_{0.25}O_{12}$ 68
5.2.3.1 Ionic conductivity of LLCZN *68*
5.2.3.2 Electronic conductivity of LLCZN *70*
5.2.3.3 Electrochemical Stability Windows of $Li_7La_{2.75}Ca_{0.25}Zr_{1.75}Nb_{0.25}O_{12}$. *72*
5.3 Summary 73

Chapter Six: Gaseous stability of lithium-garnet $Li_7La_{2.75}Ca_{0.25}Zr_{1.75}Nb_{0.25}O_{12}$ 74
6.1 General overview 74
6.2 Results and discussion 75
6.2.1 Ionic stability of $Li_7La_{2.75}Ca_{0.25}Zr_{1.75}Nb_{0.25}O_{12}$ under CO_2 77
6.2.2 Ionic stability of $Li_7La_{2.75}Ca_{0.25}Zr_{1.75}Nb_{0.25}O_{12}$ under 3% H_2O 79
6.2.3 Ionic stability of $Li_7La_{2.75}Ca_{0.25}Zr_{1.75}Nb_{0.25}O_{12}$ under CO_2 and 3% H_2O 81
6.2.4 Morphology and topography studies of $Li_7La_{2.75}Ca_{0.25}Zr_{1.75}Nb_{0.25}O_{12}$ after CO_2 and humidity exposure 82
6.2.4.1 Topography imaging of $Li_7La_{2.75}Ca_{0.25}Zr_{1.75}Nb_{0.25}O_{12}$ in ambient air *82*
6.2.4.2 In-situ topography studies of $Li_7La_{2.75}Ca_{0.25}Zr_{1.75}Nb_{0.25}O_{12}$ under 3% H_2O *84*
6.2.4.3 In-situ scanning electron microscopy studies of $Li_7La_{2.75}Ca_{0.25}Zr_{1.75}Nb_{0.25}O_{12}$ under humidity. *85*
6.3 Summary 86

Chapter Seven: Conclusions and future work 87
7.1 Conclusions 87
7.1.1 Conclusions on aqueous stability of lithium-garnet $Li_{6.5}La_{2.5}Ba_{0.5}ZrTaO_{12}$ 87
7.1.2 Conclusions on electrochemical stability of lithium garnets $Li_{6.5}La_{2.5}Ba_{0.5}ZrTaO_{12}$ and $Li_7La_{2.75}Ca_{0.25}Zr_{1.75}Nb_{0.25}O_{12}$ 88
7.1.2.1 Electrochemical stability of $Li_{6.5}La_{2.5}Ba_{0.5}ZrTaO_{12}$ *88*
7.1.2.2 Electrochemical stability of $Li_7La_{2.75}Ca_{0.25}Zr_{1.75}Nb_{0.25}O_{12}$ *88*
7.1.3 Conclusions on gaseous stability of lithium-garnet $Li_7La_{2.75}Ca_{0.25}Zr_{1.75}Nb_{0.25}O_{12}$ 88
7.2 Future work 89

References 91

Appendix: Copyrights 103

List of Tables

Table 2.1 Comparison of popular primary and secondary battery chemistries. [1, 2] 7

Table 2.2 Comparison of current commercially available Li-ion cathode materials.[11] 9

Table 2.3 Summary of proton-exchanged and chemical stability of lithium-stuffed garnet. Reprinted (adapted) with permission from Hofstetter, K.; Samson, A.J.; Narayanan, S.; Thangadurai, V. *J. Power Sources* 2018, *390*, 297-312. Copyright 2018 Elsevier. 20

Table 2.4 Li metal cycling/electrochemical stability studies with Li-garnet electrolytes. Reprinted (adapted) with permission from Hofstetter, K.; Samson, A.J.; Narayanan, S.; Thangadurai, V. *J. Power Sources* 2018, *390*, 297-312. Copyright 2018 Elsevier. 25

Table 4.1 Summary of proton-exchange after $Li_{6.5}La_{2.5}Ba_{0.5}ZrTaO_{12}$ is soaked in aqueous solution, based on TGA results in Figure 4.12. 58

List of Figures

Figure 1.1 Comparison of select battery chemistries in terms of volumetric and gravimetric energy densities. [4] 2

Figure 1.2 Suggested architecture of an aqueous Li-O_2 battery cell. 3

Figure 2.1 Operation of a rechargeable lithium-ion battery with a lithiated graphite anode (Li_xC_6), lithium iron phosphate ($LiFePO_4$) cathode and organic electrolyte. 10

Figure 2.2 Comparison of energy densities of current commercially available batteries to proposed next generation batteries.[1, 15] 12

Figure 2.3 Spider plots of the performance and stability of various solid electrolyte materials.[17] 14

Figure 2.4 Typical crystal structure of NASICON-type with the formula $LiM_2(PO_4)_3$. Space group: *P1*, $a = b = c = 9.0581$ *Å*. [23] 15

Figure 2.5. Idealized crystal structure of LISICON, $Li_{14}Zn(GeO_4)_4$. Space group: *Pnma*, a = 10.828 Å, b = 6.251 Å, c = 5.14 Å.[25] 16

Figure 2.6 Idealized structure of Li-ion conductive perovskite, (Li,La,□)TiO_3. Space group: Pm3m, a = 3.8 Å.[26] 17

Figure 2.7 Idealized cubic lithium-stuffed garnet crystal structure, $Li_5La_3M_2O_{12}$. Space group Ia3d, a = 12.7943 Å.[31] 18

Figure 2.8 Doping strategies of lithium-garnet materials to increase ionic mobility, structural stability and electrochemical stability. Green boxes indicate the parent Li_5 and Li_7 phases and blue are doped variants. 19

Figure 2.9 Crystal structure of $Li_{5-x}H_xLa_3M_2O_{12}$ (M = Nb or Ta), full unit cell representation. M = teal polyhedra, La = purple sphere, Li1 site = pink sphere, Li2 = blue sphere, and H = green sphere. Zoom illustrates a portion of the structure $Li_{5-x}H_xLa_3M_2O_{12}$ showing both distorted octahedral Li1 site (pink) and tetrahedral Li2 site (blue). Reprinted with permission from Hofstetter, K.; Samson, A.J.; Narayanan, S.; Thangadurai, V. J. Power Sources 2018, 390, 297-312. Copyright 2018 Elsevier. 21

Figure 2.10 Schematic diagram showing the reaction of $Li_7La_3Zr_2O_{12}$ garnet exposed to humid air (left) followed by lithium carbonate formation (right). Reprinted with permission from Hofstetter, K.; Samson, A.J.; Narayanan, S.; Thangadurai, V. *J. Power Sources* 2018, *390*, 297-312. Copyright 2018 Elsevier. 23

Figure 2.11 Lithium wettability onto the garnet surface. The nonwetting surface leaves lithium in point contact with the garnet surface, where the wetting surface allows lithium to be in full contact with the garnet surface.[5, 35] 26

Figure. 3.1 Schematic reaction pathway of solid-state (ceramic) synthesis of lithium-garnets. ...28

Figure 3.2 Schematic of X-ray diffraction of beams 1 and 2 diffracting off crystal planes A and B, separated by a spacing d. Bragg's law must be satisfied for diffracted beams 1' and 2' and occur. ...30

Figure 3.3. a) Schematic representation of electroceramic with Au blocking electrodes. b) Simulated Nyquist plot highlighting bulk, grain boundary, and electrode contributions. Inset shows equivalent circuit $(R_BCPE_B)(R_{GB}CPE_{GB})C_E$. ...32

Figure 3.4. a) Schematic representation of electroceramic with Li reversible electrodes. b) Simulated Nyquist plot highlighting bulk, grain boundary, and interfacial charge transfer contributions. Inset shows equivalent circuit $(R_BCPE_B)(R_{GB}CPE_{GB})(R_ICPE_I)$. ...32

Figure 3.5. Comparison of total Li-ion conductivity of $Li_7La_3Zr_2O_{12}$ garnet-type materials reported in literature.[34, 76-79] ...39

Figure 4.1 Powder X-ray diffraction (PXRD) patterns of $Li_{6.5}La_{2.5}Ba_{0.5}ZrTaO_{12}$ sample after soaking in as-prepared, water, D_2O, 1 M LiOH, and 1 M LiCl for 5 days. For comparison simulated PXRD of the parent, $Li_5La_3Nb_2O_{12}$ garnet phase is shown in (f). Reprinted (adapted) with permission from Hofstetter, K.; Samson, A.J.; Thangadurai, V. *Solid State Ionics* 2018, 318, 71-81. Copyright (2018), with permission from Elsevier [OR APPLICABLE SOCIETY COPYRIGHT OWNER]...42

Figure 4.2 Powder X-ray diffraction (PXRD) patterns of $Li_{6.5}La_{2.5}Ba_{0.5}ZrTaO_{12}$ sample before and after soaking in brine (0.1 M LiCl, 0.1 M $NaNO_3$, 0.1 M K_2CO_3) solution for 10 days. Simulated $Li_5La_3Nb_2O_{12}$ garnet phase shown for comparison...43

Figure 4.3. a) Scanning electron micrograph of cured porous Au paste on lithium-garnet, $Li_{6.5}La_{2.5}Ba_{0.5}ZrTaO_{12}$. b) Schematic representation of the symmetric aqueous cell used for daily impedance measurements. Reprinted (adapted) with permission from Hofstetter, K.; Samson, A.J.; Thangadurai, V. *Solid State Ionics* 2018, 318, 71-81. Copyright (2018), with permission from Elsevier [OR APPLICABLE SOCIETY COPYRIGHT OWNER]...44

Figure 4.4 Variation of electrical conductivity obtained at 1 MHz for $Li_{6.5}La_{2.5}Ba_{0.5}ZrTaO_{12}$ under water, D_2O, 1 M LiOH and 1 M LiCl at room temperature. Reprinted (adapted) with permission from Hofstetter, K.; Samson, A.J.; Thangadurai, V. *Solid State Ionics* 2018, 318, 71-81. Copyright (2018), with permission from Elsevier [OR APPLICABLE SOCIETY COPYRIGHT OWNER]. ...45

Figure 4.5 Variation of electrical conductivity obtained from total resistance for $Li_{6.5}La_{2.5}Ba_{0.5}ZrTaO_{12}$ in brine (0.1 M LiCl, 0.1 M $NaNO_3$, 0.1 M K_2CO_3) solution for 10 days. ...46

Figure 4.6 TGA curves of LLBZT after the chemical stability test using the solutions employed in AC impedance spectroscopy study. Samples heated at 5 °C min^{-1} under 50/50 N_2/Air. For comparison, TGA of the as-prepared sample is also shown. Asterisks (*) indicate temperatures at which tandem in-situ variable temperature PXRD were performed. Reprinted (adapted) with permission from Hofstetter, K.; Samson, A.J.; Thangadurai, V. *Solid State Ionics* 2018, 318, 71-81. Copyright (2018), with permission from Elsevier [OR APPLICABLE SOCIETY COPYRIGHT OWNER]. 49

Figure 4.7 a) TGA curves of LLBZT powder after immersing in water for 168 h. Sample heated at 10 ^oC min^{-1} under air. Insets b) and c) show ionic current response from mass spectroscopy for water (100-550 ^oC) and CO_2 (500-750 ^oC), respectively. 50

Figure 4.8 In-situ variable temperature powder X-ray diffraction (PXRD) patterns of $Li_{6.5}La_{2.5}Ba_{0.5}ZrTaO_{12}$ sample after soaking in (a) deionized water, (b) D_2O, (c) 1 M LiOH, and (d) 1 M LiCl for 5 days. For comparison, empty sample holder XRD pattern is shown in (e). Reprinted (adapted) with permission from Hofstetter, K.; Samson, A.J.; Thangadurai, V. *Solid State Ionics* 2018, 318, 71-81. Copyright (2018), with permission from Elsevier [OR APPLICABLE SOCIETY COPYRIGHT OWNER]. 51

Figure 4.9 Typical scanning electron microscopy (SEM) images of $Li_{6.5}La_{2.5}Ba_{0.5}ZrTaO_{12}$ after and before the chemical stability tests. (1) as-prepared, (2) water, (3) D_2O, (4) 1 M LiOH, and (5) 1 M LiCl. Images (1a)–(5a) show the higher magnification of (1)–(5), respectively. Reprinted (adapted) with permission from Hofstetter, K.; Samson, A.J.; Thangadurai, V. *Solid State Ionics* 2018, 318, 71-81. Copyright (2018), with permission from Elsevier [OR APPLICABLE SOCIETY COPYRIGHT OWNER]. 53

Figure 4.10 Powder X-ray diffraction (PXRD) patterns of $Li_{6.5}La_{2.5}Ba_{0.5}ZrTaO_{12}$ sample after soaking in respective solutions for 168 h. (*) indicates peaks associated with sample holder contributions. 55

Figure 4.11 HR-TEM images and SAED patterns of $Li_{6.5}La_{2.5}Ba_{0.5}ZrTaO_{12}$ of a) As-prepared sample and b) after soaking in H_2O for 168 h. c) Simulated electron diffraction of Ia3d cubic lithium garnet crystal structure along the [111] zone axis. 57

Figure 4.12 Thermogravimetric analysis of $Li_{6.5}La_{2.5}Ba_{0.5}ZrTaO_{12}$ sample after soaking in respective solutions for 168 h, samples heated at 10 °C min^{-1} under 50/50 N_2/Air. 58

Figure 5.1 Schematic of $Li_{6.5}La_{2.5}Ba_{0.5}ZrTaO_{12}$ symmetric lithium circle cell. Reprinted (adapted) with permission from Hofstetter, K.; Samson, A.J.; Thangadurai, V. *Solid State Ionics* 2018, 318, 71-81. Copyright (2018), with permission from Elsevier [OR APPLICABLE SOCIETY COPYRIGHT OWNER]. 62

Figure 5.2. Lithium plating-stripping voltage hysteresis of the symmetric crucible cell shown in Figure 5.1. Reprinted (adapted) with permission from Hofstetter, K.; Samson, A.J.; Thangadurai, V. *Solid State Ionics* 2018, 318, 71-81. Copyright (2018), with permission from Elsevier [OR APPLICABLE SOCIETY COPYRIGHT OWNER]. 62

Figure 5.3. Arrhenius plot of LLBZT under ambient air. Reprinted (adapted) with permission from Hofstetter, K.; Samson, A.J.; Thangadurai, V. *Solid State Ionics* 2018, 318, 71-81. Copyright (2018), with permission from Elsevier [OR APPLICABLE SOCIETY COPYRIGHT OWNER].....64

Figure 5.4. Open circuit Nyquist plot of Li|LLBZT|Li symmetric cell. Reprinted (adapted) with permission from Hofstetter, K.; Samson, A.J.; Thangadurai, V. *Solid State Ionics* 2018, 318, 71-81. Copyright (2018), with permission from Elsevier [OR APPLICABLE SOCIETY COPYRIGHT OWNER]. 64

Figure 5.5 Schematic representation of lithium | LLBZT | aqueous. Reprinted (adapted) with permission from Hofstetter, K.; Samson, A.J.; Thangadurai, V. *Solid State Ionics* 2018, 318, 71-81. Copyright (2018), with permission from Elsevier [OR APPLICABLE SOCIETY COPYRIGHT OWNER]. 65

Figure 5.6 Open circuit voltage of lithium|LLBZT|0.1 M LiOH, lithium|LLBZT|1 M LiOH, and lithium|LLBZT|1 M LiCl cells as a function of time. Reprinted (adapted) with permission from Hofstetter, K.; Samson, A.J.; Thangadurai, V. *Solid State Ionics* 2018, 318, 71-81. Copyright (2018), with permission from Elsevier [OR APPLICABLE SOCIETY COPYRIGHT OWNER]. 67

Figure 5.7 Open circuit voltage after intentional short circuit of cells in Figure 5.5. Reprinted (adapted) with permission from Hofstetter, K.; Samson, A.J.; Thangadurai, V. *Solid State Ionics* 2018, 318, 71-81. Copyright (2018), with permission from Elsevier [OR APPLICABLE SOCIETY COPYRIGHT OWNER]. 67

Figure 5.8 Impedance spectra of LLCZN at 25 ^{o}C. The inset shows the data at high frequencies and the equivalent circuit model used to obtain the different resistance contributions. The simulated medium semicircle is shown in red solid line. Reproduced (adapted) with permission from *J. Electrochem. Soc.*, 165, A2303 (2018). Copyright 2018, The Electrochemical Society. 69

Figure 5.9 Arrhenius plots of total conductivity of LLCZN Reproduced (adapted) with permission from *J. Electrochem. Soc.*, 165, A2303 (2018). Copyright 2018, The Electrochemical Society. 69

Figure 5.10 Time dependences of the current upon application of voltages 0.5–6 V vs. Li at 25 ^{o}C under argon. 71

Figure 5.11 Applied bias (V) vs. steady state electronic current (I) curve to calculate the electronic resistance using Ohm's law. 71

Figure 5.12 Cyclic voltammetry profile of LLCZN under argon at 25 ^{o}C. Au was used as the working electrode, whereas lithium was the counter and reference.....73

Figure 6.1 Schematic representation of in-situ impedance setup. 75

Figure 6.2 XRD diffraction patterns of inhouse made $Li_7La_{2.75}Ca_{0.25}Zr_{1.75}Nb_{0.25}O_{12}$ and as-received $Li_7La_{2.75}Ca_{0.25}Zr_{1.75}Nb_{0.25}O_{12}$ with Al_2O_3 coating, parent $Li_5La_3Nb_2O_{12}$ (PDF No.: 45-0109) shown for reference. 76

Figure 6.3 (a) Arrhenius plot of LLCZN without coating (blue square) synthesized via solid-state method at the University of Calgary. LLCZN with ALD coating (red circle) synthesized via sol-gel method at University of Maryland. Both samples have an activation energy of ~0.37 eV and conductivities of about 1 x 10^{-4} S cm at room temperature. Inset shows typical Nyquist plot of ALD-LLCZN (red circle at 28 ^oC) and LLCZN (blue 21 ^oC). (b) and (c) Scanning electron microscopy images of fracture cross-section of LLCZN pellet synthesized via solid-state and sol-gel methods, respectively. 77

Figure 6.4 Impedance spectra of $Li_7La_{2.75}Ca_{0.25}Zr_{1.75}Nb_{0.25}O_{12}$ under 400 ppm CO_2/N_2 for 100 h for a) uncoated and b) Al_2O_3 coated. 78

Figure 6.5. Summary of LLCZN impedance in all CO_2 concentrations for (a) uncoated (b) Al_2O_3 coated up to 3000 ppm CO_2. (c) and (d) show normalized impedance up to pure CO_2 for the uncoated and coated samples, respectively. 79

Figure 6.6. Nyquist plots of a) uncoated and b) coated LLCZN samples under dry Ar (black square), 95 h 3% H_2O (blue circle), and upon recovery with 93 h dry Ar (pink triangle). Coated samples exposed to 3% H_2O were fit using $R_b(CPE_{gb}R_{gb})CPE_e$ equivalent circuit, red line shows fit. 80

Figure 6.7. Summary of total resistance of samples in dry and humidified Ar for uncoated a) and coated b). 81

Figure 6.8. Overview of total ionic resistance of a) uncoated and b) coated LLCZN samples when alternated between humidified and CO_2 rich environments. 82

Figure 6.9. AFM imaging of (a-d) uncoated and (e-h) ALD-coated sample. (a) and (e) shows the observed images after every hour of exposure in ambient air of uncoated and ALD-coated samples, respectively. The samples were also left overnight and imaged the following day (after 22 h). 83

Figure 6.10. AFM imaging of (a-c) uncoated and (d-f) ALD-coated sample. (a) and (d) shows the observed images after every hour of exposure in 3% H_2O/N_2 of uncoated and ALD-coated samples, respectively. 84

Figure 6.11 In-situ scanning electron microscopy images of LLCZN in a humid atmosphere. ...85

List of Symbols

Symbol	Unit	Definition
E_a	eV	Activation energy
N_A	mol^{-1}	Avogadro's number
a	cm^2	Area
k	$J\ K^{-1}$	Boltzmann Constant
C	F	Capacitance
σ	$S\ cm^{-1}$	Conductivity
I	A	Current
F	$C\ mol^{-1}$	Faradays constant
f	Hz	Frequency
R	$J\ K^{-1}\ mol^{-1}$	Gas Constant
$Z^{//}$	Ω	Imaginary component of impedance
Z	Ω	Impedance
l	cm	Length
V_{oc}	V	Open circuit voltage
θ	Degree	Phase angle
E	V	Potential
ω	$Rad\ s^{-1}$	Radial frequency
$Z^{/}$	Ω	Real component of impedance
R	Ω	Resistance
ρ	Ω cm	Resistivity
T	^oC or K	Temperature
λ	Å	Wavelength

List of Abbreviations

AC	Alternating current
AFM	Atomic force microscopy
ALD	Atomic layer deposition
CE	Counter electrode
CPE	Constant phase element
CV	Cyclic voltammetry
DC	Direct current
DMC	Dimethyl carbonate
EC	Ethylene carbonate
ED	Electron diffraction
EIS	Electrochemical impedance spectroscopy
E-SEM	Environmental scanning electron microscope
ESW	Electrochemical stability window
FTIR	Fourier transform infrared spectroscopy
HRTEM	High resolution transmission electron microscopy
LIB	Lithium ion battery
LISICON	Lithium superionic conductor
LLT	Lithium lanthanum titanate
LLCZN	$Li_7La_{2.75}Ca_{0.25}Zr_{1.75}Nb_{0.25}O_{12}$
LLBZT	$Li_{6.5}La_{2.5}Ba_{0.5}ZrTaO_{12}$
LLZO	$Li_7La_3Zr_2O_{12}$
NASICON	Sodium superionic conductor
PDF	Powder diffraction file
PXRD	Powder X-ray diffraction
RE	Reference electrode
Redox	Reduction-oxidation
SAED	Selected area electron diffraction
SHE	Standard hydrogen electrode
SEM	Scanning electron microscopy
TIMS	Thermal ionized mass spectrometer
TEM	Transmission electron microscopy
TGA	Thermogravimetric analysis
VT-XRD	Variable temperature powder X-ray diffraction
WE	Working electrode

Chapter One: **Introduction**

1.1 Project overview

The majority of the world's energy demand is met by burning fossil fuels such as coal, natural gas and petroleum, all of which release greenhouse gases (e.g., water (H_2O), carbon dioxide (CO_2), methane (CH_4) and nitrogen oxides (NO_x)). These greenhouses gases are proven to have detrimental impacts on the environment, ultimately leading to global warming. In order to reduce our greenhouse gas emissions, steps away from non-renewable fossil fuels towards renewable energy sources (e.g. wind, solar, and geothermal) must be taken. However, due to the intermittency of renewable sources, technologies such as wind turbines, steam turbines or solar panels need to be coupled to an energy storage device such as a pumped hydro, flywheels, capacitors or rechargeable batteries.[1] Of the mentioned energy storage devices, rechargeable batteries are highly promising due to their longer discharges times (compared to capacitors and flywheels) and small physical size (compared to pumped hydro). Many battery chemistries have been successfully commercialized in the last few decades. Figure 1.1 summarizes select battery chemistries and their energy volumetric and gravimetric energy densities. Among them, lithium-ion batteries (LIBs) are the most advantageous due to their high voltage outputs (up to 4 V) and high energy density (up to 250 Wh kg^{-1}).[2] The *state-of-the-art* LIBs make use of carbonate-based organic Li-ion electrolytes that possess hazards from leakage, flammability, thermal instability and electrochemical instability.[3]

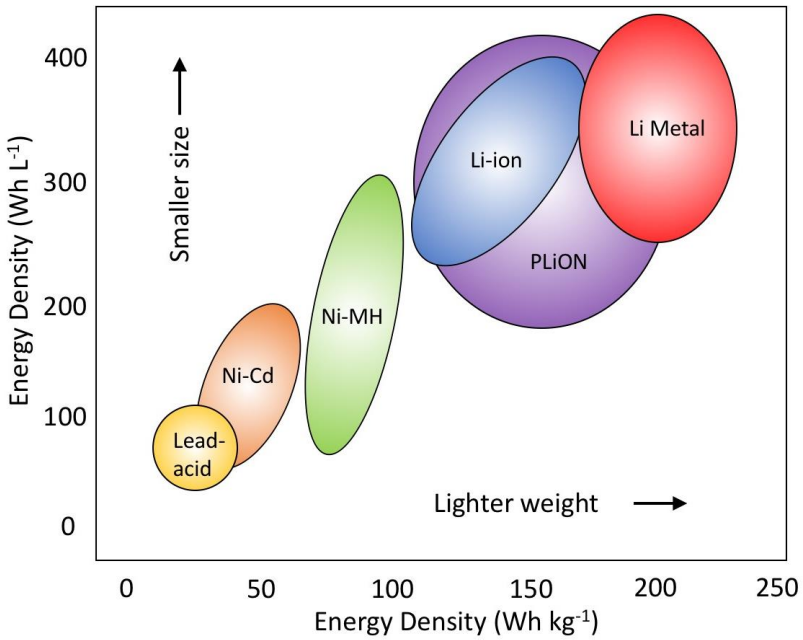

Figure 1.1 Comparison of select battery chemistries in terms of volumetric and gravimetric energy densities. [4]

Li-ion conducting solid-state ceramic electrolytes are strong alternatives to organic-based electrolytes in current LIBs. Solid-state electrolytes not only remove all hazards associated with leakage and flammability but also allow for advancements into next generation battery chemistry such as Li-O_2 and/or Li-S. The largest hurdle to overcome with solid-state electrolytes is achieving an ionic (Li^+) conductivity that rivals or surpasses the organic-based electrolytes (10^{-2} S cm^{-1}) at room or their operating temperatures. Of the reported Li-ion conducting ceramic electrolytes, garnet-type Li-ion electrolytes show the greatest promise for use in solid-state next generation batteries due to their high chemical stability with metallic Li. However, a stronger understanding regarding the environmental and electrochemical stability of lithium-garnets is required before they can be implemented into next generation batteries. The main focus of this thesis is to

understand the chemical and electrochemical stability of lithium-garnets for use in next generation Li batteries.

1.2 Research objectives

This research is aimed to determine the viability of using garnet-type Li-ion conductors in next generation Li-based batteries. One key aspect to next generation batteries is to replace the current lithiated graphite anode (372 mAh g^{-1}) with metallic Li (3861 mAh g^{-1}) and use O_2 as the cathode reactant for Li-O_2 battery cells, often referred to as Li-air. One suggested Li-O_2 architecture requires submerging a carbon support O_2 cathode and a protected metallic Li anode in aqueous media, as shown in Figure 1.2.

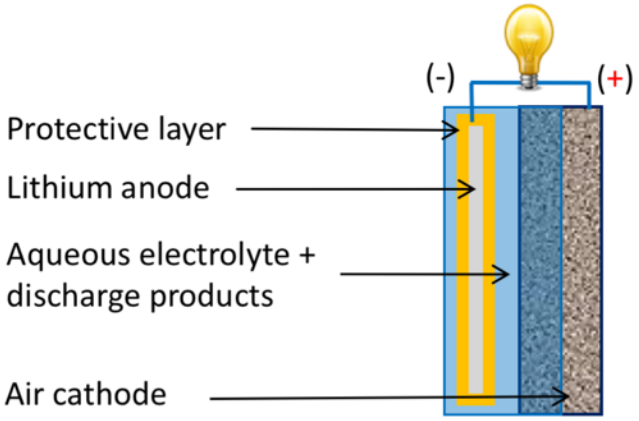

Figure 1.2 Suggested architecture of an aqueous Li-O_2 battery cell.

In this thesis, we have studied potential use of garnet-type $Li_{6.5}La_{2.5}Ba_{0.5}ZrTaO_{12}$ (LLBZT) oxide as a Li anode protective layer in an aqueous Li-O_2 cell configuration. The chemical and electrochemical stabilities of LLBZT were investigated using aqueous electrolytes namely: water, D_2O, brine (0.1 M LiCl, 0.1 M $NaNO_3$, 0.1 M K_2CO_3), LiOH and LiCl solutions. Further studies were carried out to investigate the stability of LLBZT in direct contact with metallic Li.

The chemical stability of another garnet-type $Li_7La_{2.75}Ca_{0.25}Zr_{1.75}Nb_{0.25}O_{12}$ (LLCZN) oxide was explored under the presence of 3% H_2O and CO_2-rich environments. Many researchers have reported that garnet-type electrolytes react with humidity and CO_2 leading to the formation of Li_2CO_3, but little work has been done to determine its effect on ionic conductivity or the required concentration limits before the spontaneous reaction occurs.[5] Here, we have investigated the effect of CO_2 and humidity on the ionic conductivity of garnet-type LLCZN using electrochemical impedance spectroscopy as a function of time.

1.3 Thesis organization

This thesis is divided into 7 chapters. **Chapter 1** outlines the project overview, motivation and organization of this thesis. **Chapter 2** provides background information on lithium ion batteries, next generation Li batteries and an overview of the stability of lithium-garnets towards aqueous media, CO_2 and metallic Li. A review article has been published in *Journal of Power Sources* (Hofstetter, K.; Samson, A.J.; Narayanan, S.; Thangadurai, V. J. Power Sources **2018**, 290, 297-312) focusing on the recent research of the chemical and electrochemical stability of lithium-garnets under aqueous (e.g., water, D_2O, and Li salt solutions), gaseous (e.g., CO_2, H_2O) and metallic (e.g., Li metal) media. **Chapter 3** describes the material synthesis as well as the experimental and characterization techniques used in this thesis.

Chapters 4-6 highlight the results in this thesis, each chapter gives a brief overview, main results, discussion and an overall summary of the respective chapter. **Chapter 4** reports the stability of $Li_{6.5}La_{2.5}Ba_{0.5}ZrTaO_{12}$ after the treatment of water, D_2O, 1 M LiOH, 1 M LiCl or brine (0.1 M LiCl, 0.1 M $NaNO_3$, 0.1 M K_2CO_3) solutions. Many of these results are published in *Solid State Ionics* (Hofstetter, K,; Samson, A.J,; Thangadurai, V. Solid State Ionics **2018**, 318, 71-81).

Chapter 5 focuses on the electrochemical stability of both $Li_{6.5}La_{2.5}Ba_{0.5}ZrTaO_{12}$ and $Li_7La_{2.75}Ca_{0.25}Zr_{1.75}Nb_{0.25}O_{12}$, parts of which have been published in *Solid State Ionics* (Hofstetter, K,; Samson, A.J,; Thangadurai, V. Solid State Ionics **2018**, 318, 71-81), *Journal of Electrochemical Society* (Samson. A.J,; Hofstetter. K,; Wachsman. E,; Thangadurai. V. J. Electrochem. Soc. **2018**, 165, A2303-A231), and to be submitted "Impedance analysis of garnet-type $Li_7La_{2.75}Ca_{0.25}Zr_{1.75}Nb_{0.25}O_{12}$ with and without ALD-Al_2O_3 under CO_2 and humidity" by Kyle Hofstetter, Alfred Junio Samson, Jiaqi Dai, Evan Gritton, Liangbing Hu, Eric Wachsman, and Venkataraman Thangadurai. **Chapter 6** focuses on the collaborative work done with the Eric Wachsman Group (University of Maryland) regarding the ionic (Li^+) conductivity stability of $Li_7La_{2.75}Ca_{0.25}Zr_{1.75}Nb_{0.25}O_{12}$ in the presence of 3 % H_2O and/or CO_2 using EIS which is to be submitted "Impedance analysis of garnet-type $Li_7La_{2.75}Ca_{0.25}Zr_{1.75}Nb_{0.25}O_{12}$ with and without ALD-Al_2O_3 under CO_2 and humidity" by Kyle Hofstetter, Alfred Junio Samson, Jiaqi Dai, Evan Gritton, Liangbing Hu, Eric Wachsman, and Venkataraman Thangadurai. **Chapter 7** summarizes all conclusions of this thesis and describes future outlook and experiments.

Chapter Two: **Background**

2.1 Introduction

The modern world has become heavily dependent on fossil fuels for its energy demands, which brings forth two major consequences: 1) depleting the limited resources of the non-renewable fuels, and 2) contaminating the atmosphere with harmful greenhouse gases leading to acidification of the oceans and global warming.[6] CO_2 is one of the major greenhouse gases produced from burning fossil fuels. In recent years, CO_2 levels have been on the rise, crossing 400 ppm, a 60 ppm increase since 1990.[7] This enforces the need to shift away from non-renewable resources (e.g., fossil fuels) to renewables, i.e. low or zero emission resources (e.g., wind and solar). However, they must be coupled with an energy storage device due to the intermittency of these energy resources. Some devices that are capable of storing energy include supercapacitors, pumped hydro, compressed air, flywheel, and batteries. Each of these devices have their own advantages and disadvantages, For example, capacitors and flywheels are capable of releasing the stored energy quickly but as a consequence fully discharge in seconds.[8] Pumped hydro and compressed air systems are capable of grid storage capacity but as a result are physically large and stationary.[8] Batteries discharge in the range of minutes-hours, can be designed for both portable and stationary applications but have inherent safety risks associated. Table 2.1 highlights some of the various batteries currently available along with their energy densities.

Table 2.1 Comparison of popular primary and secondary battery chemistries. [1, 2]

	Type	Reaction	Potential (V)	Gravimetric energy (Wh kg^{-1})	Volumetric energy (Wh L^{-1})
Primary	Alkaline	$Zn + 2MnO_2 \rightarrow ZnO + Mn_2O_3$	1.5	145	400
	$Li/SOCl_2$	$4Li + 2SOCl_2 \rightarrow 4LiCl + S + SO_2$	3.65	590	1100
	Zinc/air	$Zn + (1/2O_2) \rightarrow ZnO$	1.65	350	1300
Secondary	Lead-acid	$Pb + PbO_2 + 2H_2SO_4 \leftrightarrows 2PbSO_4 + 2H_2O$	2.1	35	70
	Nickel-cadmium	$Cd + 2NiOOH + 2H_2O \leftrightarrows 2Ni(OH)_2 + Cd(OH)_2$	1.35	35	100
	Lithium-ion	$Li_xC_6 + Li_{(1-x)}CoO_2 \leftrightarrows LiCoO_2 + C_6$	~4	150	400

The current *state-of-the-art* battery chemistry is lithium-ion. Lithium-ion batteries possess high gravimetric and volumetric energy densities, 250 Wh kg^{-1} and 650 Wh L^{-1}, respectively.[2] Modern lithium ion batteries use organic electrolytes composed of Li salts dissolved in an ethylene carbonate/dimethyl carbonate (EC/DMC) mixture which is prone to leakage and flammability. As a result, a major focus has been geared towards the development of solid-state (ceramic, glass, etc.) electrolytes capable of removing the need of the organic-based electrolyte and ultimately removing the risk of leaking and/or flammability.

2.2 Lithium-ion battery (LIB)

Batteries are electrochemical devices capable of storing electrical energy in the form of chemical energy. By definition, batteries refer to a collection of single cells that are able to convert from chemical to electrical energy, and electrical to chemical energy in the case of rechargeable cells. These single cells consist of three components, anode (negative electrode), electrolyte (ion

conductive material), and a cathode (positive electrode). Batteries are classified into one of two classifications, primary or secondary. Primary batteries refer to non-rechargeable/single-use cells such as an alkaline battery. In contrast, secondary batteries can be recharged and used for many cycles (charging and discharging) such as the LIB. In addition to primary and secondary battery classifications, batteries are rated based on their capacity and energy. The capacity refers to how much charge the cell can hold, expressed in amp-hour (Ah) but is commonly expressed based on the per gram scale as milliamp-hour per gram (mAh g^{-1}). The capacity can be calculated using the following:

$$Capacity = \frac{nF}{3.6 * M_W} \tag{2.1}$$

where n is the number of electrons involved in the reaction per metal centre, F is Faraday's constant (96,487 C mol^{-1}), M_w is the molar mass of the active material and 3.6 is the conversion of coulombs to milliamp-hour.

For example, $Li \rightarrow Li^{+} + e^{-}$:

$$Capacity_{Li} = \frac{(1e^{-})(96487 C\, mol^{-1})}{3.6 * (6.941 g\, mol^{-1})} = 3861 mAh\, g^{-1}$$

the energy (Wh) is typically expressed based on gravimetric (Wh kg^{-1}) or volumetric (Wh L^{-1}) which is determined by multiplying the capacity of the cell by the potential:

$$Energy\,(Wh) = Capacity\,(Ah) * Potential\,(V) \tag{2.2}$$

The gravimetric and volumetric energy densities are then calculated by using the gravimetric or volumetric capacities:

$$Energy\,(Wh\, kg^{-1}) = Capacity\,(Ah\, kg^{-1}) * Potential\,(V) \tag{2.3}$$

$$Energy\,(Wh\,L^{-1}) = Capacity\,(Ah\,L^{-1}) * Potential\,(V) \quad (2.4)$$

Of all the modern day commercially available rechargeable batteries, the LIB is the leader in terms of energy density - meaning that it is capable of holding the most energy in the smallest space and mass. The LIB was first proposed by John B. Goodenough in 1980 making use of a $LiCoO_2$ cathode and Li anode.[9] LIBs were later commercialized by Sony in 1991 with a $LiCoO_2$ cathode and lithiated graphite (Li_xC_6) anode.[10] Although lithiated graphite is the universal anode material of commercially available LIBs, various cathode materials with varying voltage windows and capacities have been developed, Table 2.2 compares some of the current cathode materials used in commercial LIBs. LIBs have found widespread applications from pacemakers and cell phones to electric vehicles, and more recently grid storage.

Table 2.2 Comparison of current commercially available Li-ion cathode materials.[11]

Cathode material	Discharge potential vs. Li/Li^+	Specific capacity (mAh/g)	Application*
$LiCoO_2$ (LCO)	3.9	155	Portable electronics
$LiFePO_4$ (LFP)	3.4	160	Power tools
$LiMn_2O_4$ (LMO)	4.0	100-120	Power tools
$LiNiCoAlO_2$ (NCA)	3.7	180	Premium electronics
$LiNiMnCoO_2$ (NMC)	3.8	160	Power tools, electric vehicles

*Cathode materials are not limited to these specific applications, rather this is typically where they are found.

2.2.1 Operation of lithium-ion batteries

A schematic representation of a LIB with a $LiFePO_4$ cathode is shown in Figure 2.1. The electrolyte is sandwiched between the negative anode and positive cathode electrodes. The anode is typically attached to a copper current collector where the cathode is typically on an aluminium current collector. Both the anode and cathode are layered host materials capable of intercalation

(insertion) and de-intercalation (release) of Li-ions. The anode and cathode are connected via an external circuit to transport electron flow. On discharge, the anode will undergo an oxidation reaction (reaction 2.1), releasing a Li-ion and an electron. Subsequently, the Li-ion will travel through the electrolyte to the cathode while the electron will move through the external circuit, where they will reductively react (reaction 2.2) with the cathode materials. Simultaneously, the electron travelling through the external circuit is used at the electrical source to power various devices. During charging, the cathode will undergo oxidation, releasing the Li-ion and electron and similarly, the Li-ion will travel through the electrolyte to the anode and the electron through the external circuit.

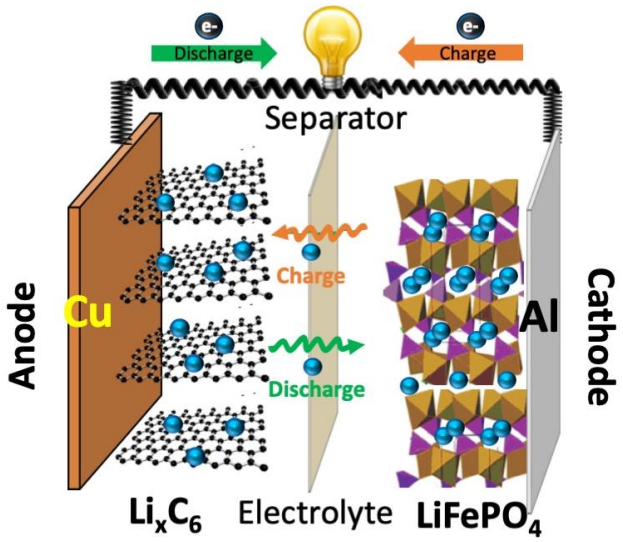

Figure 2.1 Operation of a rechargeable lithium-ion battery with a lithiated graphite anode (Li_xC_6), lithium iron phosphate ($LiFePO_4$) cathode and organic electrolyte.

On discharge the following reactions occur at the anode and cathode, respectively:

Anode (-): $LiC_6 \underset{Charge}{\overset{Discharge}{\rightleftharpoons}} C_6 + Li^+ + e^-$ (2.1)

Cathode (+): $Fe^{III}PO_4 + Li^+ + e^- \underset{Charge}{\overset{Discharge}{\rightleftharpoons}} LiFe^{II}PO_4$ (2.2)

Net: $Fe^{III}PO_4 + LiC_6 \underset{Charge}{\overset{Discharge}{\rightleftharpoons}} LiFe^{II}PO_4 + C_6$ (2.3)

2.2.2 Challenges of LIBs

Although LIBs have found widespread applications, they are still limited by their gravimetric and volumetric energy densities as well as safety. The electrolyte typically consists of a Li salt, typically $LiPF_6$ dissolved in an organic ethylene carbonate/dimethyl carbonate (EC:DMC) mixture. These electrolytes are highly flammable, have a tendency to leak and are thermally unstable.[6, 12] During battery operation using an organic electrolyte, Li dendrites can form creating an internal electrical short-circuit between the anode and cathode and in some cases thermal runaway ultimately causing the organic electrolyte to catch fire.

Among the current commercially available batteries, LIBs have the greatest energy density in terms of mass and volume.[13] However, they still lie below the energy densities required to make electric vehicles economically viable, while also removing 'range anxiety'. The United States Department of Energy (DOE) has set battery metric targets of 250 Wh kg^{-1} and 650 Wh L^{-1} by 2022.[14] In order to achieve these metrics, alternative battery chemistry must be considered.

2.3 Next generation battery technology

Next generation batteries are considered to be batteries with higher energy densities than current LIBs while also having increased safety. One of the key aspects to next generation batteries is to make use of Li anode (3861 mAh g^{-1}), opposed to the lithiated graphite (372 mAh g^{-1}). This will also require cathode materials with higher capacities, those suggested in the literature include elemental sulfur and oxygen.[15] Figure 2.2 compares the theoretical energy densities of commercialized batteries to purposed next generation batteries.

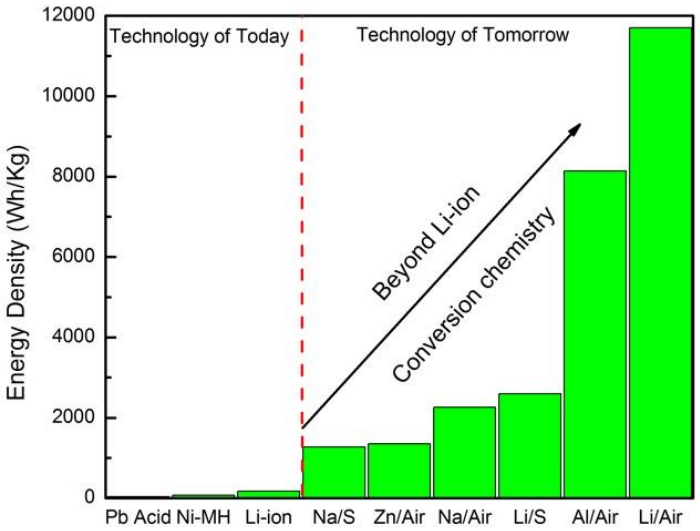

Figure 2.2 Comparison of energy densities of current commercially available batteries to proposed next generation batteries.[1, 15]

Li-O_2, commonly referred to as Li-air batteries fall into one of the four proposed architectures, all of which have a Li anode and porous carbon air cathode but are differentiated by their electrolyte: (1) aprotic – organic electrolyte; (2) aqueous – use water with dissolved Li salt but require the Li anode to have a protective layer; (3) all-solid-state – a Li-ion conductive solid electrolyte; and (4) mixed aprotic/aqueous – anode is submerged in an organic electrolyte which is separated from the air cathode by an aqueous electrolyte. [5, 15] Of the four proposed designs aqueous Li-O_2 batteries show the greatest promise due to the lack of flammable organic electrolyte compared to the aprotic and mixed design. The aqueous battery also reduces the number of solid-solid interfaces compared to all-solid-state batteries, allowing for a more simplistic design. In aqueous Li-O_2 batteries, the Li anode is separated from the aqueous electrolyte by a Li-ion conducting solid electrolyte.[16] This requires the solid electrolyte to be chemically and electrochemically stable towards Li and the aqueous electrolyte.

2.4 Solid state lithium-ion conducting electrolytes

There are only a handful of reported solid-state Li-ion conducting electrolytes, Figure 2.3 compares the advantages and disadvantages of the various classifications of solid-state electrolytes.[17] The key properties sought after in a solid electrolyte include:[18]

1) High total (bulk + grain boundary) Li-ion conductivity near 10^{-2} S cm^{-1} with a Li-ion transference number (t_{Li+}) close to 1,
2) chemically stable with high voltage Li anodes and cathodes and a wide electrochemical stability window: ≥ 6 V vs. Li/Li^+,
3) chemically stable against redox reactions occurring at the anode and cathode interfaces,
4) low or negated electrode | electrolyte interfacial resistance, and
5) inexpensive relative to other battery components and environmentally friendly.

This thesis and the following sections will focus on oxide-based solid-state ceramic electrolytes.

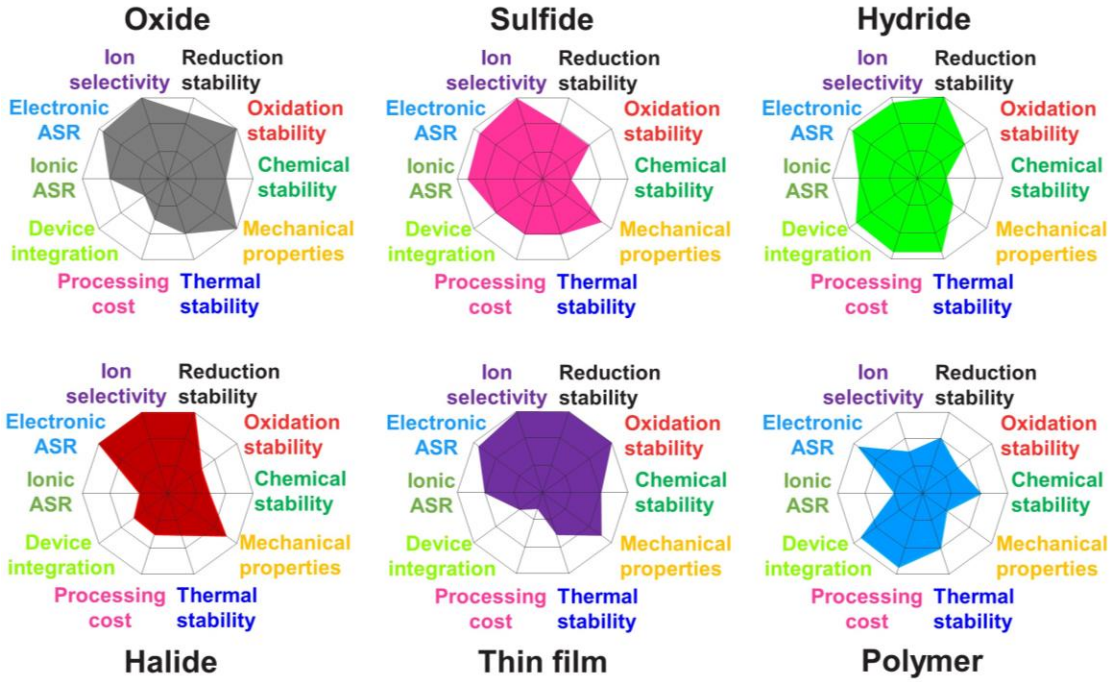

Figure 2.3 Spider plots of the performance and stability of various solid electrolyte materials.[17]

2.4.1 NASICON and LISICON

2.4.1.1 NASICON

Na SuperIonic CONductor (NASICON) was first coined in 1976 with the discovery of $Na_{1-x}Zr_2Si_xP_{3-x}O_{12}$ ($0 \leq x \leq 3$) [ref. [19]]. The parent phase has the general formula $AM_2(PO_4)_3$ where A = Li or Na and M = Ge, Zr or Ti.[20] For Li-ion conducting NASICON, $LiTi_2(PO_4)_3$ system has been the most widely investigated. These systems contain TiO_6 octahedra and PO_4 tetrahedra that are connected through a three dimensional (3D) edge sharing.[21] The typical NASICON crystal structure is shown in Figure 2.4. NASICON structures show high conductivities of 10^{-3} S cm^{-1} at room temperature but lack stability with Li due to the reduction of Ti^{4+} to Ti^{3+} or Ge^{4+} to Ge^{3+}- ultimately leading to electronic conduction. The stability with Li can be solved by substituting Ti

or Ge with Zr, however, this results in a lower ionic conductivity of ~ 10^{-4} S cm^{-1} at 25 °C and is costly to produce.[22]

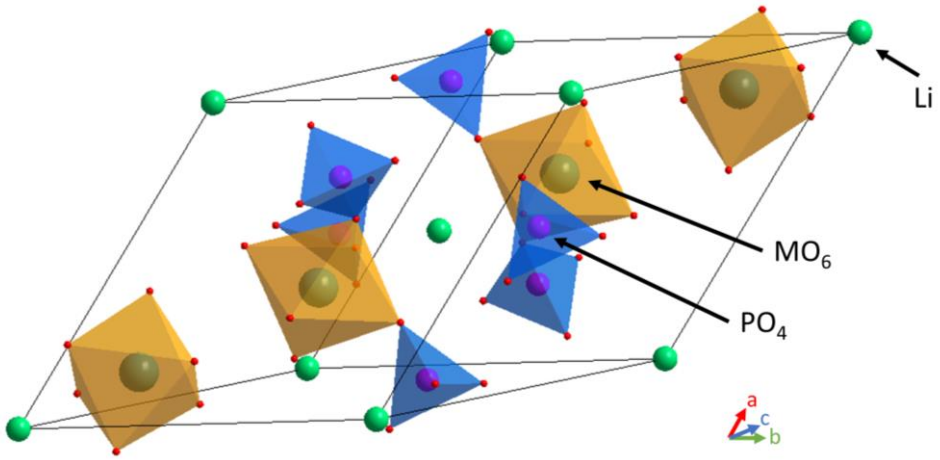

Figure 2.4 Typical crystal structure of NASICON-type with the formula $LiM_2(PO_4)_3$. Space group: *P1, a = b = c = 9.0581 Å*. [23]

2.4.1.2 LISICON

Li SuperIonic CONductors (LISICON) are a family of systems with the chemical formula $Li_{2+2x}Zn_{1-x}GeO_4$ ($0.36 \leq x \leq 0.87$) [ref. [24]]. LISICONs have relatively low ionic conductivities (10^{-7} S cm^{-1}) at room temperature, compared to other reported Li-ion conductive systems.[24] The low ionic conductivity can be improved by substituting oxygen within the structure for sulfur - leading to another classification of Li-ion solid electrolytes, thio-LISICON. However thio-LISICONS suffer from reactivity with moisture leading to the formation of toxic hydrogen sulfide (H_2S). Similar to NASICON, LISICON suffers from instability with Li due to the reduction of Ge^{4+} to Ge^{3+}. Furthermore, LISICON is highly reactive towards to CO_2. Therefore, ageing of LISICON in ambient or CO_2 rich atmosphere leads to degradation of the ionic conductivity and overall performance. Figure 2.5 shows an idealized crystal structure of LISICON.[24]

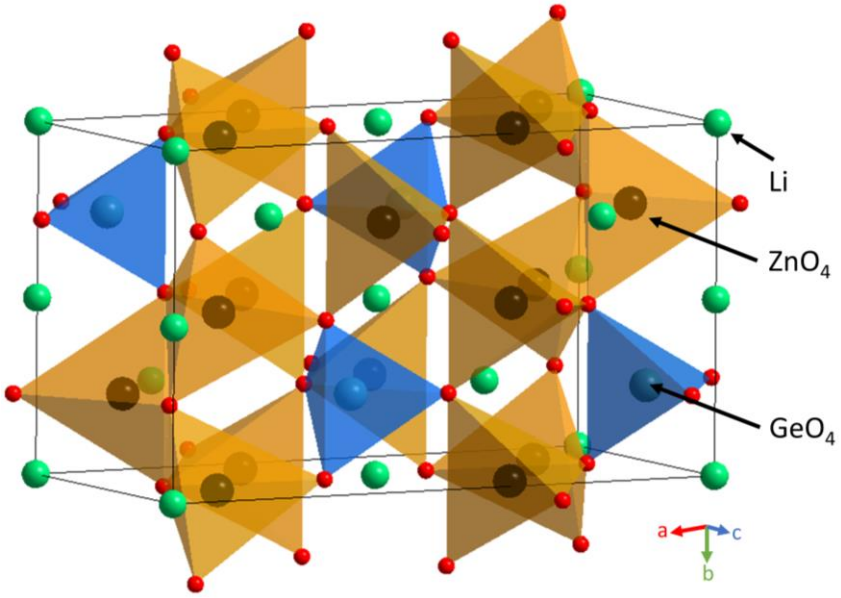

Figure 2.5. Idealized crystal structure of LISICON, $Li_{14}Zn(GeO_4)_4$. Space group: *Pnma*, *a* = 10.828 Å, *b* = 6.251 Å, *c* = 5.14 Å.[25]

2.4.2 A-site deficient perovskite-type

The perovskite has the general chemical formula of ABO_3, where A and B are twelve-fold and six-fold coordinated cations, respectively. The Li-ion conductive perovskite has A = Li, La, or a vacancy and B = Ti with a nominal formula $Li_{3x}La_{(2/3)-x}\square_{(1/3)-2x}TiO_3$ (LLT, $0 < x < 0.16$ and □ is a vacancy).[26] Figure 2.6 shows the idealized cubic perovskite crystal structure. Many crystal structures have been reported for lithium perovskites including cubic, hexagonal, tetragonal, and orthorhombic.[26] It is believed that varying synthesis routes and Li/vacancy concentrations lead to different crystal structures. Solid-state synthesis is the most common method for the preparation of perovskites, however, during high-temperature sintering processes - volatilization of Li_2O makes it difficult to control Li concentrations in the structure.[26] Li-ion mobility is through A-site deficiencies that are randomly distributed throughout the structure. Li-ion conductive perovskites are among the highest Li-ion conducting solids reaching $\geq 10^{-3}$ S cm^{-1} at room temperature in some

systems.[27] Just like NASICON and LISICON structures, these materials suffer from reductive instability of the Ti center, making them incompatible with Li.

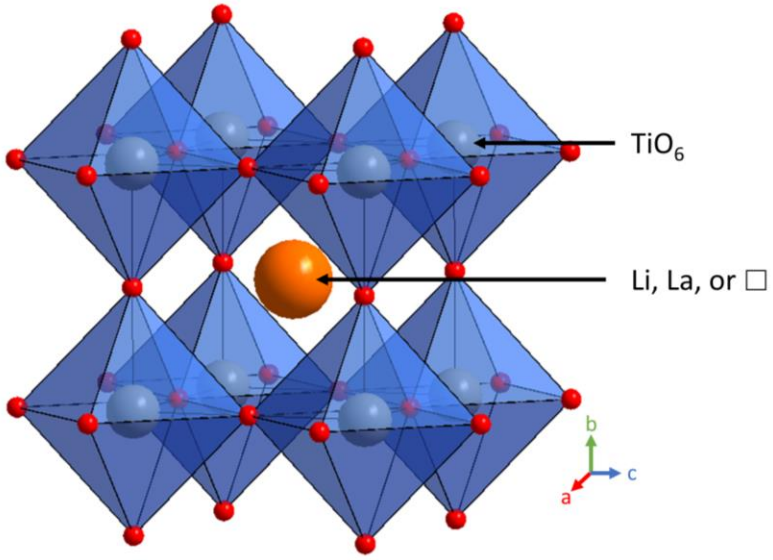

Figure 2.6 Idealized structure of Li-ion conductive perovskite, (Li,La,□)TiO_3. Space group: $Pm\bar{3}m$, a = 3.8 Å.[26]

2.4.3 Lithium-stuffed Garnet-type

The ideal garnets are orthosilicates with the nominal formula of $A_3B_2(SiO_4)_3$, where A is an eight-fold coordinated divalent cation, B is a six-fold coordinated trivalent cation, and Si is in a four-fold coordinated site. These systems are often stabilized in the body-centered cubic structure with the $Ia\bar{3}d$ space group. The first Li based garnet was reported by Mazza in 1988 with the chemical formula $Li_5La_3M_2O_{12}$ (M = Nb or Ta).[28] It wasn't until later in 2003 that Thangadurai *et al.* reported Li-ion mobility within these systems with Li-ion conductivity of 10^{-6} S cm^{-1} at room temperature.[29] Figure 2.7 shows the idealized crystal structure of cubic phase lithium-garnet-type $Li_5La_3M_2O_{12}$. The structure contains eight-fold coordinated dodecahedral LaO_8 and six-fold coordinated MO_6 octahedra leading to a $[La_3M_2O_{12}]^{5-}$ framework that must accommodate five Li-ions.[30] Li-ions are then distributed throughout three different interstitial sites: tetrahedral (24d),

octahedral (48g) and distorted four-fold (96h) octahedral coordination.[31] These materials are referred to as lithium-rich or lithium-stuffed because they can accommodate more Li than the classical garnet $Li_3Ln_3Te_2O_{12}$ (Ln = Y, Pr, Nd, Sm-Lu).[32] The presence of interstitial space and variety of coordination sites allows flexibility of substitution within the structure. Since their discovery as a Li-ion conductive material, there has been a lot of focus towards increasing the ionic mobility through doping and substitution, Figure 2.8 highlights some of the doping stratagies.[33] In 2007, Thangadurai *et al.* had substituted Ta and Nb with Zr, allowing for additional Li to be added to the structure, $Li_7La_3Zr_2O_{12}$, this resulted in a large increase in ionic conductivity to ~10^{-4} S cm^{-1} at room temperature.[34] These materials have shown to have large a electrochemical stability window (ESW) up to 9 V vs. Li/Li^+ [ref. [35, 36]], making them strong candidates for next generation batteries with Li anodes. The focus of this thesis will be understanding the chemical and electrochemical stability of lithium-stuffed garnet materials with aqueous and humid environments, CO_2 rich environments and with Li for potential use in aqueous Li-O_2 batteries.

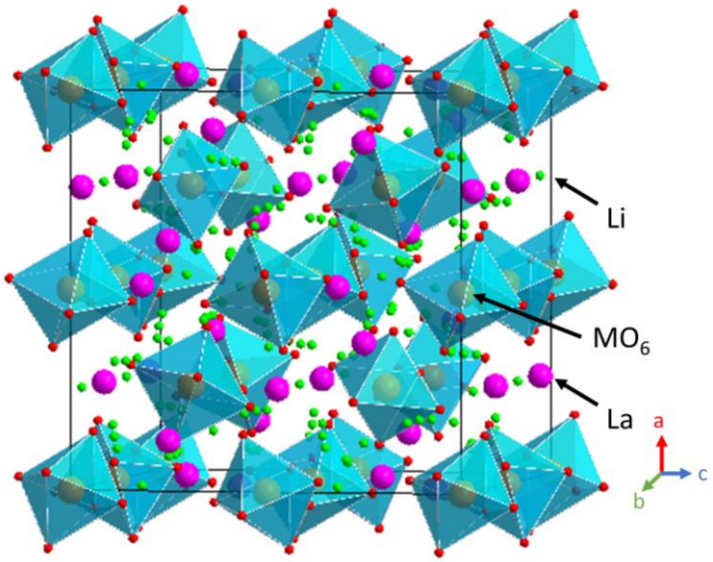

Figure 2.7 Idealized cubic lithium-stuffed garnet crystal structure, $Li_5La_3M_2O_{12}$. Space group $Ia\bar{3}d$, a = 12.7943 Å.[31]

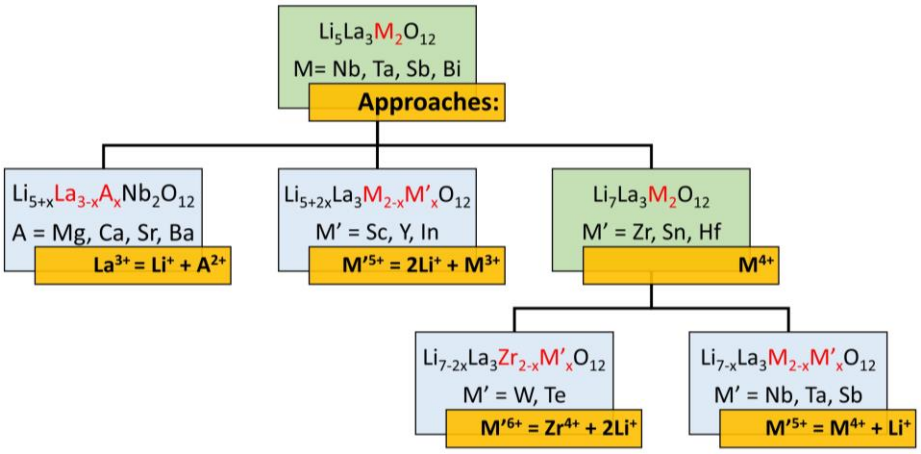

Figure 2.8 Doping strategies of lithium-garnet materials to increase ionic mobility, structural stability and electrochemical stability. Green boxes indicate the parent Li_5 and Li_7 phases and blue are doped variants.

2.5 Stability of lithium-stuffed garnets in aqueous/moisture environments

Lithium-garnets are known to undergo a spontaneous Li^+/H^+ exchange in the presence of water and moisture.[5] Preliminary studies were performed by Nyman et al. where sintered powders of $Li_5La_3M_2O_{12}$ (M = Nb or Ta) were stirred in deionized water, a rapid increase in pH from 7 to 11 was observed for both samples.[37] This increase in pH has been attributed to a Li^+/H^+ exchange by the following reaction:[37-41]

$$Li_5La_3M_2O_{12} + xH_2O \rightarrow Li_{5-x}H_xLa_3M_2O_{12} + xLiOH \qquad (2.4)$$

There are many factors that affect the extent and rate of ion exchange including particle size, solution composition, temperature, immersion duration and chemical composition. Table 2.3 summarizes the proton-exchange properties of various lithium-stuffed garnets.

Table 2.3 Summary of proton-exchanged and chemical stability of lithium-stuffed garnet. Reprinted (adapted) with permission from Hofstetter, K.; Samson, A.J.; Narayanan, S.; Thangadurai, V. *J. Power Sources* 2018, *390*, 297-312. Copyright 2018 Elsevier.

Composition [Ref.]	Aqueous treatment / time	H^+/Li^+ exchange %	Characterization techniques [a]
$Li_5La_3Ta_2O_{12}$ [37]	Powders stirred in neutral water/30 min.	~20	Monitor pH, IR spectroscopy, ^6Li MAS NMR, TGA, XRD.
$Li_5La_3Ta_2O_{12}$ [37]	Powders stirred in acidified conditions/1 h.	~80	Monitor pH change, IR spectroscopy, ^6Li MAS, NMR TGA, XRD.
$Li_5La_3Nb_2O_{12}$ [42]	Reflux powder in benzoic acid + ethanol/1 week.	82 ± 1	Flame photometry, TGA, XRD, ^6Li MAS NMR, ND
$Li_5La_3Nb_2O_{12}$ [40]	3 mm pellet placed in excess water at RT/4 days.	48	TGA, ND, XRD
$Li_5La_3Nb_2O_{12}$ [40]	3 mm pellet placed in excess D_2O/4 days	40	TGA, XRD, EIS
$Li_5La_3Nb_2O_{12}$ [40]	Powders soaked in D_2O/4 days.	88	TGA, FTIR
$Li_5La_3Nb_2O_{12}$ [40]	3 mm pellet was hung in excess water at RT/7 days.	59	TGA, ND, XRD
$Li_5La_3Nb_2O_{12}$ [40]	3 mm pellet was hung in excess water at RT/10 days.	83	TGA, ND, XRD
$Li_5La_3Nb_2O_{12}$ [40]	3 mm pellet was hung in excess water at RT/14 days.	93	TGA, ND, XRD
$Li_5La_3Nb_2O_{12}$ [43]	Powder left in ambient air/several years.	~56	XRD, EIS, Raman, TGA, ICP, ND, ^7Li, ^6Li, ^1H MAS-NMR
$Li_5La_3Nb_2O_{12}$ [44]	Powders stirred in acetic acid at RT/4 days	100	XRD, TGA, FTIR, SEM
$Li_{5.5}Ba_{0.5}La_{2.5}Nb_2O_{12}$ [44]	Powders stirred in acetic acid at RT/4 days	40	XRD, TGA, FTIR, SEM
$Li_6BaLa_2Nb_2O_{12}$ [44]	Powders stirred in acetic acid at RT/4 days	13	XRD, TGA, FTIR, SEM
$Li_6La_2CaNb_2O_{12}$ [45]	Reflux in pure acetic acid/ 4 days	81.7	TGA, TEM, XRD, ND
$Li_{6.5}La_{2.5}Ba_{0.5}ZrTaO_{12}$ [46]	Pellet submerged in H_2O at RT/5 days	52	TGA, XRD, EIS, SEM
$Li_{6.5}La_{2.5}Ba_{0.5}ZrTaO_{12}$ [46]	Pellet submerged in D_2O at RT/5 days	31	TGA, XRD, EIS, SEM
$Li_{6.5}La_{2.5}Ba_{0.5}ZrTaO_{12}$ [46]	Pellet submerged in 1 M LiOH at RT/5 days	45	TGA, XRD, EIS, SEM
$Li_{6.5}La_{2.5}Ba_{0.5}ZrTaO_{12}$ [46]	Pellet submerged in 1 M LiCl at RT/5 days	79	TGA, XRD, EIS, SEM
$Li_7La_3Zr_2O_{12}$ [47]	Exchange occurring during sample preparation	2	TGA, MS, DSC, XRD
$Li_7La_3Zr_2O_{12}$ [41]	Annealing pellet at 150 °C in ambient air/24 h	69	TGA, ICP, XRD, Raman, ND
$Li_7La_3Zr_2O_{12}$ [41]	Annealing pellet at 350 °C in ambient air/4 days	21.4	TGA, XRD, Raman, ND

$Li_7La_3Sn_2O_{12}$ [48]	Reflux power in benzoic acid+ethanol/1 week	68 ± 1	Flame photometry, TGA, XRD
$Li_7La_3Sn_2O_{12}$ [42]	Reflux power in benzoic acid+ethanol/1 week	70 ± 1	Flame photometry, TGA, XRD, ^{7}Li MAS NMR, ND

[a] (EIS – electrochemical impedance spectroscopy, FTIR, ICP-OES – inductively coupled plasma optical emission spectrometry, MAS-NMR – Magic angle spinning nuclear magnetic resonance spectroscopy, ND – Neutron diffraction, RT – room temperature (22–25 °C), SEM – Scanning electron microscopy, TGA – Thermogravimetric analysis, and XRD - X-ray diffraction).

Many of the above compositions have confirmed the ion exchange to be a topotactic.[38-40, 44, 46, 49, 50] O'Callaghan and Cussen determined that garnets with lower Li content have majority of the Li within the tetrahedral ('framework') sites and less in the octahedral ('mobile') sites using neutron diffraction.[30, 51] As the Li concentration increases, the occupation in the tetrahedral sites decreases and octahedral increases. Truong and Thangadurai had reported that the tetrahedral sites are more favourable to undergo Li^+/H^+ exchange over the octahedral sites. As a result, compositions with lower Li concentrations undergo Li^+/H^+ exchange to a larger degree.[38] Figure 2.9 shows the proton exchanged crystal structure, $Li_{5-x}H_xLa_3M_2O_{12}$ (M = Nb or Ta).[5, 40]

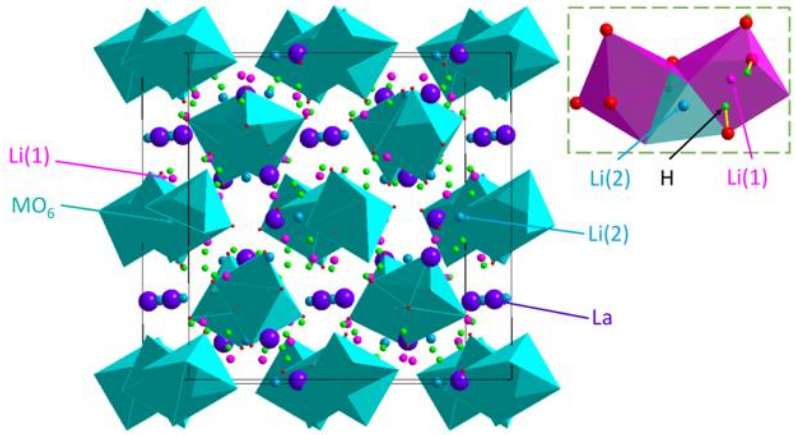

Figure 2.9 Crystal structure of $Li_{5-x}H_xLa_3M_2O_{12}$ (M = Nb or Ta), full unit cell representation. M = teal polyhedra, La = purple sphere, Li1 site = pink sphere, Li2 = blue sphere, and H = green sphere. Zoom illustrates a portion of the structure $Li_{5-x}H_xLa_3M_2O_{12}$ showing both distorted octahedral Li1 site (pink) and tetrahedral Li2 site (blue). Reprinted with permission from Hofstetter, K.; Samson, A.J.; Narayanan, S.; Thangadurai, V. J. Power Sources 2018, 390, 297-312. Copyright 2018 Elsevier.

Although treatment with aqueous solution and organic acid have been shown to undergo the spontaneous Li^+/H^+ ion-exchange, this reaction has also been reported to occur during synthesis due to the presence of moisture.[46, 47] With this, a deep understanding of the chemical and electrochemical stability of lithium-garnets is required before they can be implemented into an aqueous Li-O_2 cell.

2.6 Stability of lithium-stuffed garnets in CO_2 rich environments.

Lithium-garnets are also reported to react with CO_2 forming Li_2CO_3 layers. Two reaction mechanisms have been reported:

A) Direct carbonation:[5, 52]

$$Li_7La_3Zr_2O_{12} + xCO_2 \rightarrow Li_{7-2x}La_3Zr_2O_{12-x} + xLi_2CO_3 \quad (2.5)$$

B) Two-step reaction beginning with protonation forming a LiOH layer, which further reacts with CO_2: [5, 46, 52]

$$Li_7La_3Zr_2O_{12} + xH_2O \rightarrow Li_{7-x}H_xLa_3Zr_2O_{12} + xLiOH \quad (2.6)$$

$$2LiOH + CO_2 \rightarrow Li_2CO_3 + H_2O \quad (2.7)$$

Figure 2.10 shows the two-step reaction forming the Li_2CO_3 layer. Li_2CO_3 has been detected forming on the garnet surface using X-ray diffraction, X-ray photoelectron spectroscopy (XPS), and Fourier-transform infrared spectroscopy.[52, 53] Thermogravimetric analysis has also revealed that CO_2 can be desorbed from the surface around 700 ^oC.[53] The largest issue reported with Li_2CO_3 formation on the garnet surface is the increased interfacial resistance between the lithium-garnet and Li compared to an uncontaminated surface, further explained in section 2.7. Little work has been done to investigate the effect of CO_2 on ionic conductivity in lithium-garnet materials. This

thesis aims to explore the lithium-garnets for its allowance to maximum tolerance towards CO_2 before Li-ion conductivity is deteriorated.

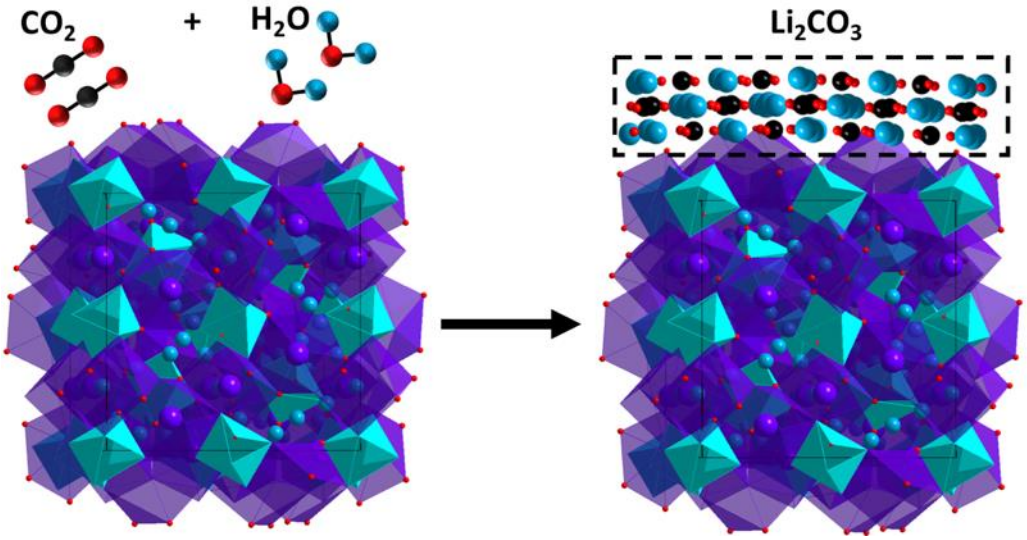

Figure 2.10 Schematic diagram showing the reaction of $Li_7La_3Zr_2O_{12}$ garnet exposed to humid air (left) followed by lithium carbonate formation (right). Reprinted with permission from Hofstetter, K.; Samson, A.J.; Narayanan, S.; Thangadurai, V. *J. Power Sources* 2018, *390,* 297-312. Copyright 2018 Elsevier.

2.7 Stability of lithium-stuffed garnets with lithium.

One of the major aspects for a solid-state electrolyte to be viable in a next-generation Li battery is to be highly stable with direct contact with Li at open circuit potential and under its operating conditions. Of the ceramic electrolytes mentioned in section 2.4, lithium-garnets are among a few Li-ion conducting materials stable with Li. Li is a powerful reducing agent with a reduction potential of -3.04 vs. standard hydrogen electrode (SHE), the lowest of all metals.

2.7.1. Chemical and electrochemical stability of lithium-garnets with lithium

Although many lithium-garnet compositions have been reported to be stable with Li,[29, 34, 35, 54] there are reports of lithium-garnets to be unstable with Li, namely those with highly doped or

substituted with Nb;[55, 56] which is attributed to the reduction of Nb^{5+} to Nb^{4+} [ref. [55]]. Many groups have reported the retention of the garnet crystal structure after the treatment of molten Li for durations ranging from 12 h – 2 months [29, 35, 54, 57] and at room temperature from 24 h to 6 months.[35] Cyclic voltammetry (CV) has revealed many lithium-garnet materials to be electrochemically stable up to 6-9 V vs. Li/Li^+ [ref. [35, 36, 58]].

Lithium-garnet materials are also reported to have a high shear modulus around 60 GPa, where Li has a shear modulus of 4-5 GPa.[59] To prevent dendrite formation, Monroe and Newman suggested that the shear modulus of a solid electrolyte be double that of Li to prevent dendrite nucleation,[60] a property well surpassed by lithium-garnets. However, due to this high shear modulus of lithium-garnets, the garnet surface does not wet well with Li.[61, 62]

2.7.2 Lithium | Garnet interface

Due to the poor wetting of Li onto the garnet surface, a high interfacial resistance is present. The Li dissolution process in the Li | garnet interface ($Li \rightarrow Li^+ + e^-$) is a combination of the Li-ion transfer across the interface as well as the simultaneous formation of a vacancy in the metal surface and the incorporation of a Li-ion into the garnet structure. The untreated garnet sample has been reported to have an area specific resistance (ASR) at the Li | garnet interface as high as 2000 Ω cm^2 [ref. [5, 63]]. In order to reduce the interfacial resistance, many attempts for surface modification have been carried out, Table 2.4 summarizes the various lithium-garnet compositions and their Li | garnet interfacial resistance before and after surface modification.

Table 2.4 Li metal cycling/electrochemical stability studies with Li-garnet electrolytes. Reprinted (adapted) with permission from Hofstetter, K.; Samson, A.J.; Narayanan, S.; Thangadurai, V. *J. Power Sources* 2018, *390*, 297-312. Copyright 2018 Elsevier.

Composition (synthesis)	σ_{Total} at RT (S cm^{-1})	Ri, – "unmodified" interface (Ω cm^2); Electrochemical stability	[a] Ri, - "modified" interface (Ω cm^2); Electrochemical stability
$Li_{5.98}Al_{0.33}La_3Zr_{1.95}O_{11.89}$ Large grains (LG): 100–200 μm; Small grains (SG): 20–40 μm (1100 °C/12 h) [64]	LG: 2.0 x 10^{-4} SG: 2.5 x 10^{-4}	LG: 130; Galvanostatic cycling up to 90 μA cm^{-2}, 30 min/Li plate or strip: Cell shorted during the 2 h period at the current density of 90 μA cm^{-2}.	SG: 37; Galvanostatic cycling up to 134 μA cm^{-2}, 30 min/Li plate or strip): voltage constant at different current densities, increasing linearly at higher current densities up to 134 μA cm^{-2}. Above this value, the cell exhibited voltage instability and short- circuited.
$Li_{6.75}La_{2.75}Ca_{0.25}Zr_{1.75}Nb_{0.25}O_{12}$ (1050 °C/12 h) [65]	2.2 x 10^{-4}	1900; Galvanostatic cycling at 0.1 mA cm cm^{-2}, 10 min/Li plate or strip: observation not reported.	20; Modification: ZnO coating via ALD; Galvanostatic cycling at 0.1 mA cm−2, 10 min/Li plate or strip: interfacial resistance decreased to 20 Ω cm^2 after 50 h of stripping – plating.
$Li_{6.85}La_{2.9}Ca_{0.1}Zr_{1.75}Nb_{0.25}O_{12}$ (1050 °C/12 h) [66]	2.5 x 10^{-4}	925; Galvanostatic cycling at 0.05 mA cm^{-2}, 10 min/Li plate or strip: voltage hysteresis is large and the plating/stripping curves are unstable.	127; Modification: Si coating via PECVD; Galvanostatic cycling up to 0.2 mA cm^{-2}, 10 min/Li plate or strip: voltage profiles exhibited flat and stable plating and stripping curves with small overpotential. Voltage profile remained stable after cycling for 225 h (0.1 or 0.05 mA cm^{-2}, 10 min/Li plate or strip).
$Li_{6.85}La_{2.9}Ca_{0.1}Zr_{1.75}Nb_{0.25}O_{12}$ (1050 °C/12 h) [67]	Not reported	925; Galvanostatic cycling at 0.05 mA cm^{-2}, 5 or 10 min/Li plate or strip: fluctuating voltage, high voltage hysteresis, short cycle life	115; Modification: Ge thermal evaporation; Galvanostatic cycling at 0.025–0.1 mA cm^{-2}, 5 or 10 min/Li plate or strip: stable over 150 h at 0.025 and 0.05 mA cm^{-2}.
$Li_7La_{2.75}Ca_{0.25}Zr_{1.75}Nb_{0.25}O_{12}$ (1050 °C/12 h) [35]	2.2 x 10^{-4}	1710; Galvanostatic cycling at 0.1 mA cm^{-2}, 30 min/plate or strip: noisy potential with large voltage polarization	1; Modification: Al_2O_3 coating via ALD; Galvanostatic cycling at 0.1–0.2 mA cm^{-2}, 30 min/plate or strip: stable response in both directions

[a] ALD – atomic layer deposition, PECVD – plasma enhanced chemical vapour deposition, , Ri – interfacial resistance between the Li metal and electrolyte at RT under Ar. RT – room temperature (22–25 °C), σ_{Total} – total conductivity. *R_i estimated by subtracting the resistance of electrolyte from a total resistance and multiplying by area. All compositions were synthesized by ceramic synthesis (unless a different method is written) and the final temperature is indicated in parenthesis in the first column. The electrochemical cell configuration is Li|garnet|Li.

The most effective technique to increase the wettability of Li onto the garnet surface is atomic layer deposition (ALD) of Al_2O_3, which decreased the interfacial resistance from 1710 Ω cm^2 to 1 Ω cm^2 [ref. [35]]. Figure 2.11 schematically shows the interfacial nonwetting and wetting of Li onto the garnet surface at the microscopic level.

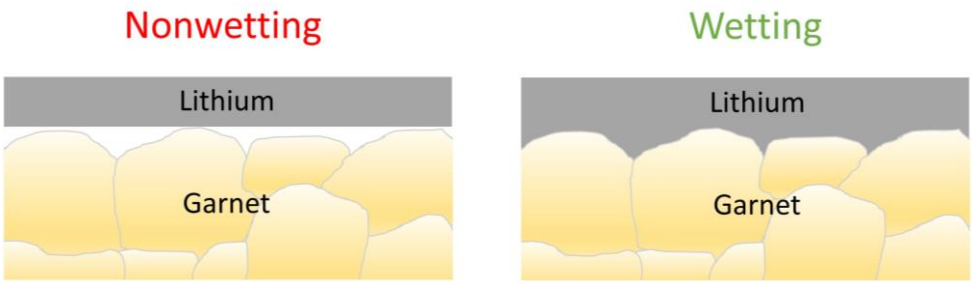

Figure 2.11 Lithium wettability onto the garnet surface. The nonwetting surface leaves lithium in point contact with the garnet surface, where the wetting surface allows lithium to be in full contact with the garnet surface.[5, 35]

Chapter 4-6 will aim to address the chemical and electrochemical stability of lithium garnet-type metal oxides in regards to aqueous (e.g., water, D_2O and Li salt solutions; Chapter 4), metallic Li (Chapter 5), and gaseous (e.g., CO_2 and H_2O; Chapter 6).

Chapter Three: **Experimental methods**

3.1 Material preparation

3.1.1 Material synthesis

Lithium-rich garnet-type $Li_{6.5}La_{2.5}Ba_{0.5}ZrTaO_{12}$ (Chapters 4 and 6) and $Li_7La_{2.75}Ca_{0.25}Zr_{1.75}Nb_{0.25}O_{12}$ (Chapters 5 and 6) were prepared using conventional solid-state (ceramic) methods using stoichiometric quantities of $LiNO_3$ (99%, Alfa Aesar), La_2O_3 (99%, Alfa Aesar), $Ba(NO_3)_2$ (98%, Alfa Aesar) or $Ca(NO_3)_2$ (>99% Alfa Aesar), ZrO_2 (99%, Alfa Aesar) and Ta_2O_5 (99%, Alfa Aesar) or Nb_2O_5 (99%, Alfa Aesar). 10 wt% excess of $LiNO_3$ was added to compensate for Li_2O volatilization during high temperature sintering. Due to the hygroscopic nature of La_2O_3, the powder was pre-heated at 900 ^oC for 12 h to remove any moisture. All other precursors were used as is from the manufacturer. Precursors powders were combined in 80 ml zirconia ball mill jars along with 6 (10 mm diameter) zirconia balls and 2-propanol. Powders were mixed using a Pulverisette, Fritsch, Germany ball mill at 200 rpm for 6 h to ensure homogenous mixing. The 2-propanol was evaporated in an 80 ^oC air oven, dried powders were transferred to clean alumina crucibles and capped with an alumina cover. Contents were heated to 700 ^oC for 6 h (10 ^oC/min) to decompose nitrates and form oxides. Resulting powders were ball milled a second time in the same manner as the first milling step. Dried powders were isostatically cold pressed in rubber molds using a P.O. Weber press at a pressure of 150 MPa for 1 min to form rod-shaped (approx. diameter 10 mm and length 20 mm) green powders. In addition to rod geometry, crucible shaped garnets ceramics were formed. To do so, a quartz rod was inserted into the middle of the rubber mold to create a hollow cavity. Garnet rods and crucibles were placed on a garnet mother powder bed within a clean alumina crucible and further covered with garnet mother powder. The additional mother powder around the rods and crucibles was to reduce the Li_2O volatilization at

high temperatures. Finally, rods and crucibles were sintered in ambient air in a two-step process, samples were heated to 900 ^{o}C for 24 h (5 ^{o}C/min) then directly heated to 1100 ^{o}C for 6 h-12 h (5 ^{o}C/min) and naturally cooled to approx. 300 ^{o}C - 400 ^{o}C before removing and transferring to a desiccator or glovebox. Rods were cut into pellets 1-2 mm thick using a Buehler IsoMet 5000 diamond saw. The reaction scheme is shown in Figure 3.1.

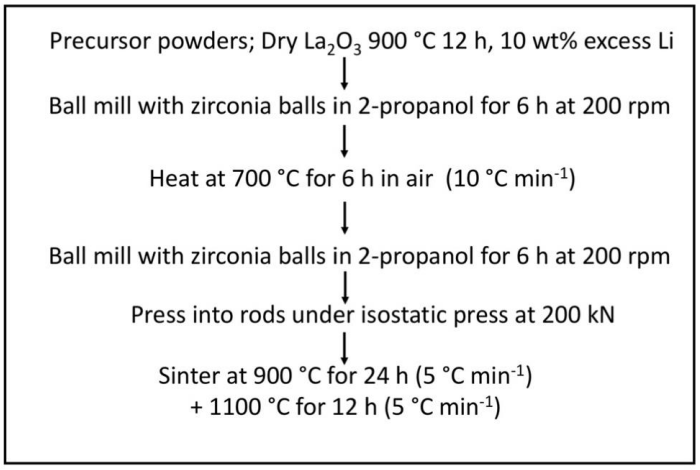

Figure. 3.1 Schematic reaction pathway of solid-state (ceramic) synthesis of lithium-garnets.

3.1.2 Ion-exchanged samples

To evaluate the Li^{+}/H^{+} ion-exchange under various aqueous media, sintered garnet rods were cut into pellets approx. 1 mm thick and 10 mm in diameter. Pellets were placed in closed vials with 20 mL of water, D_2O, 1 M LiOH, 1 M LiCl, or brine (0.1 M LiCl, 0.1 M $NaNO_3$, 0.1 M K_2CO_3) for 5 to 10 days at room temperature. Powdered samples were tested to encourage excessive Li^{+}/H^{+} ion-exchange, in this case, sintered garnet pellets were crushed to a fine powder and stirred in solution at room temperature. Approximately 5 g of garnet powder was stirred in 20 mL solution, the solution was refreshed every 48 h for a total immersion time of 7 days. After solution treatment,

powders and pellets were vacuum filtered, washed with 2-propanol, and dried under vacuum. Samples were kept in desiccators for further analysis.

3.2 Powder X-ray diffraction

Powder X-ray diffraction is one of the most powerful techniques used in solid-state chemistry for crystal (or amorphous) phase characterization. X-Ray diffraction can be used to determine crystal structure, phase formation, and crystallite size and density. For the X-ray generation, a beam of high energy electrons (40 kV) hit a metal surface, typically Cu or Mo causing an electron from the K-shell to be ejected, an electron from the L-shell will immediately fall in energy and fill the hole, as a result, a near monochromatic X-ray is formed; in the case of Cu the K_α wavelength is 1.5418 Å. Due to varying spin states of electrons, $K_{\alpha 1}$ (λ = 1.5405 Å) and $K_{\alpha 2}$ (λ = 1.5443 Å) are generated. In addition, electrons from M-shell can also fall into the ejected K-shell electron leading to K_β generation. A Ni-filter is generally used to absorb this K_β radiation.

X-ray diffraction from crystalline lattice planes occurs when Bragg's law is satisfied, as such the X-rays diffracted off crystal planes must undergo constructive interference rather than destructive interference. Bragg's law is as follows:

$$n\lambda = 2d\sin\theta \tag{3.1}$$

where n, λ, d, and θ are the order of diffraction, the wavelength, inter-planar distance (d-spacing), and Bragg angle (angle of incidence), respectively. Figure 3.2 schematically depicts Bragg's law with two crystal planes.

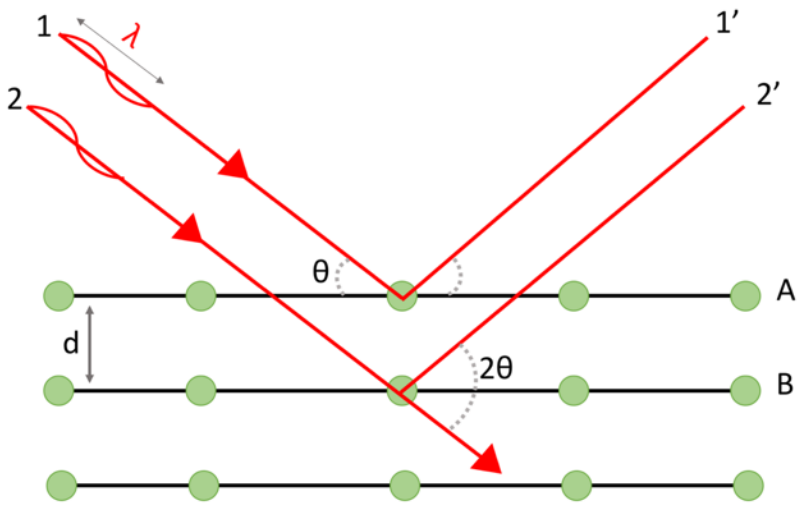

Figure 3.2 Schematic of X-ray diffraction of beams 1 and 2 diffracting off crystal planes A and B, separated by a spacing d. Bragg's law must be satisfied for diffracted beams 1' and 2' and occur.

A sample will be scanned over a 2θ range where Bragg's law is satisfied. A diffraction pattern will be generated in crystalline materials, where each peak will correspond to a given d-spacing. These d-spacing can further be analyzed to determine the crystal structure and indexed to give unit cell parameters. Variable temperature XRD (VT-XRD) can also be implemented to confirm crystal structure retention or destruction at elevated temperatures. In this situation, the samples were heated in-situ using a high-temperature reactor chamber (Anton Paar XRK 900) allowing for the X-ray diffraction pattern to be collected at the elevated temperature.

3.3 Electrochemical characterization

3.3.1 Electrochemical impedance spectroscopy

To understand the electrical properties of ionically conducting materials, AC electrochemical impedance (EIS) is a powerful technique. The impedance of a material is measured over a given frequency range (100 mHz to 1 MHz in this thesis) by applying an external perturbation (100 mV

in this thesis). Due to the distinctive variance in capacitance, impedance attributed to bulk, grain-boundary and interfacial charge transfer can be determined.[68]

Impedance is a complex function of resistance (R) and capacitance (C) which is dependent on the applied angular frequency (ω), described by the following equation:[68]

$$\omega_{\max} RC = 1 \tag{3.2}$$

where $\omega = 2\pi f$, f is the frequency of the AC potential. The capacitance of a materials bulk, grain-boundary, and interfacial charge transfer are in the range of 10^{-12}, 10^{-11} – 10^{-8}, and 10^{-7} – 10^{-5} F, respectively.[68, 69] A schematic of a polycrystalline electroceramic with blocking electrodes is shown in Figure 3.3a, with an corresponding ideal Nyquist plot shown in Figure 3.3b, with an RC equivalent circuit shown in the inset. Similarly, Figure 3.4a schematically shows a polycrystalline electroceramic with reversible electrodes and the corresponding ideal Nyquist plot shown in Figure 3.4b. Ideal capacitance can be calculated using the following equation:[68]

$$C = \varepsilon_o \varepsilon_r \frac{a}{l} \tag{3.3}$$

where ε_0 is the vacuum permittivity (8.854 x 10^{-12} F m^{-1}), ε_r is the relative permittivity of the material, a is the area of electrode, and l is the distance between the electrodes. However, due to surface roughness and contamination the capacitance is not ideal. In this case a constant phase element, CPE is used instead of C.[70] In this case, the capacitance can be calculated using equation:

$$C = R^{\left(\frac{1-n}{n}\right)} CPE^{\left(\frac{1}{n}\right)} \tag{3.4}$$

where R is the resistance, and n is a value between 0 and 1. In the case of a pure capacitor n = 1 therefore C = CPE.

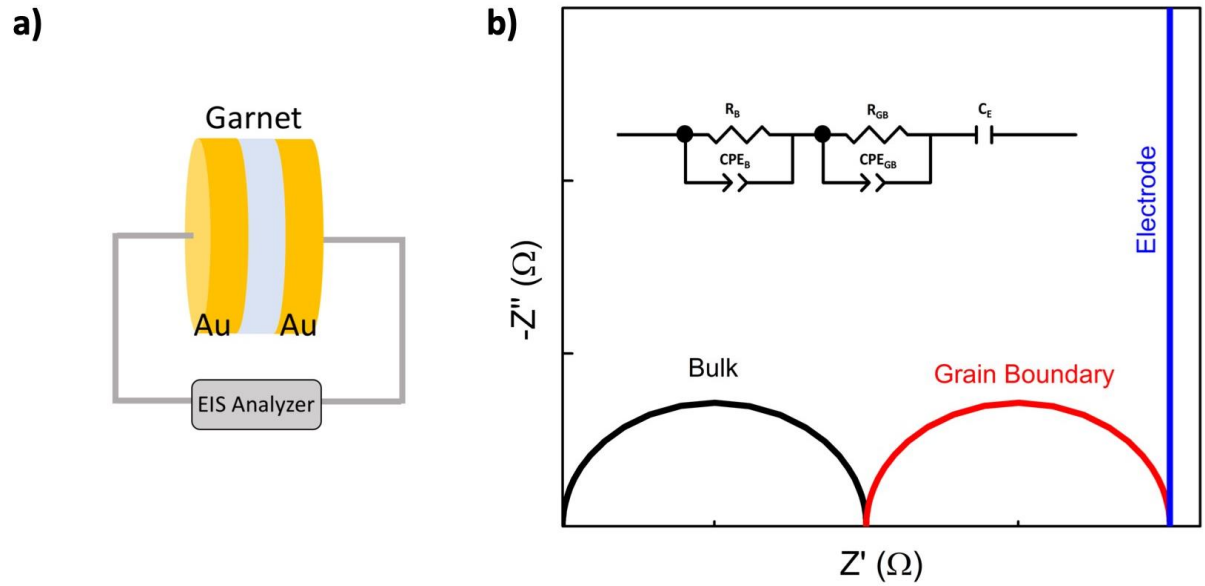

Figure 3.3. a) Schematic representation of electroceramic with Au blocking electrodes. b) Simulated Nyquist plot highlighting bulk, grain boundary, and electrode contributions. Inset shows equivalent circuit (R_BCPE_B)($R_{GB}CPE_{GB}$)C_E.

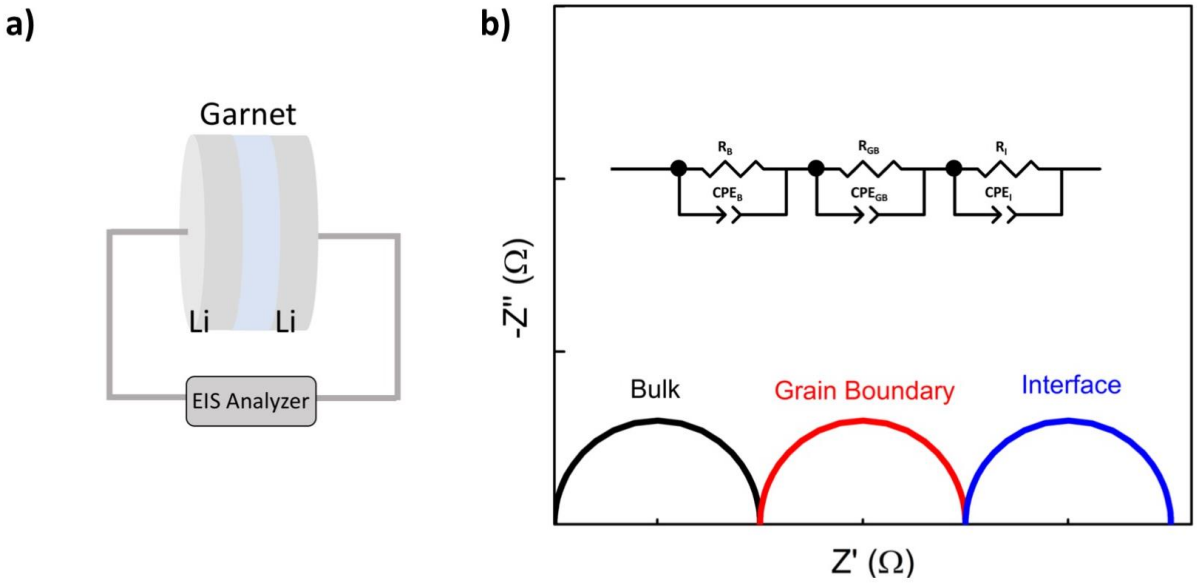

Figure 3.4. a) Schematic representation of electroceramic with Li reversible electrodes. b) Simulated Nyquist plot highlighting bulk, grain boundary, and interfacial charge transfer contributions. Inset shows equivalent circuit (R_BCPE_B)($R_{GB}CPE_{GB}$)(R_ICPE_I).

The ionic conductivity of the samples calculated from the following equation:

$$\sigma = \left(\frac{1}{R}\right)\left(\frac{l}{a}\right) \tag{3.5}$$

where R is the resistance, l is the thickness of the pellet, and a is the pellet area. Conductivity is dependent on temperature, that follows the Arrhenius equation:

$$\sigma T = A\exp^{\left(-\frac{E_a}{kT}\right)} \tag{3.6}$$

where T is the temperature in kelvin, A is the pre-exponential term, E_a is the activation energy, and k is Boltzmann's constant.

In this thesis, EIS measurements were conducted on a Solartron SI 1260 impedance and gain-phase/analyzer and a Princeton Applied PARSTAT 3000. Garnet pellet samples for impedance measurements were prepared by polishing garnet surfaced with varying polish papers, a final grit of 1500 was used. Samples were sonicated in 2-propanol and dried in an 80 ^{o}C air oven. For $Li_{6.5}La_{2.5}Ba_{0.5}ZrTaO_{12}$ samples, Au was painted onto the opposing sides, with a minimum of 3 coats, the paste was dried between coats by placing the samples in an 80 ^{o}C air oven. Final curing was done by heating the samples to 700 ^{o}C for 1 h to remove an organic binder within the gold paste and form a porous conductive coating. For $Li_7La_{2.75}Ca_{0.25}Zr_{1.75}Nb_{0.25}O_{12}$ samples, Au was sputtered to a thickness of approx. 30 nm on opposing sides. To measure impedance as a function of temperature, samples were temperature controlled with a tubular furnace. After each temperature change, samples were left for a minimum of 1 h to ensure thermal equilibrium.

3.3.2 Cyclic voltammetry

Cyclic voltammetry studies were performed to evaluate the electrochemical stability window (ESW) of the garnet materials. A two-electrode setup was used, using Au and Li as the working electrode (WE) and reference/counter electrode (RE/CE), respectively. Garnet samples were

polished in the same manner as EIS measurements, Au was sputtered onto one side of the pellet and transferred to an argon-filled glovebox. Li granules were rolled and a Li disc was punched out. Li was melted on top of the bare garnet side at 200 ^{o}C for 1 h and naturally cooled. A scanning rate of 1 mV s^{-1} between -0.5 to 6 V vs Li/Li^{+} for 1-5 cycles. A Solartron 1287 electrochemical interface was used for CV studies.

3.3.3 Hebb-Wagner polarization

Hebb-Wagner (HW) polarization was performed to differentiate ionic and electronic conductivity. For these measurements, electrodes are attached to the electrolyte samples, one electrode must be reversible to both the mobile ions and electrons, while the other must be blocking to the mobile ion. The cell was polarized such that the mobile Li in the electrolyte moves away from the blocking, Au electrode towards the reversible Li electrode. Since the Au electrode cannot supply additional Li-ions, the garnet electrolyte becomes starved of mobile Li-ions hence ionic conduction stops.[71, 72]

Samples were prepared in the same manner as those used for CV studies. A constant potential bias in the range of 0.5 to 6 V was held for 4-24 h to create ion mobility from the blocking Au electrode towards the reversible Li electrode. As the Li-ions become blocked, the steady-state current is due to the movement of electrons and holes. By taking the slope of steady-state current (A cm^{-2}) vs. potential bias (V), the electronic conductivity can be determined. The ionic transference value can be calculated by taking the ratio of ionic conductivity (σ_i) to total conductivity ($\sigma_i + \sigma_e$) as seen in the following equation:

$$t_i = \frac{\sigma_i}{\sigma_i + \sigma_e} \tag{3.7}$$

3.3.4 Plating and stripping DC polarization

Li plating and striping was performed by melting Li onto both sides of a garnet pellet at 180 ^{o}C inside an argon-filled glovebox, several melting cycles were done with fresh Li to ensure a clean surface and uniform contact, the Li was allowed to naturally cool. At 25 ^{o}C, a constant current was applied in the range of 39 – 169 μA cm^{-2} for one minute, at which time the current direction was reversed for 100 cycles. From the voltage hysteresis, the total resistance of the cell can be calculated using Ohm's law:

$$V = IR \tag{3.8}$$

where V is the stable potential, I is the applied current, and R is the total resistance. By knowing the resistance contribution from the electrolyte (from EIS), the area specific (interfacial) resistance (ASR) can also be calculated:

$$interfacial\ resistance = \left(\frac{total\ resistance - electrolyte\ resistance}{2}\right) * area \tag{3.9}$$

the factor of 2 accounts for the symmetric cell design, so the ASR of only one interfacial side is calculated.

3.4 Thermogravimetric analysis and mass spectroscopy

Thermogravimetric analysis (TGA) is used to measure weight change as a function of temperature. Results can give suggestion towards material decomposing, gas uptake, or redox reactions. Analysis can be done under various atmospheres such as N_2, Ar, O_2, H_2, CO_2, humidified air, or any combination of these gases but not limited to these gases. Weight losses can be single step, multistep, or not present at all, a lack of weight change can suggest the material is stable over that given temperature range. TGA measurements were used to determine the extent of ion-exchange

in protonated garnets. Using a Mettler Toledo Thermal Analysis TGA/DSC1/1600HT, < 10 mg of garnet powder was placed into a 70 µL alumina crucible, which was transferred into the reaction furnace. Samples were heated from 30 – 900 ^{o}C or 30 – 1000 ^{o}C at 5 ^{o}C min^{-1} or 10 ^{o}C min^{-1} under 50:50 air:N_2. Samples were cooled back to 30 ^{o}C at the same heating rate, typically a second cycle was performed to confirm stability. A blank measurement with an empty alumina crucible was done and subtracted from experimental data to account for buoyancy effects of the crucible. Mass spectroscopy (MS) was used to confirm the presence of water and CO_2 in the TGA exhaust gas using a Pfeiffer Vacuum (Asslar, Germany). When coupled with the mass spectrometer, a SDT-Q600 TGA was used with the same heating/cooling rates.

3.5 Microscopy imaging

3.5.1 Scanning electron microscopy

Size and morphology of the garnet particles were characterized by a Zeiss Sigma VP or FEI Quanta FEG 250 scanning electron microscope. Scanning electron microscopy relies on high energy electrons (0.1-30 keV) hitting the surface of a material under vacuum, as a result, secondary and backscattered electrons along with X-rays and light are ejected/emitted. The secondary and backscattered electrons are collected by the detector to form micrographs, with a resolution limit approx. 10 nm. Electron imaging of pre- and post-solution treatment can reveal morphological changes within the samples.

For SEM analysis in this thesis, garnet pellets were attached to an aluminum block using carbon tape. Pellets were either attached as is for surface characterization or broken in half for cross-sectional imaging in high vacuum using Zeiss Sigma VP, Nanoscience program, University of Calgary. Environmental scanning electron microscopy was performed using an FEI Quanta FEG

250 in IFFAEM lab, Department of Geoscience, University of Calgary. This technique allows for humidity-controlled SEM imaging to be performed.

3.5.2 Transmission electron microscopy and selected area electron diffraction

Transmission electron microscopy (TEM) was used to confirm structural stability at the atomic level of the garnet samples using a Tecnai F20, Microscopy and Imaging Facility of the Health Sciences Centre, University of Calgary. In TEM, high energy electrons (60-300 keV) are focused on a thin sample, these electrons will either reflect off the sample or transmit through the sample. The transmitted electrons are collected to form an image. High-resolution transmission electron microscopy (HR-TEM) can be used to resolve features of the scale of 0.1-1 nm. Selected area electron diffraction (SAED) patterns were collected confirming crystal structure. SAED relies on electrons diffracting off atom planes that satisfy Bragg's law. The resulting diffractogram shows spots, each corresponding to a d-spacing and crystal plane within the structure. In the case of amorphous or polycrystalline materials, rings tend to form rather than individual spots.

3.5.2 Atomic force microscopy

Atomic force microscopy (AFM) was used to image the surface topography of garnet samples in ambient and humid conditions using an Agilent Technologies 5500, Nanoscience program, University of Calgary. There are two primary image techniques in AFM 1) contact mode, where a cantilever with a sharp tip is dragged over the surface of material. 2) tapping mode, where the cantilever is oscillated over the sample, continuously tapping the surface. A laser is directed to the end of the cantilever, as the cantilever modes over the surface the raised and lowered topographical features influencing the deflection of the laser, which is monitored by position-sensitive photodiode.

3.6 Error considerations

- During material preparation impurities may be present in precursor materials. Precursors were not purified once received from manufacturer as purity was ~99 %. Volatilization of Li_2O at high temperatures may have occurred, an excess 10 wt% Li salt was added during initial weighing to accommodate for loss. A common practice in synthesis of lithium-garnets.[73, 74]
- Lithium-garnet chemical compositions are stoichiometrically based off fixed amounts of Ca/Ba, La, Zr, Nb/Ta, and O content.
- Sintering of pellets was done in alumina crucibles and Al contamination may have occurred. To reduce Al contamination and Li loss, pellets were placed on mother powder beds in the crucibles and pellets were further covered with mother powder.[75]
- Ionic conductivities are known to differ from sample to sample, therefore exact conductivities are unknown, rather approximate ionic conductivities of 10^{-5} - 10^{-4} S cm^{-1} are accepted for compositions in this thesis. Figure 3.5 highlights various reported temperature dependent ionic conductivities for $Li_7La_3Zr_2O_{12}$ materials.
- Ion-exchange calculations assume the sample is pure garnet material, not accounting for Al contamination or potential Li loss and/or other impurities.
- Samples immersed in solution were not held at a specific temperature, rather ambient temperatures were used which fluctuate from day to night.
- Pellets were not perfectly circular, measurements were done with digital calipers. Multiple diameter and thickness measurements were done and average dimensions were used.

- X-Ray diffraction has a detection limit of 5 %, allowing for undetected impurities to be present, such as Al-based contaminants.
- The Mettler Toledo TGA/DSC1/1600HT TGA furnace has an error of ±0.5 ^{o}C and a balance error of ±1 µg.
- Author takes responsibility for any oversight in data interpretation.

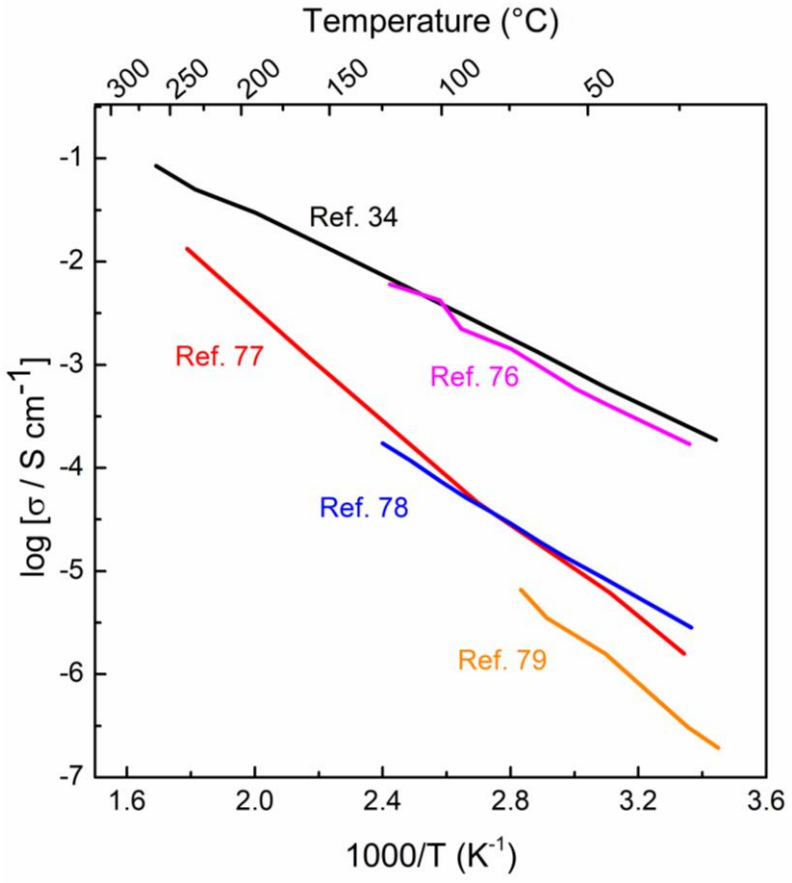

Figure 3.5. Comparison of total Li-ion conductivity of $Li_7La_3Zr_2O_{12}$ garnet-type materials reported in literature.[34, 76-79]

Chapter Four: **Aqueous stability of lithium-garnet $Li_{6.5}La_{2.5}Ba_{0.5}ZrTaO_{12}$**

Contents of this chapter reproduced from the published work, "Characterization of lithium-rich garnet-type $Li_{6.5}La_{2.5}Ba_{0.5}ZrTaO_{12}$ for beyond intercalation chemistry-based lithium-ion batteries" by Kyle Hofstetter, Alfred Junio Samson, and Venkataraman Thangadurai, *Solid State Ionics*. 2018, 318, 71-81. Garnet-type $Li_{6.5}La_{2.5}Ba_{0.5}ZrTaO_{12}$ has been selected for aqueous stability as this composition has previously been optimized by our group.[80, 81]

4.1 General overview

Lithium-garnet materials have shown high promise for solid (ceramic) Li-ion conducting materials. Many lithium-garnets compositions have desirable properties including high Li-ion mobility (> 1 mS cm^{-1}) at room temperature[82], thermally stable, stability with Li, and large electrochemical stability windows (ESW; up to 9 V vs. Li/Li^+).[58] Solid electrolytes are also believed to be the key aspect to accessing Li-O_2 battery chemistry. In aqueous Li-O_2 cells, the Li anode must be separated from the aqueous electrolyte, requiring a protective layer. Solid electrolytes can be used as the protective layer in aqueous Li-O_2 batteries assuming the solid electrolyte is chemically stable with Li and the aqueous media simultaneously.

In this chapter, $Li_{6.5}La_{2.5}Ba_{0.5}ZrTaO_{12}$ (LLBZT) is studied for its stability in aqueous media including water, D_2O, 1 M LiOH, 1 M LiCl, and a brine solution (0.1 M LiCl, 0.1 M $NaNO_3$, 0.1 M K_2CO_3) to understand the effects of Li^+/H^+ ion-exchange on crystal structure, mechanical integrity, and ionic conductivity. X-Ray diffraction patterns after solution treatment show that the crystal structure is retained, deep crystal structure studied with electron diffraction further agreed that the garnet crystal structure is retained. Scanning electron microscopy images show that small morphological changes after treatment with 1 M LiOH and 1 M LiCl compared to as-prepared

samples, other media treatments do not show the same morphological changes. HR-TEM images show ordered crystallinity before and after media treatment. Electrochemical impedance measurements were taken daily, revealing that the garnet samples increase in conductivity after 1 day and stabilize thereafter (measured for 10 consecutive days).

4.2 Results and discussion

4.2.1 Condensed bulk $Li_{6.5}La_{2.5}Ba_{0.5}ZrTaO_{12}$ pellet stability in aqueous solution

For the purpose of this study, lithium-garnets were kept in a sintered, condensed pellet form for aqueous solution treatment.

4.2.1.1 Phase characterization of protonated $Li_{6.5}La_{2.5}Ba_{0.5}ZrTaO_{12}$ in bulk pellet geometry

Pellets (approx. 10 mm in diameter x 1 mm thick) were soaked in either 20 ml water, D_2O, 1 M LiOH, or 1 M LiCl for 5 days at room temperature. Powder X-ray diffraction patterns of $Li_{6.5}La_{2.5}Ba_{0.5}ZrTaO_{12}$ were collected before and after aqueous solution treatment (Figure 4.1). In all cases, after solution treatment, the characteristic cubic lithium-garnet peaks are retained. Similar results were obtained for pellets soaked in brine (0.1 M LiCl, 0.1 M $NaNO_3$, 0.1 M K_2CO_3) solution for 10 days, seen in Figure 4.2. Simulated pattern of parent $Li_5La_3Nb_2O_{12}$ phase shown for comparison.

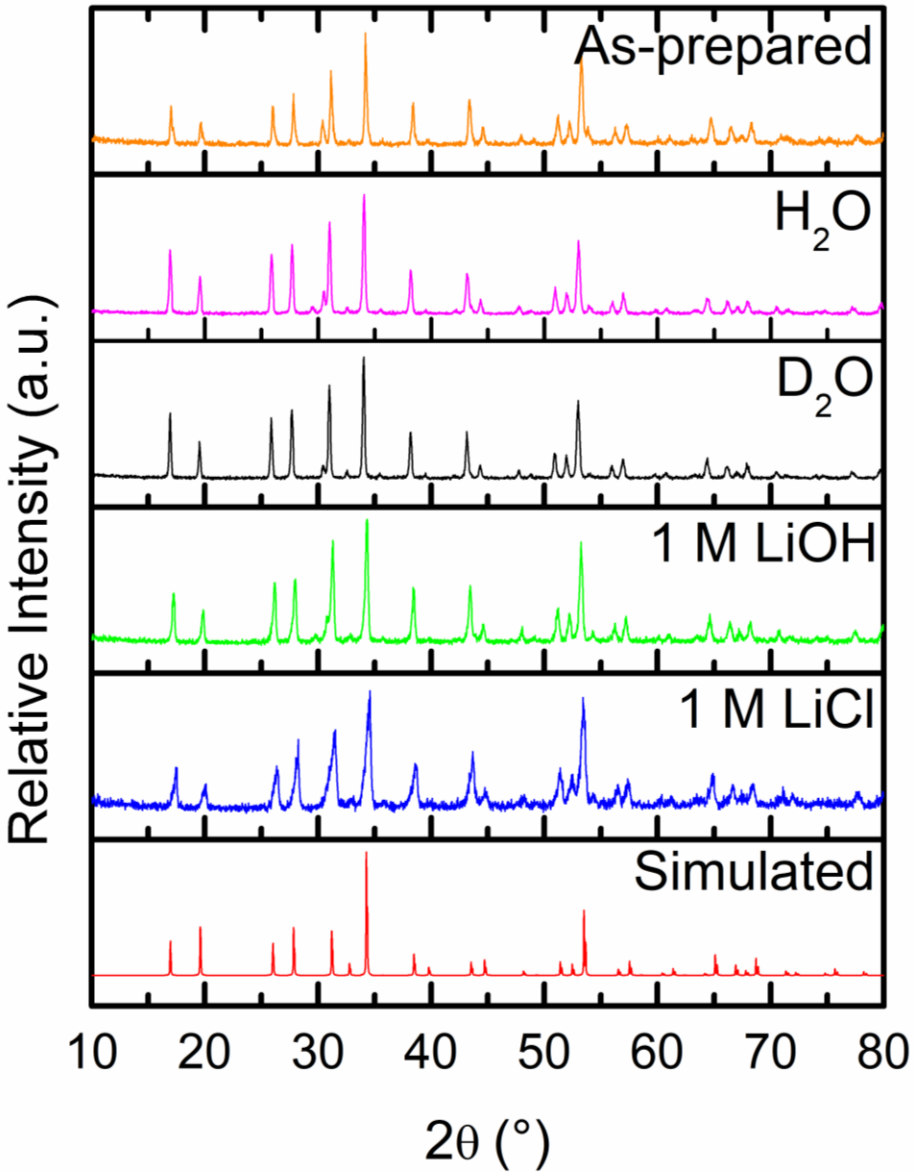

Figure 4.1 Powder X-ray diffraction (PXRD) patterns of $Li_{6.5}La_{2.5}Ba_{0.5}ZrTaO_{12}$ sample after soaking in as-prepared, water, D_2O, 1 M LiOH, and 1 M LiCl for 5 days. For comparison simulated PXRD of the parent, $Li_5La_3Nb_2O_{12}$ garnet phase is shown in (f). Reprinted (adapted) with permission from Hofstetter, K.; Samson, A.J.; Thangadurai, V. *Solid State Ionics* 2018, 318, 71-81. Copyright (2018), with permission from Elsevier [OR APPLICABLE SOCIETY COPYRIGHT OWNER].

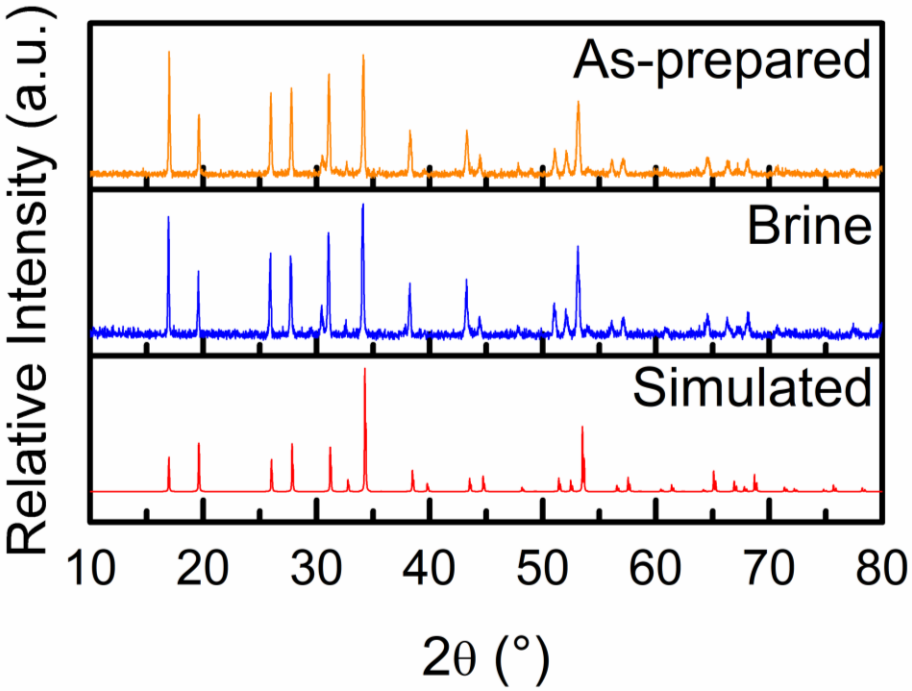

Figure 4.2 Powder X-ray diffraction (PXRD) patterns of $Li_{6.5}La_{2.5}Ba_{0.5}ZrTaO_{12}$ sample before and after soaking in brine (0.1 M LiCl, 0.1 M $NaNO_3$, 0.1 M K_2CO_3) solution for 10 days. Simulated $Li_5La_3Nb_2O_{12}$ garnet phase shown for comparison.

4.2.1.2 Ionic conductivity of protonated $Li_{6.5}La_{2.5}Ba_{0.5}ZrTaO_{12}$ in solution as a function of time

To monitor the effect on ionic conductivity as a function of time in aqueous solution, garnet pellets were painted with porous Au paste on opposing sides to act as current collectors, Figure 4.3a. One side of the sample was fixed to a hollow quartz tube, these tubes were suspended in a 20 ml vial; the desired solution was poured into the tube as well as into the vial, Figure 4.3b shows the symmetric aqueous cell setup.

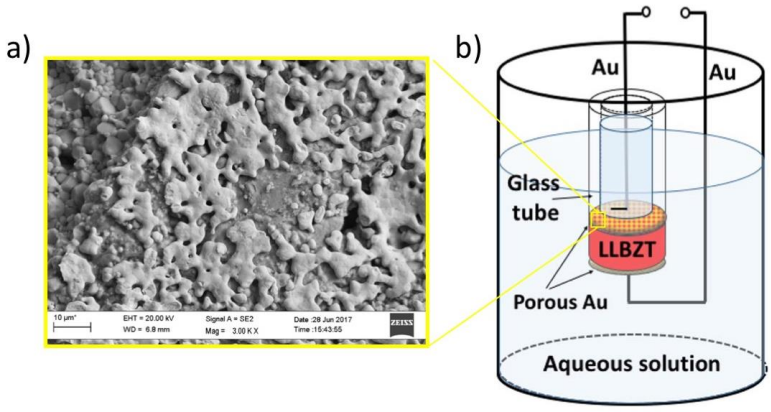

Figure 4.3. a) Scanning electron micrograph of cured porous Au paste on lithium-garnet, $Li_{6.5}La_{2.5}Ba_{0.5}ZrTaO_{12}$. b) Schematic representation of the symmetric aqueous cell used for daily impedance measurements. Reprinted (adapted) with permission from Hofstetter, K.; Samson, A.J.; Thangadurai, V. *Solid State Ionics* 2018, 318, 71-81. Copyright (2018), with permission from Elsevier [OR APPLICABLE SOCIETY COPYRIGHT OWNER].

The in-situ electrochemical impedance spectra was collected daily for 10 days for each solution treated sample (1 MHz – 100 mHz ; 100 mV) at room temperature. The 1 MHz impedance value was used as the bulk resistance value, the ionic conductivity was then determined using equation (3.5). For the given conditions, all four solutions water, D_2O, 1 M LiOH, and 1 M LiCl had shown a decrease in impedance with passing time; increase in conductivity (Figure 4.4).

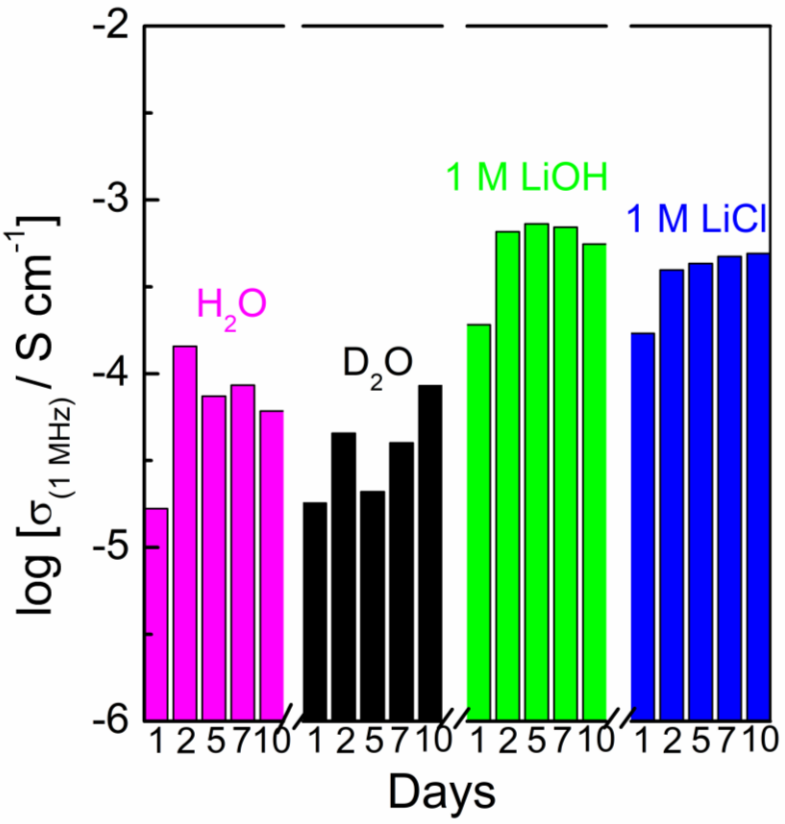

Figure 4.4 Variation of electrical conductivity obtained at 1 MHz for $Li_{6.5}La_{2.5}Ba_{0.5}ZrTaO_{12}$ under water, D_2O, 1 M LiOH and 1 M LiCl at room temperature. Reprinted (adapted) with permission from Hofstetter, K.; Samson, A.J.; Thangadurai, V. *Solid State Ionics* 2018, 318, 71-81. Copyright (2018), with permission from Elsevier [OR APPLICABLE SOCIETY COPYRIGHT OWNER].

The same approach was used to monitor the change in ionic conductivity while $Li_{6.5}La_{2.5}Ba_{0.5}ZrTaO_{12}$ is immersed in a brine solution (0.1 M LiCl, 0.1 M $NaNO_3$, 0.1 M K_2CO_3). Within 4 h, a noticeable decrease in total impedance were observed, after 24 hours the impedance becomes stabilized for the remaining duration. The conductivity of a function of time in brine solution is shown in Figure 4.5.

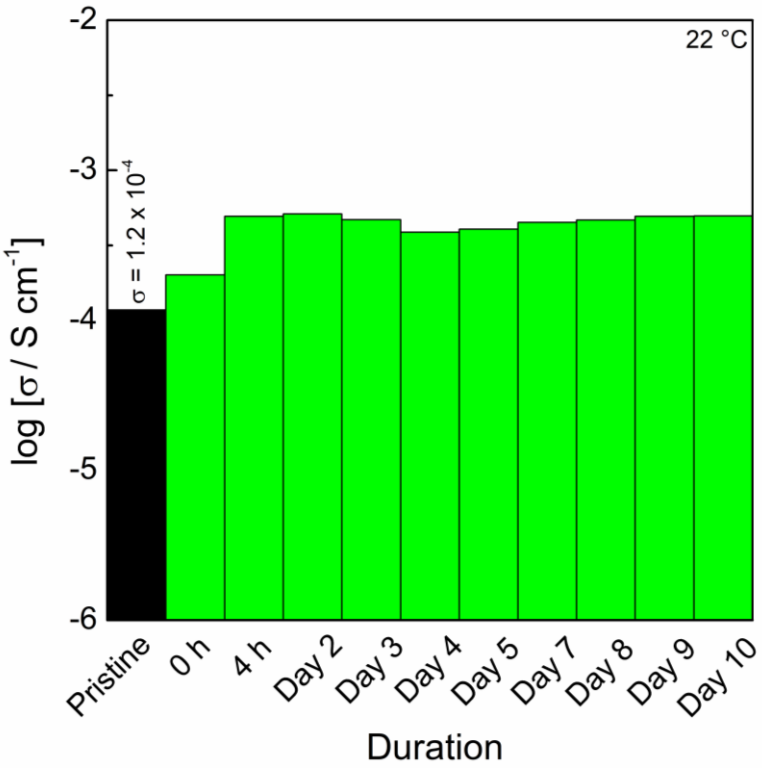

Figure 4.5 Variation of electrical conductivity obtained from total resistance for $Li_{6.5}La_{2.5}Ba_{0.5}ZrTaO_{12}$ in brine (0.1 M LiCl, 0.1 M $NaNO_3$, 0.1 M K_2CO_3) solution for 10 days.

In all cases, an increase in conductivity is observed after the first day. It is worth noting that these conductivity values are still below those of the solutions (10^{-3}-10^{-2} S cm^{-1}), suggesting that the pellet retained mechanical strength and the observed ionic conductivity is due to the garnet pellet rather than the aqueous solution. It should not be ignored that the increase in conductivity may be from the addition of H^+ conduction.

4.2.1.3 Ion-exchange extent in protonated $Li_{6.5}La_{2.5}Ba_{0.5}ZrTaO_{12}$ bulk pellets

To determine the extent of Li^+/H^+ ion exchange that occurred after solution treatment, TGA measurements were employed. $Li_{6.5}La_{2.5}Ba_{0.5}ZrTaO_{12}$ pellets 1 mm in thickness (~10 mm in diameter) were immersed in 20 ml of the given solution in a closed vial at room temperature for 5

days. Following immersion, samples were rinsed with isopropanol to remove excess surface salts that may have accumulated. TGA measurements were performed from 20 – 900 ^{o}C (5 ^{o}C min^{-1}) under 50:50 N_2:air using < 10 mg of sample. For fresh as-prepared samples, a small 0.5 wt% change is observed over the given temperature range, which is attributed to carbonate and moisture adsorption that occurred during the cooling cycle of synthesis (Figure 4.6). For solution treated samples, much more obvious weight losses are seen. When heating adsorbed water loss occurs around 100-250 °C, H^+ release in the form of water around 200–450 °C and CO_2 loss above 550 °C. After exchange, LiOH at the surface of the materials may interact with CO_2 to form Li_2CO_3. For $Li_{6.5}La_{2.5}Ba_{0.5}ZrTaO_{12}$, an anticipated complete exchange would result in a 6.6 wt% loss from 3.25 mols of water:

$$Li_{6.5}Ba_{2.5}Ba_{0.5}ZrTaO_{12} \xrightarrow{Li^+/H^+} H_{6.5}Ba_{2.5}Ba_{0.5}ZrTaO_{12} + 6.5LiOH \quad (4.1)$$

$$2LiOH + CO_2 \rightarrow Li_2CO_3 + H_2O \quad (4.2)$$

For the actual solution treated samples, the weight loss up to 550 ^{o}C was taken to be in the form of water. To confirm that the weight loss was from water and CO_2, exhaust gas from TGA was coupled with a thermal ionized mass spectrometer (TIMS), both water and CO_2 gases were observed at the above mentioned temperatures, as shown in Figure 4.7. The anticipated chemical formula based on the TGA weight loss experiment (Figure 4.6) are as follows:

$$Li_{6.5}Ba_{2.5}Ba_{0.5}ZrTaO_{12} \xrightarrow{H_2O/5\ Days} Li_{3.13}H_{3.37}Ba_{2.5}Ba_{0.5}ZrTaO_{12} \quad (4.3)$$

$$Li_{6.5}Ba_{2.5}Ba_{0.5}ZrTaO_{12} \xrightarrow{D_2O/5\ Days} Li_{4.5}D_2Ba_{2.5}Ba_{0.5}ZrTaO_{12} \quad (4.4)$$

$$Li_{6.5}Ba_{2.5}Ba_{0.5}ZrTaO_{12} \xrightarrow{1M\ LiOH/5\ Days} Li_{3.59}H_{2.91}Ba_{2.5}Ba_{0.5}ZrTaO_{12} \quad (4.5)$$

$$Li_{6.5}Ba_{2.5}Ba_{0.5}ZrTaO_{12} \xrightarrow{1M\ LiCl/5\ Days} Li_{1.39}H_{5.11}Ba_{2.5}Ba_{0.5}ZrTaO_{12} \quad (4.6)$$

Lithium-garnets are known to have more than one Li-ion site, tetrahedral, octahedral, and distorted octahedral sites are reported (this is also discussed in Chapter 3). The multistep weight loss seen for water and 1 M LiCl treated samples is believed to be due to different dehydration energies of octahedral and tetrahedral sites. TGA measurements were performed for two cycles to confirm that the loss was from carbonate and moisture species. To confirm that the weight loss was from carbonate and moisture species rather than the decomposition of the crystal structure, variable temperature XRD (VT-XRD) was performed in tandem. VT-XRD patterns were collected every 100 ^{o}C up to 650 ^{o}C for both heating and cooling directions. Characteristic garnet peaks are observed for all 4 solution treated samples as well as at all temperatures measured, as shown in Figure 4.8. Upon heating, the addition of small peaks can be observed which is believed to be from the sample holder. When heated, a loss of product occurs making the sample holder susceptible to X-ray diffraction.

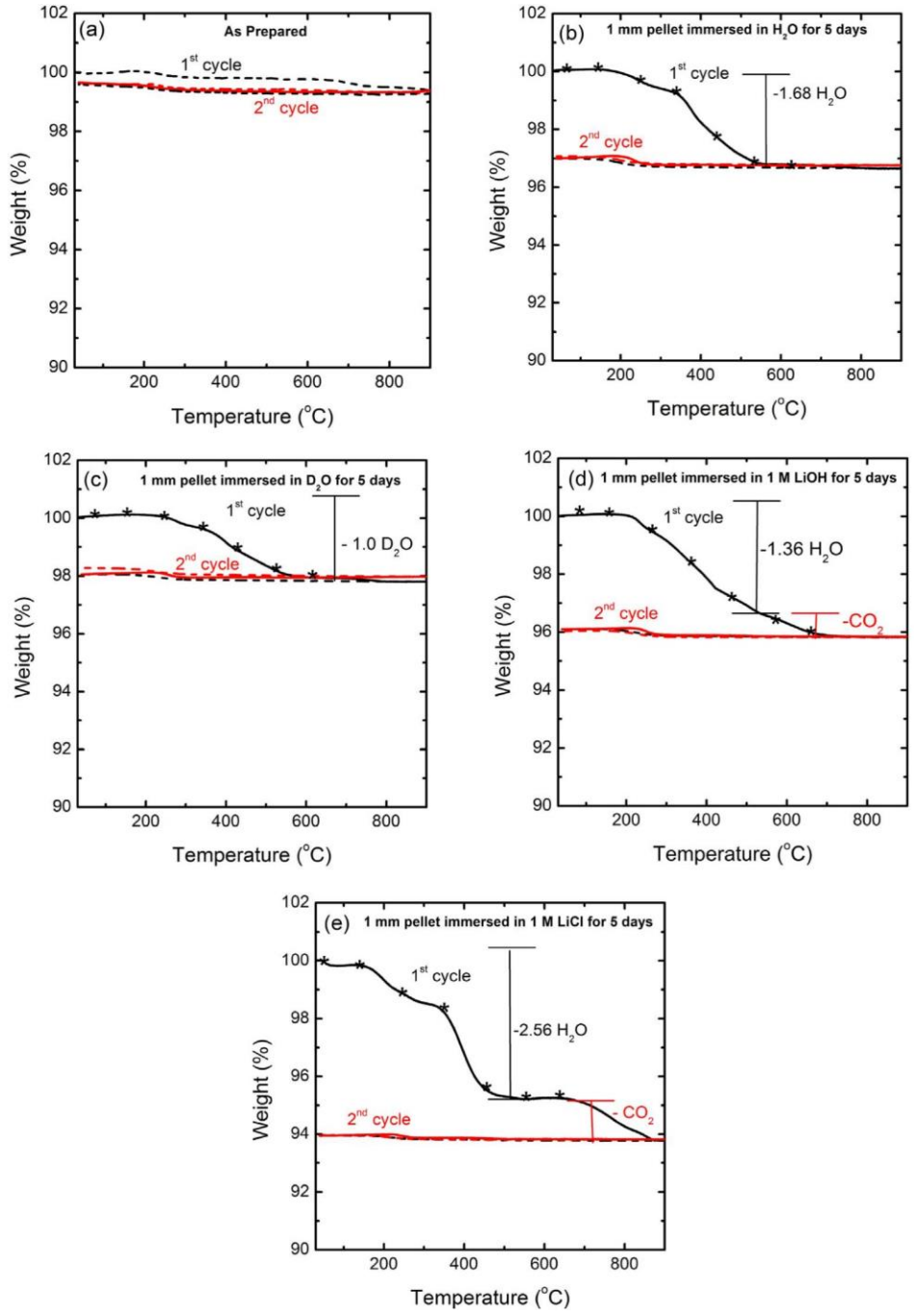

Figure 4.6 TGA curves of LLBZT after the chemical stability test using the solutions employed in AC impedance spectroscopy study. Samples heated at 5 °C min^{-1} under 50/50 N_2/Air. For comparison, TGA of the as-prepared sample is also shown. Asterisks (*) indicate temperatures at which tandem in-situ variable temperature PXRD were performed. Reprinted (adapted) with permission from Hofstetter, K.; Samson, A.J.; Thangadurai, V. *Solid State Ionics* 2018, 318, 71-81. Copyright (2018), with permission from Elsevier [OR APPLICABLE SOCIETY COPYRIGHT OWNER].

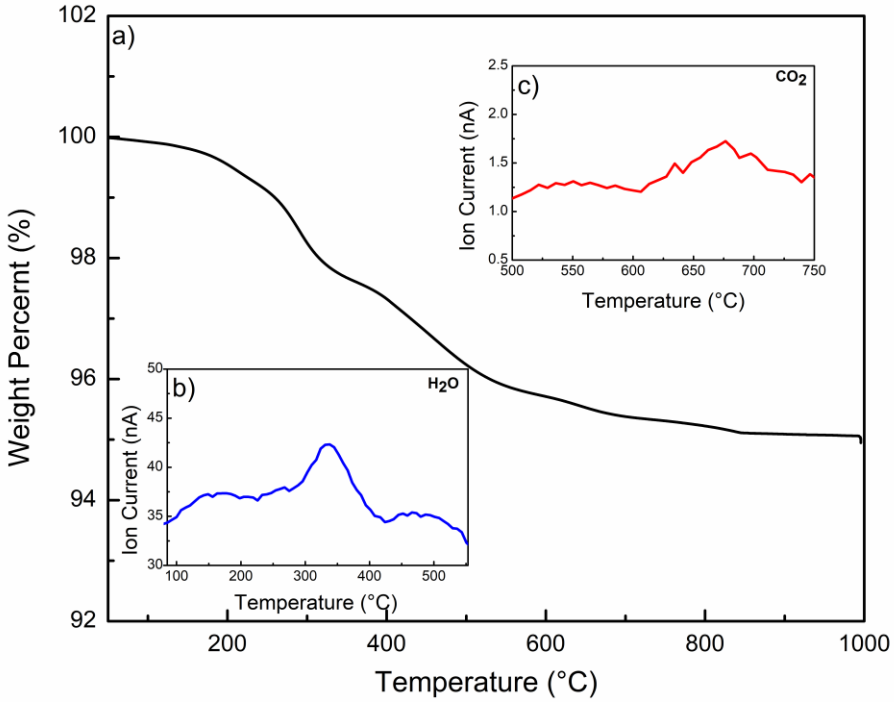

Figure 4.7 a) TGA curves of LLBZT powder after immersing in water for 168 h. Sample heated at 10 ºC min^{-1} under air. Insets b) and c) show ionic current response from mass spectroscopy for water (100-550 ºC) and CO_2 (500-750 ºC), respectively.

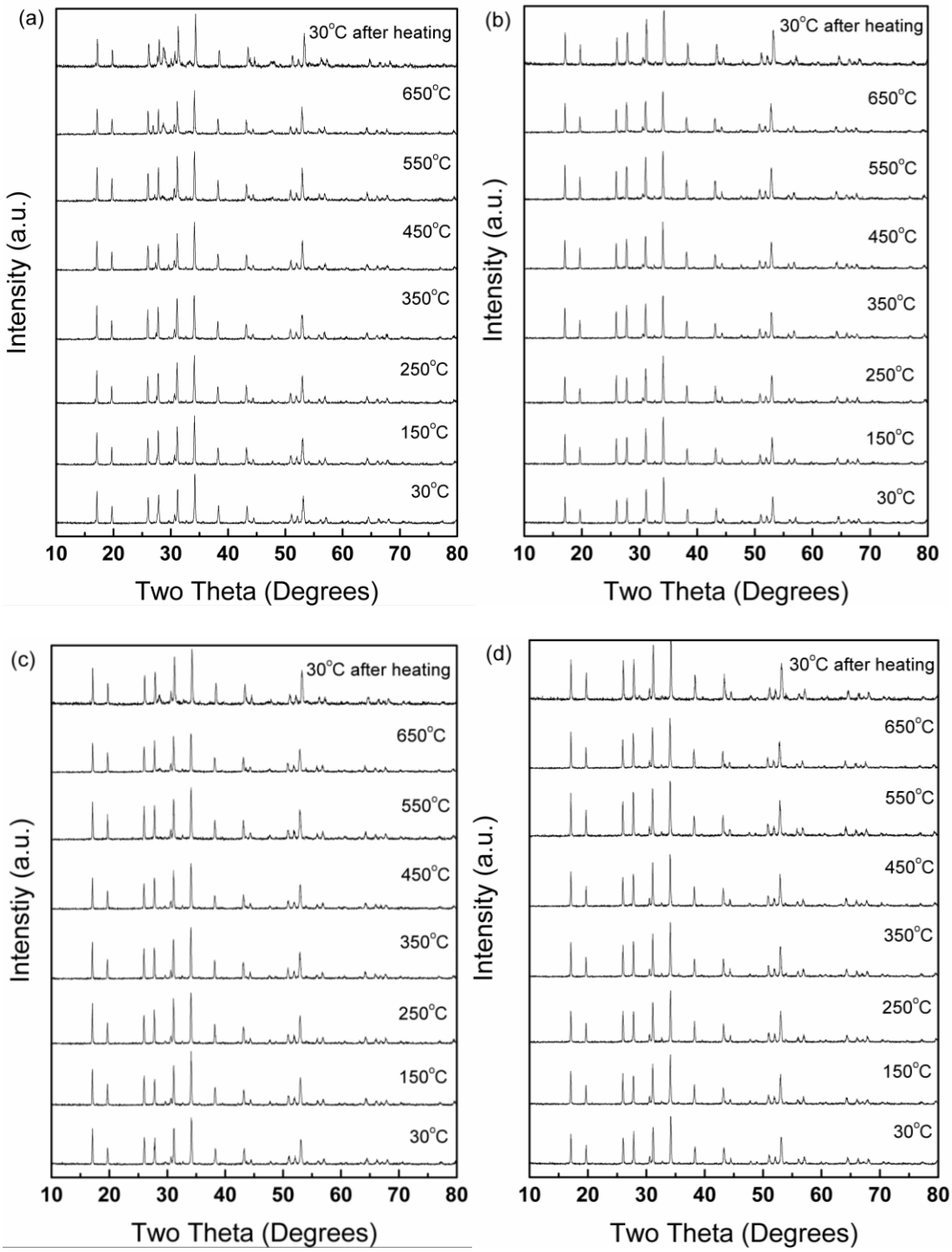

Figure 4.8 In-situ variable temperature powder X-ray diffraction (PXRD) patterns of $Li_{6.5}La_{2.5}Ba_{0.5}ZrTaO_{12}$ sample after soaking in (a) deionized water, (b) D_2O, (c) 1 M LiOH, and (d) 1 M LiCl for 5 days. For comparison, empty sample holder XRD pattern is shown in (e). Reprinted (adapted) with permission from Hofstetter, K.; Samson, A.J.; Thangadurai, V. *Solid State Ionics* 2018, 318, 71-81. Copyright (2018), with permission from Elsevier [OR APPLICABLE SOCIETY COPYRIGHT OWNER].

4.2.1.4 Scanning electron images of protonated $Li_{6.5}La_{2.5}Ba_{0.5}ZrTaO_{12}$ bulk pellets

To investigate the morphology of the $Li_{6.5}La_{2.5}Ba_{0.5}ZrTaO_{12}$ samples before and after solution treatment, scanning electron microscopy (SEM) images were collected, as shown in Figure 4.9. The sample pellets used for TGA investigations were also used for SEM imaging. The as-prepared (Figure 4.9 (1)) sample is consistent with those reported in literature,[83] with grain sizes on the order of 5-10 microns in diameter. Samples treated with water (Figure 4.9 (2)) and D_2O (Figure 4.9 (3)) show similar morphology to that of as-prepared however a thin layer appears to have formed, attributed to Li_2CO_3. Samples treated with 1 M LiOH (Figure 4.9 (4)) and 1 M LiCl (Figure 4.9 (5)) show greater morphological changes. 1 M LiOH treated samples show elongated grains with respect to as-prepared whereas 1 M LiCl treated appear to have agglomerated, forming larger masses.

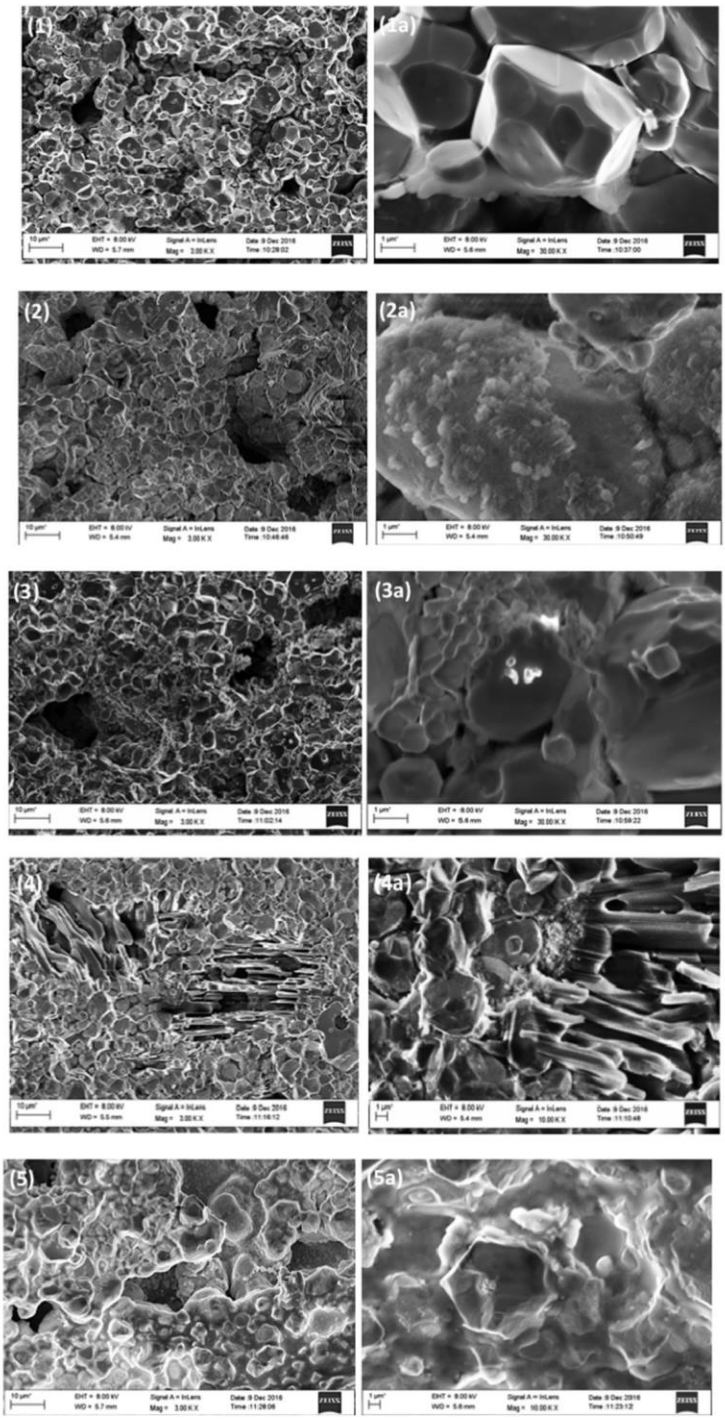

Figure 4.9 Typical scanning electron microscopy (SEM) images of $Li_{6.5}La_{2.5}Ba_{0.5}ZrTaO_{12}$ after and before the chemical stability tests. (1) as-prepared, (2) water, (3) D_2O, (4) 1 M LiOH, and (5) 1 M LiCl. Images (1a)–(5a) show the higher magnification of (1)–(5), respectively. Reprinted (adapted) with permission from Hofstetter, K.; Samson, A.J.; Thangadurai, V. *Solid State Ionics* 2018, 318, 71-81. Copyright (2018), with permission from Elsevier [OR APPLICABLE SOCIETY COPYRIGHT OWNER].

4.2.2 Powder form $Li_{6.5}La_{2.5}Ba_{0.5}ZrTaO_{12}$ stability in aqueous solution

For the purpose of this study, fully sintered lithium-garnets were crushed to powder form to maximize the surface area to volume ratio and to exaggerate the Li^+/H^+ ion-exchange.

4.2.2.1 Phase characterization of protonated $Li_{6.5}La_{2.5}Ba_{0.5}ZrTaO_{12}$ powder form via X-Ray diffraction

Approximately 5 g of powder was stirred in 20 ml of solution (deionized water, D_2O, 1 M LiOH or 1 M LiCl) at room temperature. Solutions were decanted and refreshed every 48 h for a total of 168 h. Samples were then vacuum filtered and rinsed with isopropanol to remove any LiOH or LiCl salts on the surface and completely dried in a vacuum oven overnight. X-ray diffraction patterns, seen in Figure 4.10, before and after solution treatment match those of the parent cubic $Ia\bar{3}d$, $Li_5La_3Nb_2O_{12}$ (PDF 45-0109) indicating that the cubic lithium-garnet structure is retained.

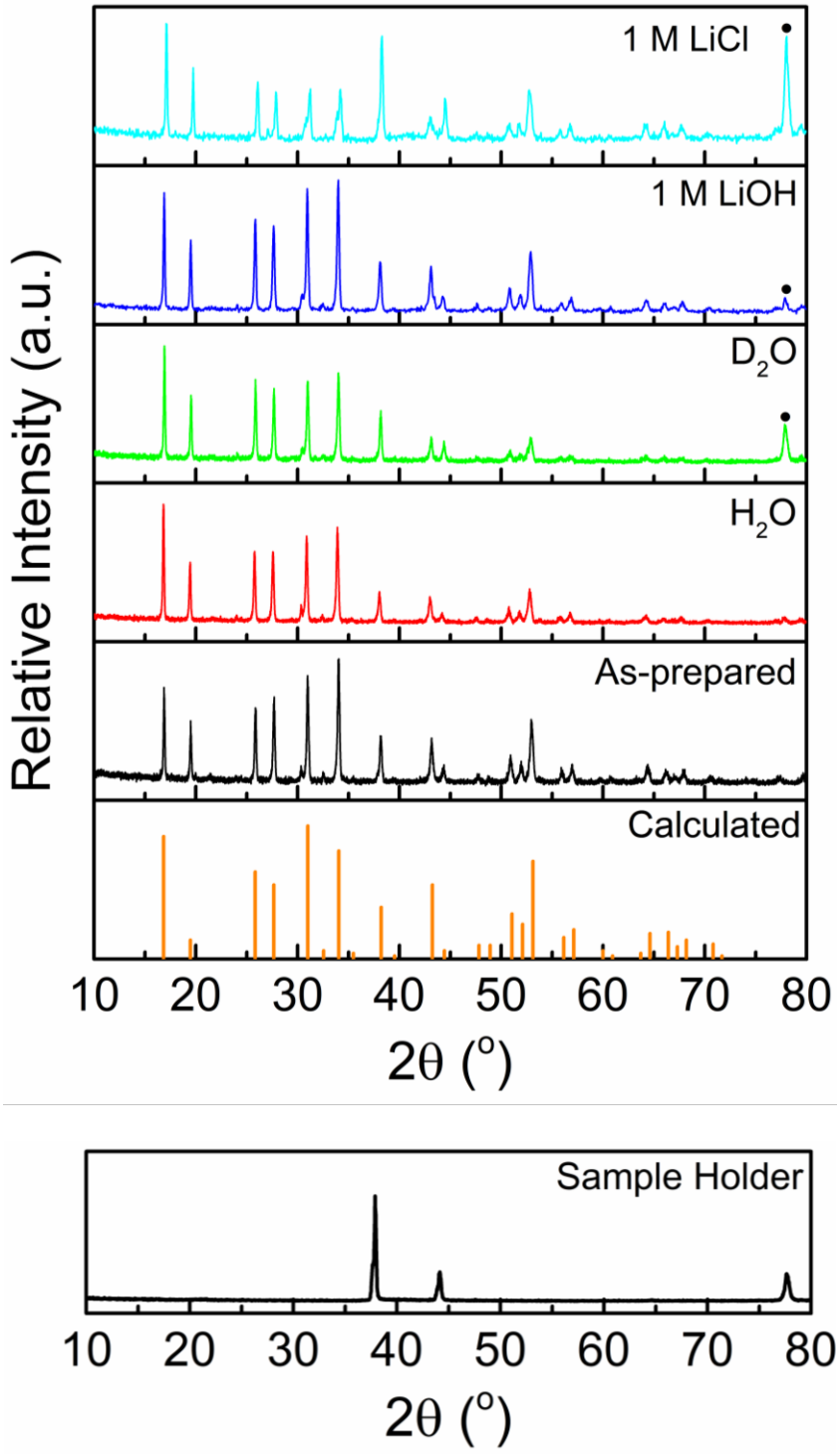

Figure 4.10 Powder X-ray diffraction (PXRD) patterns of $Li_{6.5}La_{2.5}Ba_{0.5}ZrTaO_{12}$ sample after soaking in respective solutions for 168 h. (*) indicates peaks associated with sample holder contributions.

4.2.2.2. Phase and crystallinity characterization of protonated $Li_{6.5}La_{2.5}Ba_{0.5}ZrTaO_{12}$ powder form via selected area electron diffraction and transmission electron microscopy

Transmission electron microscopy (TEM) was successfully performed using a Tecnai F20 for as-prepared and H_2O treated samples. TEM was used to study the retention of local crystallinity within the LLBZT structure. No observable kinks, dislocations or atom vacancies were observed form the high-resolution TEM (HR-TEM) images before or after solution treatment of H_2O in the areas imaged. Due to beam sensitivity, HR-TEM images were unsuccessfully collected for D_2O and 1 M LiOH samples. Similar findings were observed for $Li_7La_3Zr_2O_{12}$ by Ma *et al.*[50] before and after treated with 2 M LiOH as well as Buschmann *et al.*[49] before and after LLZO was treated with H_2O.

The XRD (Figure 4.9) shows that samples before and after treatment display cubic $Ia\bar{3}d$ space group. As with HR-TEM images, selected area electron diffraction (SAED) patterns were collected for as-prepared and H_2O treated samples were oriented along the [111] zone axis, seen in Figure 4.11. Simulated patterns were generated using STEM Cell software.[84] Simulation patterns were based off cubic garnet $Ia\bar{3}d$ with similar doping previously reported.[51] Although not all diffraction spots are seen in the experimental results with respect to simulated, many distinguishable spots can be indexed, revealing that the $Ia\bar{3}d$ cubic lithium-garnet crystal structure is retained after treatment with H_2O. Although some spots appear to be 'missing' in the experimental pattern compared to the simulated pattern, this can be attributed to the sample being slightly off the [111] zone axis, reducing the intensity of various spots.

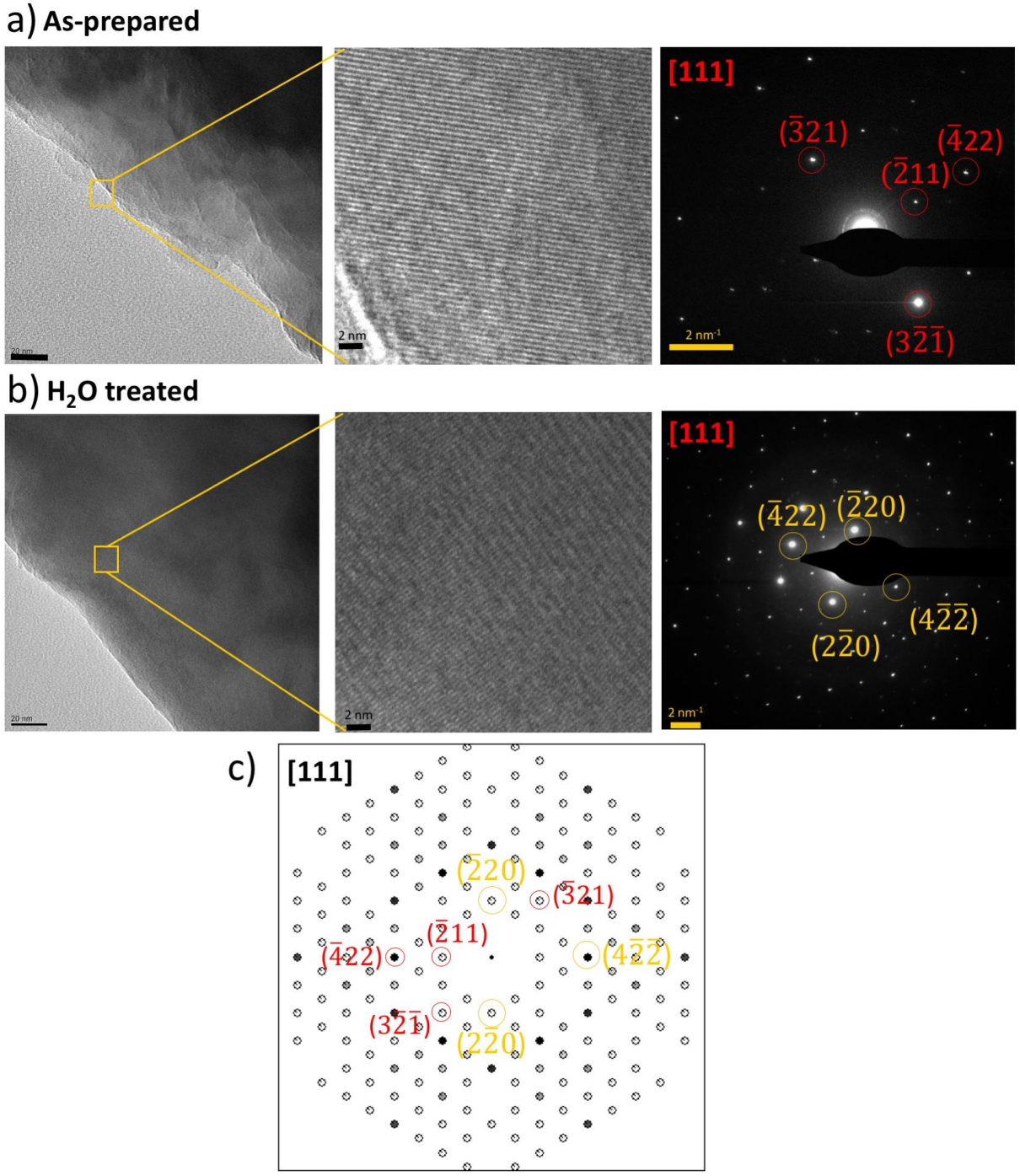

Figure 4.11 HR-TEM images and SAED patterns of $Li_{6.5}La_{2.5}Ba_{0.5}ZrTaO_{12}$ of a) As-prepared sample and b) after soaking in H_2O for 168 h. c) Simulated electron diffraction of $Ia\bar{3}d$ cubic lithium garnet crystal structure along the [111] zone axis.

4.2.2.3 Ion-exchange extent in protonated $Li_{6.5}La_{2.5}Ba_{0.5}ZrTaO_{12}$ in powder form

The ion-exchange of the powder form $Li_{6.5}La_{2.5}Ba_{0.5}ZrTaO_{12}$ was determined in the same manner to the bulk pellets discussed in section 4.2.1.3. Similarly, weight losses associated with water and carbonate species, seen in Figure 4.12 are observed. Table 4.1 highlights the weight loss attributed to water (30-550 ^{o}C). Comparing ion-exchange between bulk pellets and powders, it is evident that the higher surface area to volume ratio plays a vital role in the extent of exchange.

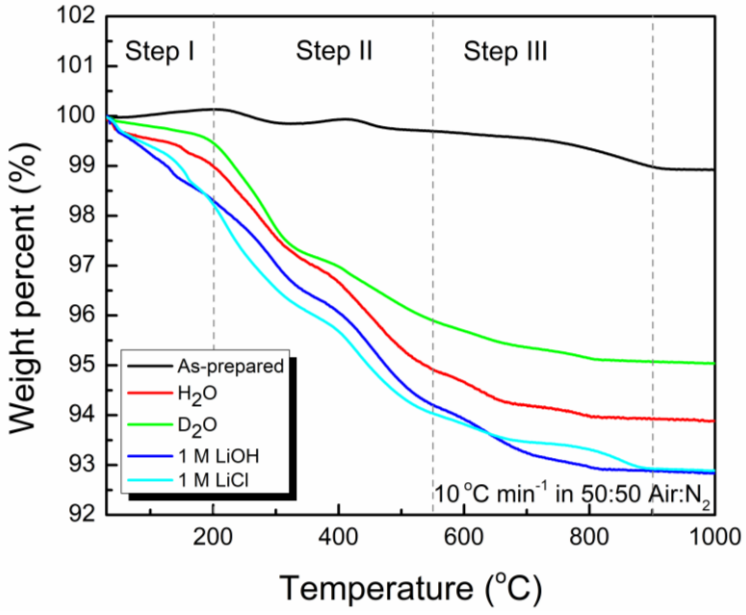

Figure 4.12 Thermogravimetric analysis of $Li_{6.5}La_{2.5}Ba_{0.5}ZrTaO_{12}$ sample after soaking in respective solutions for 168 h, samples heated at 10 °C min^{-1} under 50/50 N_2/Air.

Table 4.1 Summary of proton-exchange after $Li_{6.5}La_{2.5}Ba_{0.5}ZrTaO_{12}$ is soaked in aqueous solution, based on TGA results in Figure 4.12.

Solution Treatment	Weight loss % (30-550 ^{o}C)	Li^+/H^+ exchange (%)
As-prepared	0.3	4.6
H_2O	5.1	78
D_2O	4.1	57
1 M LiOH	5.8	88.3
1 M LiCl	5.9	90.7

4.3 Summary

To summarize, $Li_{6.5}La_{2.5}Ba_{0.5}ZrTaO_{12}$ has shown to undergo the spontaneous Li^+/H^+ reaction after treatment with deionized H_2O, D_2O, 1 M LiOH, or 1 M LiCl based on TGA results. Although lithium is replaced by protons, the cubic garnet crystal structure is retained, evident from XRD and ED diffraction patterns. This combined indicates that the spontaneous Li^+/H^+ reaction is of topotactic nature. Despite the lithium-garnet becoming protonated, the ionic conductivity calculated from EIS has shown to slightly increase over the course of 24 hours and stabilizes thereafter, this was seen for the 10-day duration monitoring. SEM images reveal that water and D_2O treated samples resemble that of pristine samples, whereas 1 M LiOH and 1 M LiCl samples show distinct morphological changes. With a clearer understanding of the aqueous stability of $Li_{6.5}La_{2.5}Ba_{0.5}ZrTaO_{12}$, further understanding of $Li_{6.5}La_{2.5}Ba_{0.5}ZrTaO_{12}$ with Li for application towards a Li-O_2 cell are reported in the following chapter.

Chapter Five: **Electrochemical stability of lithium garnets $Li_{6.5}La_{2.5}Ba_{0.5}ZrTaO_{12}$ and $Li_7La_{2.75}Ca_{0.25}Zr_{1.75}Nb_{0.25}O_{12}$**

Contents of this chapter are reproduced from the published work, "Characterization of lithium-rich garnet-type $Li_{6.5}La_{2.5}Ba_{0.5}ZrTaO_{12}$ for beyond intercalation chemistry-based lithium-ion batteries" by Kyle Hofstetter, Alfred Junio Samson, and Venkataraman Thangadurai, *Solid State Ionics*. 2018, 318, 71-81, "Towards Mixed Ionic and Electronic Conducting Li-Stuffed Garnets" by Alfred Junio Samson, Kyle Hofstetter, Eric Wachsman, and Venkataraman Thangadurai, J. Electrochem Soc. 2018, 165, A2303-A2311, and to be submitted "Impedance analysis of garnet-type $Li_7La_{2.75}Ca_{0.25}Zr_{1.75}Nb_{0.25}O_{12}$ with and without ALD-Al_2O_3 under CO_2 and humidity" by Kyle Hofstetter, Alfred Junio Samson, Jiaqi Dai, Evan Gritton, Liangbing Hu, Eric Wachsman, and Venkataraman Thangadurai Lithium-garnet studies with $Li_7La_{2.75}Ca_{0.25}Zr_{1.75}Nb_{0.25}O_{12}$ were done in collaboration with the Eric Wachsman group (University of Maryland Energy Research Center).

5.1 General overview

Next generation batteries are believed to utilize metallic lithium anode (3861 mAh g^{-1}) opposed to lithiated graphite (372 mAh g^{-1}) found in current state-of-the-art batteries. Due to the highly reducing nature of lithium, very few lithium ion conducting electrolytes are known to be stable with metallic lithium. Lithium-garnets are among the few electrolytes that are reported to be stable with Li. In addition to Li anodes, next generation battery chemistry will rely on conversion reactions rather than intercalation reactions. One such battery chemistry proposed is aqueous Li-O_2, where Li is coated in a protective layer that is submerged into an aqueous electrolyte along with a porous carbon cathode. In order for this architecture to be achieved, a protective solid-state Li-ion electrolyte layer stable to both Li and an aqueous media must be investigated. The following

work has been carried out to study the electrochemical stability of $Li_{6.5}La_{2.5}Ba_{0.5}ZrTaO_{12}$ (LLBZT) by Li by plating-stripping experiments. The feasibility of LLBZT as a lithium anode protective layer was investigated by monitoring the open-circuit voltage (OCV) of a Li | garnet | aqueous media cell. Additional electrochemical stability measurements were carried out with a similar garnet composition, $Li_7La_{2.75}Ca_{0.25}Zr_{1.75}Nb_{0.25}O_{12}$ (LLCZN). Electrochemical stability was determined using cyclic voltammetry (CV) and DC polarization (Hebb-Wagner) methods to further confirm that lithium-garnet materials are electrochemical stabile with metallic lithium and potential candidates for next generation lithium batteries.

5.2 Results and discussion

5.2.1 Lithium plating and stripping across $Li_{6.5}La_{2.5}Ba_{0.5}ZrTaO_{12}$ and area specific resistance

5.2.1.1 Plating and stripping lithium across $Li_{6.5}La_{2.5}Ba_{0.5}ZrTaO_{12}$

Lithium garnet powders of $Li_{6.5}La_{2.5}Ba_{0.5}ZrTaO_{12}$ (LLBZT) were sintered in a crucible geometry, allowing lithium to be melted onto both sides, forming a lithium symmetric cell. Figure 5.1 shows a schematic representation of the symmetric crucible cell. Figure 5.2 shows the lithium plating and stripping hysteresis, the current was applied in each direction for 1 minute at 39 84, and 169 μA cm^2, similar voltage profiles have also been reported by Luo et al.[66] The over-potential in each step is associated with the total resistance of the cell. The total resistance is a combination of the resistance of Li-ion migration in the electrolyte + the interfacial resistance to plate/strip lithium to/from the metallic lithium electrode. At lower current densities, lower over-potentials are observed, hence a lower overall resistance.

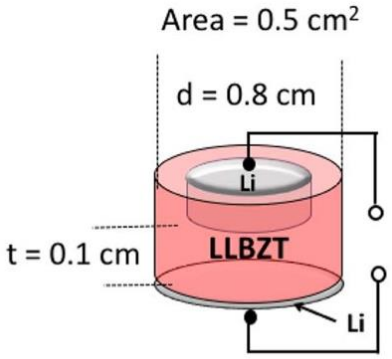

Figure 5.1 Schematic of $Li_{6.5}La_{2.5}Ba_{0.5}ZrTaO_{12}$ symmetric lithium circle cell. Reprinted (adapted) with permission from Hofstetter, K.; Samson, A.J.; Thangadurai, V. *Solid State Ionics* 2018, 318, 71-81. Copyright (2018), with permission from Elsevier [OR APPLICABLE SOCIETY COPYRIGHT OWNER].

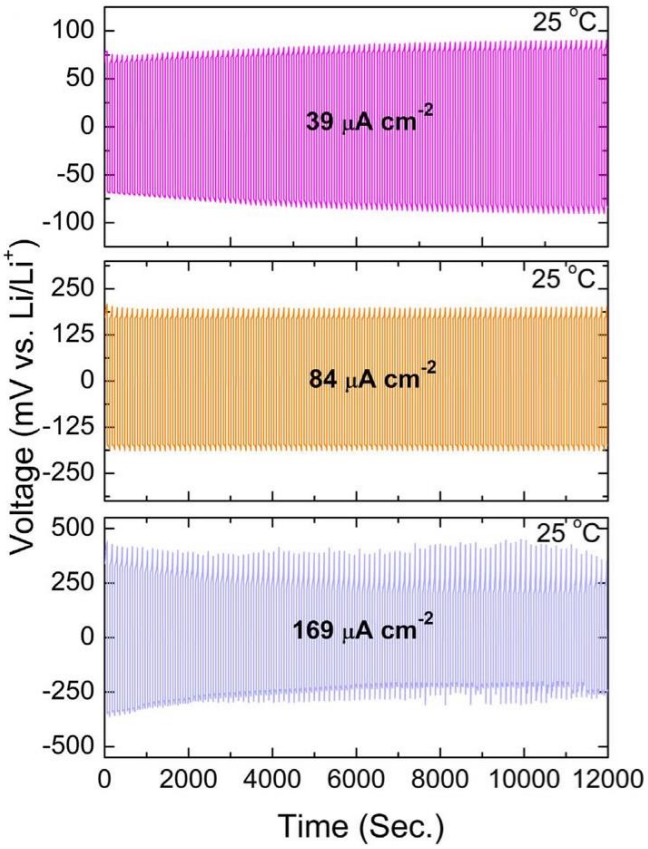

Figure 5.2. Lithium plating-stripping voltage hysteresis of the symmetric crucible cell shown in Figure 5.1. Reprinted (adapted) with permission from Hofstetter, K.; Samson, A.J.; Thangadurai, V. *Solid State Ionics* 2018, 318, 71-81. Copyright (2018), with permission from Elsevier [OR APPLICABLE SOCIETY COPYRIGHT OWNER].

5.2.1.2 Area specific resistance of lithium | $Li_{6.5}La_{2.5}Ba_{0.5}ZrTaO_{12}$ interface

The area specific (interfacial) resistance (ASR) value for the charge transfer resistance between the solid metallic lithium and solid garnet electrolyte can be estimated from the initial over-potential of the plating-stripping experiment (Figure 5.2). Using Ohm's law, a linear fit of the over-potential vs. applied current indicates that the total resistance of the cell is 3200 Ω. The total solid Li-ion electrolyte resistance determined from EIS indicates that the bulk ionic resistance is 1308 Ω at 25 °C. Figure 5.3 highlights the Arrhenius behavior of LLBZT in the temperature range of 25-150 °C. Therefore, the ASR of the Li | garnet interface at 25 °C can be determined as followed:

$$\left[\frac{(3200\,\Omega - 1308\,\Omega)}{2}\right] * 0.5\,cm^2 = 473\,\Omega\,cm^2 \qquad (5.1)$$

The factor of 2 accounts for the symmetric cell configuration, therefore, an interfacial resistance of 473 Ω cm^2 was determined based on DC plating and stripping methods. Another approach to determine the interfacial resistance is to use EIS with non-blocking electrodes. Figure 5.4 shows a typical Nyquist plot of LLBZT sandwiched between metallic lithium electrodes before the plating-stripping experiment. The first semi-circle is associated with the resistance of the bulk electrolyte, where the second semi-circle is associated with the interfacial resistance of both Li | garnet interfaces. The total resistance (electrolyte + interface) from the EIS measurement was found to be 3500 Ω, comparable to the 3200 Ω found in the plating-stripping experiment. Subtracting the 1308 Ω form the bulk electrolyte and dividing by 2, the interfacial resistance is determined to be 548 Ω cm^2, again comparable to the value determined using the plating-stripping experiment. Although high, these ASR values are comparable to other untreated samples in the literature,[5] other studies have investigated surface modifications in order to reduce the ASR value,[5] with the lowest

ASR value reaching 1 Ω cm^2 by applying a thin 10 nm Al_2O_3 interfacial layer between the lithium and garnet surface.[35]

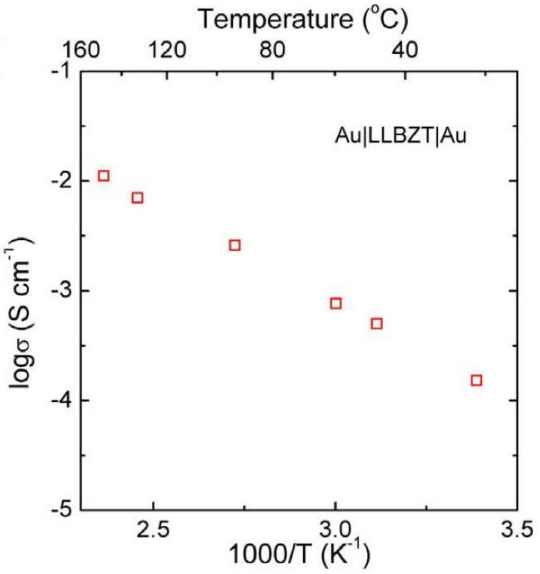

Figure 5.3. Arrhenius plot of LLBZT under ambient air. Reprinted (adapted) with permission from Hofstetter, K.; Samson, A.J.; Thangadurai, V. *Solid State Ionics* 2018, 318, 71-81. Copyright (2018), with permission from Elsevier [OR APPLICABLE SOCIETY COPYRIGHT OWNER].

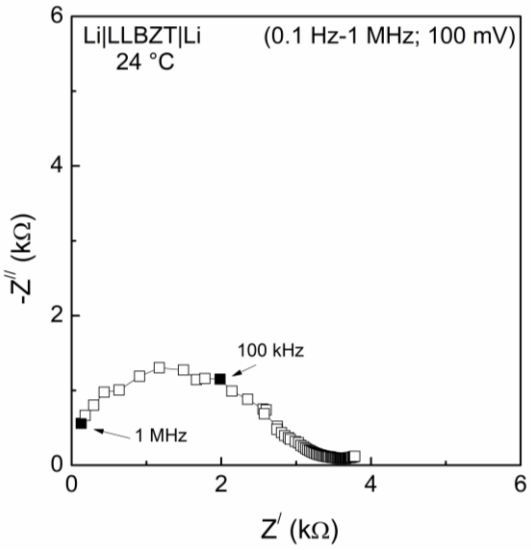

Figure 5.4. Open circuit Nyquist plot of Li|LLBZT|Li symmetric cell. Reprinted (adapted) with permission from Hofstetter, K.; Samson, A.J.; Thangadurai, V. *Solid State Ionics* 2018, 318, 71-81. Copyright (2018), with permission from Elsevier [OR APPLICABLE SOCIETY COPYRIGHT OWNER].

5.2.2 $Li_{6.5}La_{2.5}Ba_{0.5}ZrTaO_{12}$ as a protective layer in aqueous Li-O_2 cells.

In combination with earlier findings regarding the stability of lithium garnet LLBZT with aqueous solution (Chapter 4), aqueous Li-O_2 cells were constructed to further investigate the lithium and aqueous stability of LLBZT. Figure 5.5 shows the Li | LLBZT | aqueous solution cell configuration, LLBZT were again sintered in a crucible geometry, allowing lithium to be melted within and protected from the aqueous environment. Carbon paper was used as the air cathode.

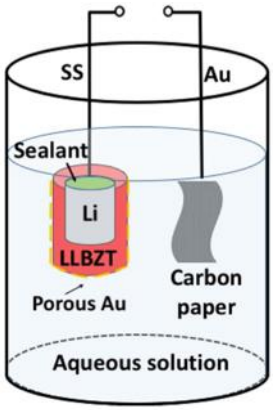

Figure 5.5 Schematic representation of lithium | LLBZT | aqueous. Reprinted (adapted) with permission from Hofstetter, K.; Samson, A.J.; Thangadurai, V. *Solid State Ionics* 2018, 318, 71-81. Copyright (2018), with permission from Elsevier [OR APPLICABLE SOCIETY COPYRIGHT OWNER].

Figure 5.6 shows the open circuit voltage (OCV) of the cells comprised of 0.1 M LiOH, 1 M LiOH, and 1 M LiCl. In all three cases, a stable voltage of ~3 V is observed. The lack of short-circuit (0 V) indicates that the LLBZT is free of micropores that would allow the aqueous solution to penetrate and react with the Li anode. In order to confirm the reproducibility of the OCV, the cells were intentionally short-circuited to remove any potential stray capacitance, in all solutions after each short-circuit the OCV would resume at ~3 V, as seen in Figure 5.7. Based on the literature,[85] we believe the following two-electron half-cell chemical reactions and net reaction to describe the observed voltage:

Anode side reaction: $2Li \rightarrow 2Li^{+} + 2e^{-}$ (5.1)

Cathode side reaction: $O_2 + H_2O + 2e^{-} \rightarrow OH^{-} + HO_2^{-}$ (5.2)

Overall reaction: $2Li + O_2 + H_2O \rightarrow LiOH + Li^{+} + HO_2^{-}$ (5.3)

Which will subsequently react as follows:[86]

$2Li^{+} + HO_2^{-} + OH^{-} \rightarrow Li_2O_2 \downarrow + H_2O$ (5.4)

Depending upon pH and catalytic activity on the cathode, the oxygen reduction reaction (ORR) appears to follow two-electron and/or four-electron paths in alkaline solution, leading to different reaction products and potentials. The four-electron path is as follows:[46, 85, 86]

Anode side reaction: $4Li \rightarrow 4Li^{+} + 4e^{-}$ (5.5)

Cathode side reaction: $O_2 + 2H_2O + 4e^{-} \rightarrow 4OH^{-}$ (5.6)

Overall reaction: $4Li + O_2 + 2H_2O \rightarrow 4LiOH$ (5.7)

The two-electron process described in reaction (5.3) has an OCV of ~3 V vs. Li, whereas the four-electron process in reaction (5.7) has an OCV of ~3.45 V vs. Li. We believe in our cells the two-electron path is seen in all three aqueous solutions. With a lack of oxygen reduction reaction (ORR) catalyst on the air cathode and a low concentration of dissolved oxygen forces the reaction in the two-electron process. This argument is also suggested by Safanama and Adams.[85]

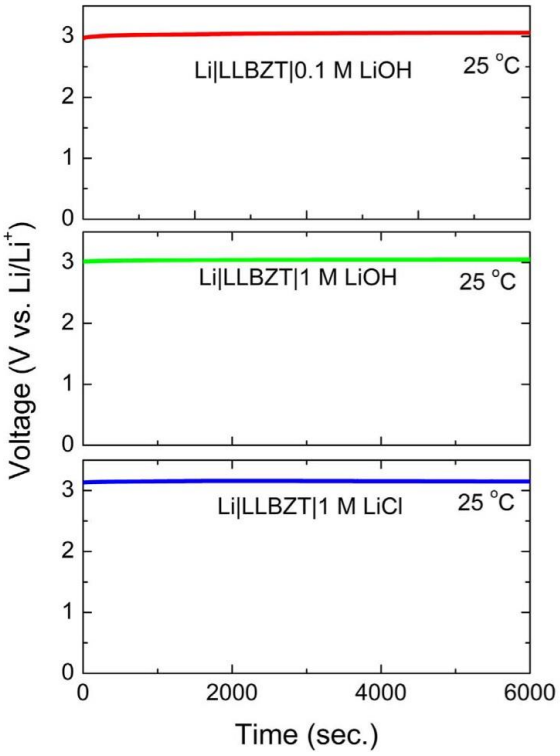

Figure 5.6 Open circuit voltage of lithium|LLBZT|0.1 M LiOH, lithium|LLBZT|1 M LiOH, and lithium|LLBZT|1 M LiCl cells as a function of time. Reprinted (adapted) with permission from Hofstetter, K.; Samson, A.J.; Thangadurai, V. *Solid State Ionics* 2018, 318, 71-81. Copyright (2018), with permission from Elsevier [OR APPLICABLE SOCIETY COPYRIGHT OWNER].

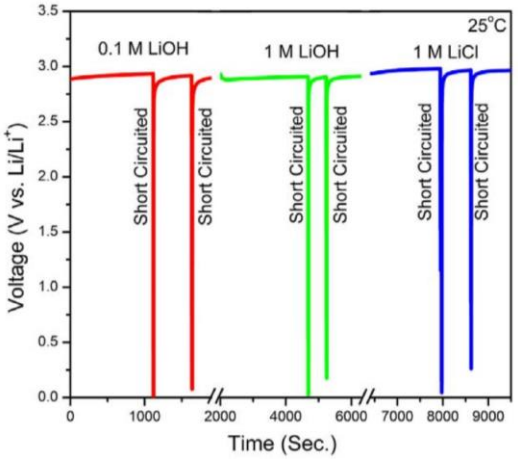

Figure 5.7 Open circuit voltage after intentional short circuit of cells in Figure 5.5. Reprinted (adapted) with permission from Hofstetter, K.; Samson, A.J.; Thangadurai, V. *Solid State Ionics* 2018, 318, 71-81. Copyright (2018), with permission from Elsevier [OR APPLICABLE SOCIETY COPYRIGHT OWNER].

5.2.3 Ionic and Electronic conductivity of $Li_7La_{2.75}Ca_{0.25}Zr_{1.75}Nb_{0.25}O_{12}$

5.2.3.1 Ionic conductivity of LLCZN

The Li-ion conductivity of $Li_7La_{2.75}Ca_{0.25}Zr_{1.75}Nb_{0.25}O_{12}$ (LLCZN) was determined using electrochemical impedance spectroscopy. LLCZN pellets were coated with Li-ion blocking Au electrodes and EIS was measurement under open circuit conditions in the frequency range of 0.1 Hz – 1 MHz with a perturbation potential of 100 mV. Figure 5.8 highlights a typical impedance spectra of LLCZN at 25 ^oC, under ambient air. The data is fit with the $R_b(R_{gb}CPE_{gb})CPE_e$ equivalent circuit, corresponding to the bulk resistance (3571 Ω cm), resistance and constant phase element of the grain boundary, and the constant phase element of the electrode interface, respectively. The ionic conductivity was determined using equation (3.5). The ionic conductivity of LLCZN at 25 ^oC was determined to be 2.8 x 10^{-4} S cm^{-1}, which is comparable with many of lithium-garnets ionic conductivities.[18, 35] Figure 5.8 shows the Arrhenius plot of LLCZN in the temperature range of 23-150 ^oC, the activation energy over this temperature range was determined to be 0.33 eV based on the Arrhenius equation (3.6).

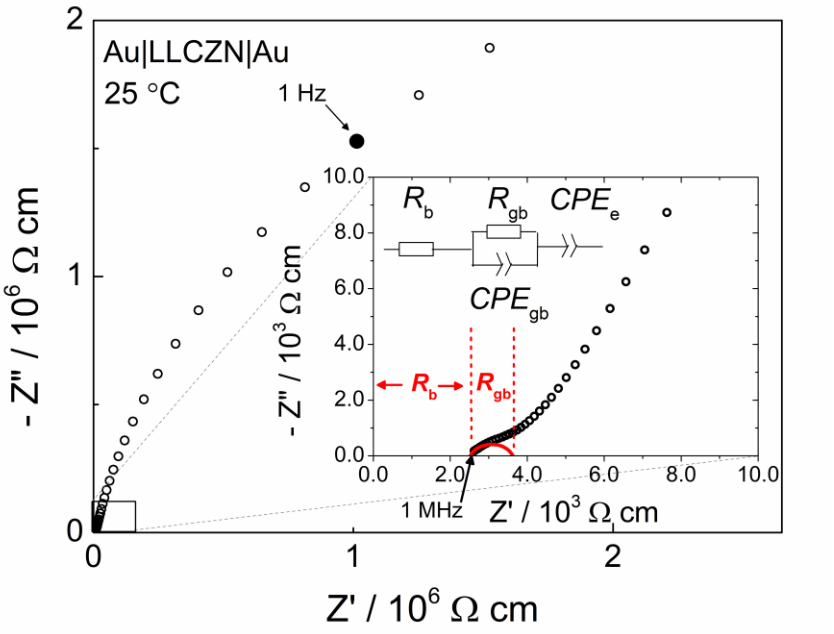

Figure 5.8 Impedance spectra of LLCZN at 25 ºC. The inset shows the data at high frequencies and the equivalent circuit model used to obtain the different resistance contributions. The simulated medium semicircle is shown in red solid line. Reproduced (adapted) with permission from *J. Electrochem. Soc.*, 165, A2303 (2018). Copyright 2018, The Electrochemical Society.

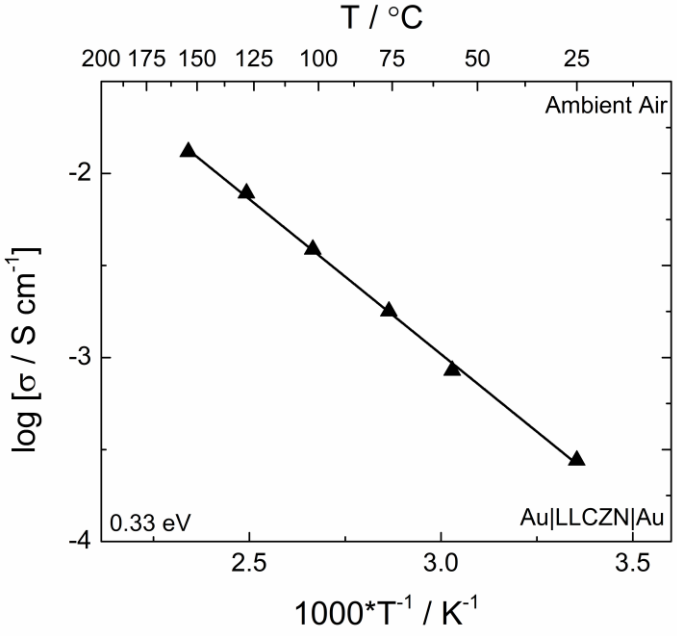

Figure 5.9 Arrhenius plots of total conductivity of LLCZN Reproduced (adapted) with permission from *J. Electrochem. Soc.*, 165, A2303 (2018). Copyright 2018, The Electrochemical Society.

5.2.3.2 Electronic conductivity of LLCZN

In order to determine the electronic conductivity of LLCZN, Hebb-Wagner (HW) measurements was performed. LLCZN pellets were sputtered with Au on one side and Li was thermally attached to the opposing side (heating to 180 ºC/ 1 h), in an argon-filled glovebox. Figure 5.10 shows the time-dependent current response upon applying a potential bias between 0.5-6 V at 25 ºC. The initial high current at each potential is attributed to the Li-ion mobility, while the semi-stabilized current (t = 4 h) is from electronic conductivity, as current due to Li-ion migration is blocked.[71] The steady state current as a function of voltage is shown in Figure 5.11. Using Ohm's law, V = IR, the electronic conductivity was determined to be in the range of ~10^{-8} S cm^{-1}, four orders of magnitude lower than the total ionic conductivity determined through EIS (Figure 5.8). The transference number (t_i) was determined to near unity, using the following equation:

$$t_{Li} = \frac{\sigma_{Li}}{\sigma_{Li} + \sigma_e} \tag{3.7}$$

$$t_{Li} = \frac{10^{-4}\,S\,cm^{-2}}{\left(10^{-4}\,S\,cm^{-2} + 10^{-8}\,S\,cm^{-2}\right)} \approx 0.99$$

Given that that transference number is near unity, suggesting that lithium-garnet LLCZN is predominantly an ionically conductor. The transference number near 1 agrees with many other reported garnet compositions in the literature. [18, 72, 87]

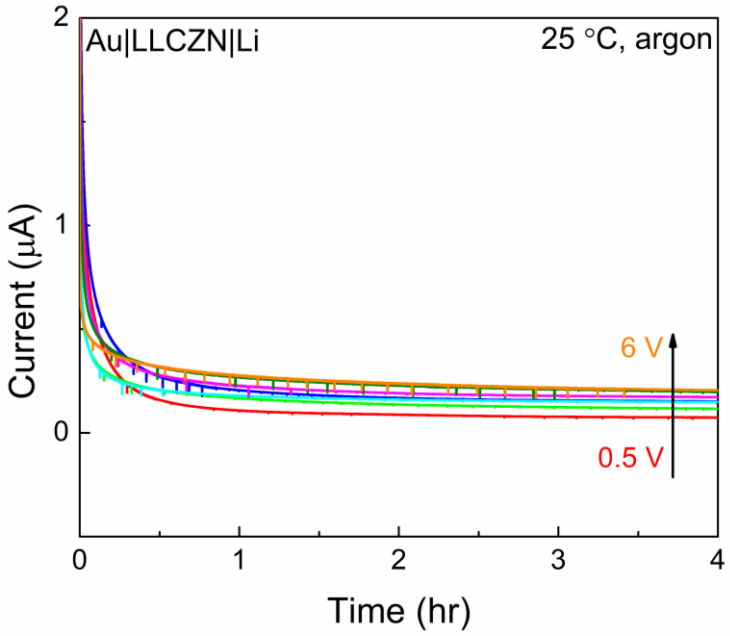

Figure 5.10 Time dependences of the current upon application of voltages 0.5–6 V vs. Li at 25 ºC under argon.

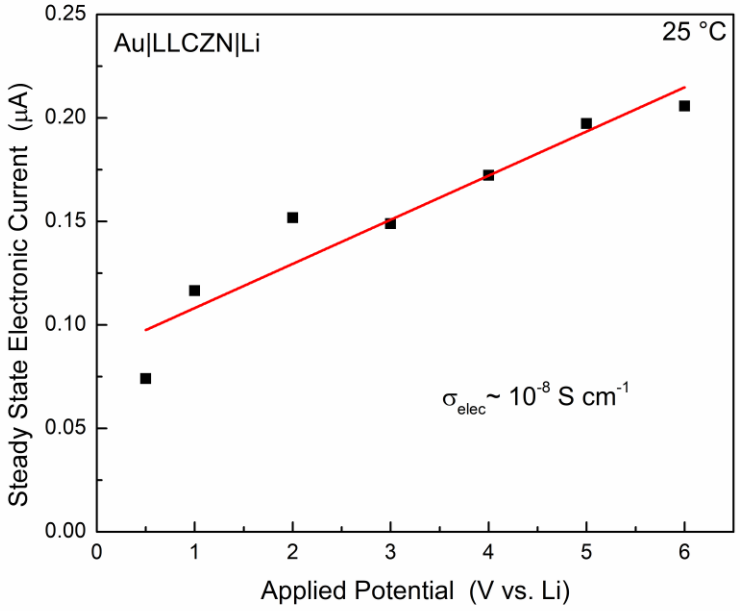

Figure 5.11 Applied bias (V) vs. steady state electronic current (I) curve to calculate the electronic resistance using Ohm's law.

5.2.3.3 Electrochemical Stability Windows of $Li_7La_{2.75}Ca_{0.25}Zr_{1.75}Nb_{0.25}O_{12}$

To determine the electrochemical stability window (ESW) of the lithium-garnet $Li_7La_{2.75}Ca_{0.25}Zr_{1.75}Nb_{0.25}O_{12}$, cyclic voltammetry (CV) measurements were performed. Pellet form of samples were sputtered with Au (~ 40 nm in thickness) on one side and transferred to an argon glove box. Li was heated onto the bare side of the pellet at 200 ^oC for 1 h and naturally cooled. Here, Au acts as the working electrode (WE), whereas Li plays the role of the counter (CE) and reference electrodes (RE). Figure 5.12 display the CV profile of LLCZN. Scans were measured between -0.5 and 6 V vs. Li/Li^+ with a sweep rate of 1 mV s^{-1}. The only observable peaks are centred around 0 V vs. Li/Li^+, the reduction peak is due to Li being deposited onto the Au working electrode ($Li^+ + e^- \rightarrow Li$), whereas the oxidation peak corresponds to the Li dissolution from the Au electrode and entering the garnet structure. As there are no other peaks due to redox reaction seen throughout the scanned window, $Li_7La_{2.75}Ca_{0.25}Zr_{1.75}Nb_{0.25}O_{12}$ is electrochemically stable up to 6 V vs. Li/Li^+. These findings are consistent with other stable Li-ion conductive electrolytes.[35, 36, 58]

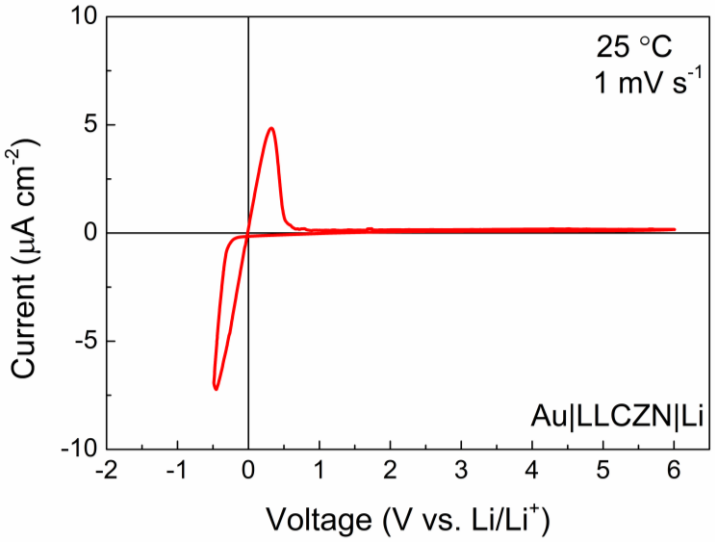

Figure 5.12 Cyclic voltammetry profile of LLCZN under argon at 25 ºC. Au was used as the working electrode, whereas lithium was the counter and reference.

5.3 Summary

Having demonstrated the aqueous stability of LLBZT in aqueous media (Chapter 4), this lithium-garnet was able to be applied as a protective layer in an aqueous Li-O_2 cell. Using carbon as an air electrode, a steady ~3 V was observed for the Li | LLBZT | aqueous media cell, further suggesting that the lithium-garnet can be used in next generation aqueous Li-O_2 batteries. LLCZN is shown to be primarily a Li-ion conductor with a transference value near unity (~1) based on DC Hebb-Wagner and electrochemical impedance measurements. Furthermore, the electrochemical stability window is shown to be up to 6 V vs. Li/Li^+ using cyclic voltammetry. Having demonstrated that LLCZN is electrochemically stable with Li, further investigations regarding the stability LLCZN in the presence of humidity and CO_2 are explored in Chapter 6.

Chapter Six: **Gaseous stability of lithium-garnet $Li_7La_{2.75}Ca_{0.25}Zr_{1.75}Nb_{0.25}O_{12}$**

This chapter reports the work in collaboration with the Eric Wachsman group at the University of Maryland. Contents of this chapter are to be submitted "Impedance analysis of garnet-type $Li_7La_{2.75}Ca_{0.25}Zr_{1.75}Nb_{0.25}O_{12}$ with and without ALD-Al_2O_3 under CO_2 and humidity" by Kyle Hofstetter, Alfred Junio Samson, Jiaqi Dai, Evan Gritton, Liangbing Hu, Eric Wachsman, and Venkataraman Thangadurai.

6.1 General overview

This chapter investigates the stability of lithium-garnet, $Li_7La_{2.75}Ca_{0.25}Zr_{1.75}Nb_{0.25}O_{12}$ (LLCZN) in the presence of CO_2 and humidity. Lithium-garnets are known to react with both humidity and CO_2 but little is known how this affects the ionic stability. Humidity is believed to react with lithium-garnets the same way as aqueous solution: [5, 46, 52]

$$Li_7La_3Zr_2O_{12} + xH_2O \rightarrow Li_{7-x}H_xLa_3Zr_2O_{12} + xLiOH \tag{6.1}$$

forming LiOH on the grain boundaries which subsequently reacts with CO_2 forming a Li_2CO_3 layer on the surface of lithium-garnets:[5, 46, 52]

$$LiOH + \frac{1}{2}CO_2 \rightarrow \frac{1}{2}Li_2CO_3 + \frac{1}{2}H_2O \tag{6.2}$$

Also, a direct carbonation mechanism has been reported: [5, 52]

$$Li_7La_3Zr_2O_{12} + xCO_2 \rightarrow Li_{7-x}La_3Zr_2O_{12-x} + xLi_2CO_3 \tag{6.3}$$

this Li_2CO_3 layer has been shown to increase the interfacial resistance between the lithium-garnet and the metallic Li electrode.[52, 88] Various groups have sought out to reduce the interfacial resistance by applying additional interfacial layers.[35, 65-67, 89-92] The most successful approach reported to reducing the lithium|garnet interfacial resistance is performed by applying a thin Al_2O_3

layer. As such, uncoated $Li_7La_{2.75}Ca_{0.25}Zr_{1.75}Nb_{0.25}O_{12}$ samples show a Li | garnet interfacial resistance of 1710 Ω cm^2, whereas Al_2O_3 coated samples drop to 1 Ω cm^2 [ref.[35]]. Although this coating has shown to negate the interfacial resistance, there is a lack of understanding towards its potential as a protective layer from moisture and CO_2 reactions. In this chapter, we have aimed to decouple the humidity and CO_2 reactions to monitor the effects on ionic conductivity and overall stability of $Li_7La_{2.75}Ca_{0.25}Zr_{1.75}Nb_{0.25}O_{12}$ with and without the Al_2O_3 coating. Figure 6.1 shows the schematic representation of the in-situ impedance setup.

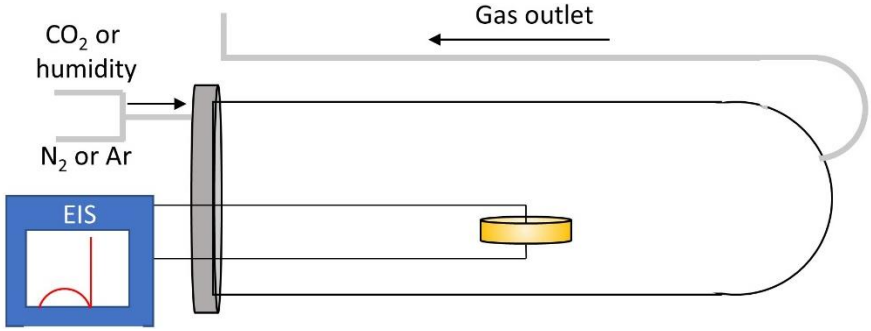

Figure 6.1 Schematic representation of in-situ impedance setup.

6.2 Results and discussion

$Li_7La_{2.75}Ca_{0.25}Zr_{1.75}Nb_{0.25}O_{12}$ (LLCZN) samples without any coating were synthesized via solid-state method at the University of Calgary, described in Chapter 3. Samples with the Al_2O_3 coating were synthesized by the Wachsman group (University of Maryland Energy Research Center). Garnet samples from the Wachsman group were synthesized via sol-gel preparation, a 10 nm Al_2O_3 layer was applied using atomic layer deposition (ALD). For this thesis, samples with the coating will be referred to as ALD-LLCZN, whereas uncoated will be LLCZN. Upon receiving, samples were stored in an Ar-filled glovebox to reduce any potential reaction with moisture or CO_2. Crystal

structures of both coated and uncoated samples was characterized by XRD, as shown in Figure 6.2. Both samples have $Ia\bar{3}d$ cubic garnet phase and are isostructural with parent phase $Li_5La_3Nb_2O_{12}$ (PDF No.: 45-0109). Peaks associated to Al_2O_3 are not observed, as these are below the 5% limit of detections of XRD.

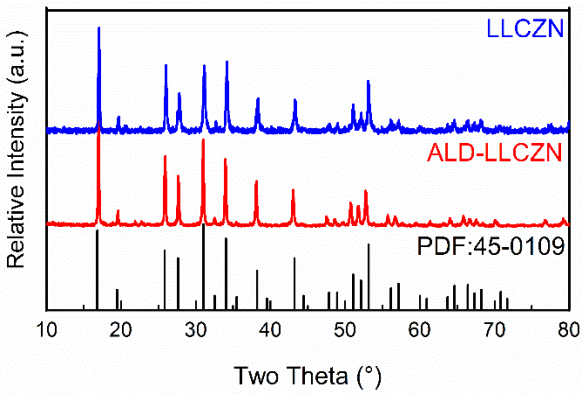

Figure 6.2 XRD diffraction patterns of inhouse made $Li_7La_{2.75}Ca_{0.25}Zr_{1.75}Nb_{0.25}O_{12}$ and as-received $Li_7La_{2.75}Ca_{0.25}Zr_{1.75}Nb_{0.25}O_{12}$ with Al_2O_3 coating, parent $Li_5La_3Nb_2O_{12}$ (PDF No.: 45-0109) shown for reference.

To monitor ionic conductivity in various atmospheres, pellets were sputtered with Au (~40 nm) on opposing sides to act as current collectors. Sputtering was used rather than Au paste to remove the need of thermal curing; aluminum is reported to diffuse into the garnet structure at elevated temperatures,[93, 94] therefore Au curing could not be performed with Al_2O_3 coated samples.

Although samples were prepared via two different methods (solid-state and sol-gel), the conductivity of both samples are comparable. Figure 6.3a shows the Arrhenius plots of LLCZN with and without the Al_2O_3 coating in the temperature range of room temperature to 225 ^oC. These values are consistent with similar lithium-garnet compositions reported in the literature.[18] Figures 6.3b and c show the microstructure of LLZCN synthesized via solid-state and sol-gel methods, both samples have comparable microstructures with grain diameter in the range of 5-10 μm.

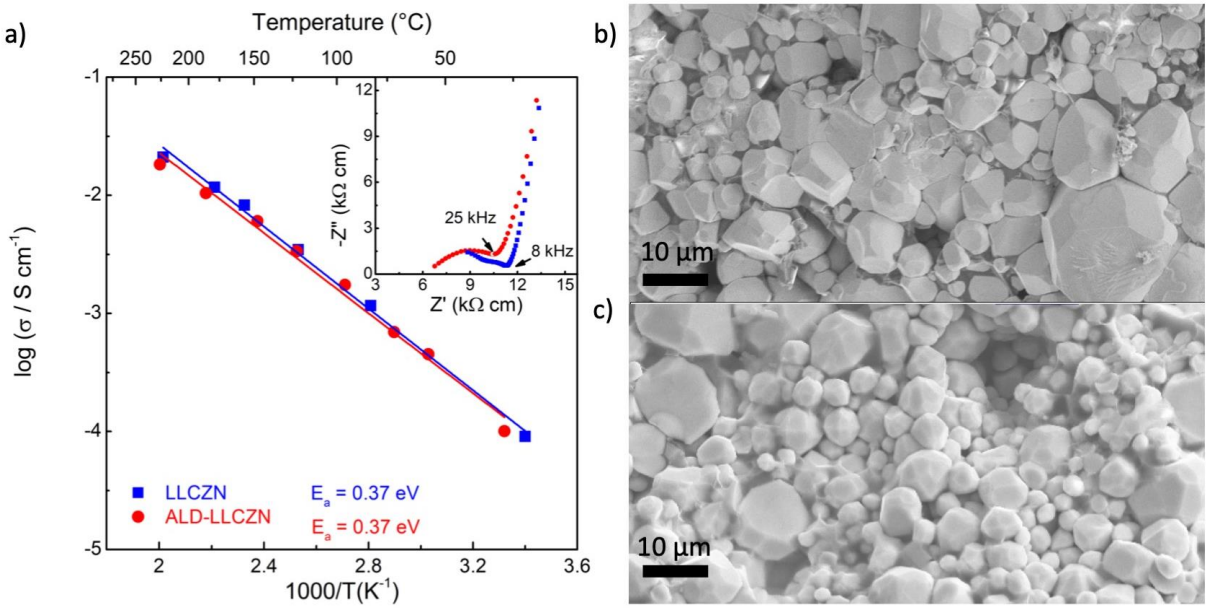

Figure 6.3 (a) Arrhenius plot of LLCZN without coating (blue square) synthesized via solid-state method at the University of Calgary. LLCZN with ALD coating (red circle) synthesized via sol-gel method at University of Maryland. Both samples have an activation energy of ~0.37 eV and conductivities of about 1 x 10^{-4} S cm at room temperature. Inset shows typical Nyquist plot of ALD-LLCZN (red circle at 28 ºC) and LLCZN (blue 21 ºC). (b) and (c) Scanning electron microscopy images of fracture cross-section of LLCZN pellet synthesized via solid-state and sol-gel methods, respectively.

6.2.1 Ionic stability of $Li_7La_{2.75}Ca_{0.25}Zr_{1.75}Nb_{0.25}O_{12}$ under CO_2

To determine the maximum concentration of CO_2 that lithium-garnets can be exposed to before altering the ionic conductivity, samples were exposed to various concentrations (0 ppm to pure) of CO_2 and in-situ impedance measurements were collected every 4-24 h for a total 100 h at each concentrations. Samples were initially measured under inert N_2 for 100 h to build a baseline, the starting concentration of CO_2 was set to 400 ppm as this is close to that found in ambient conditions (at the time of writing). Figures. 6.4a and b show the Nyquist plots under dry N_2, 400 ppm CO_2/N_2 (100 h) and 3000 ppm CO_2/N_2 (100 h) at 25 °C for the uncoated and ALD-coated samples,

respectively. It is worth noting that little to no change is observed for both the Al_2O_3 coated samples, however a small increase in resistance is observed for samples without the Al_2O_3 coating.

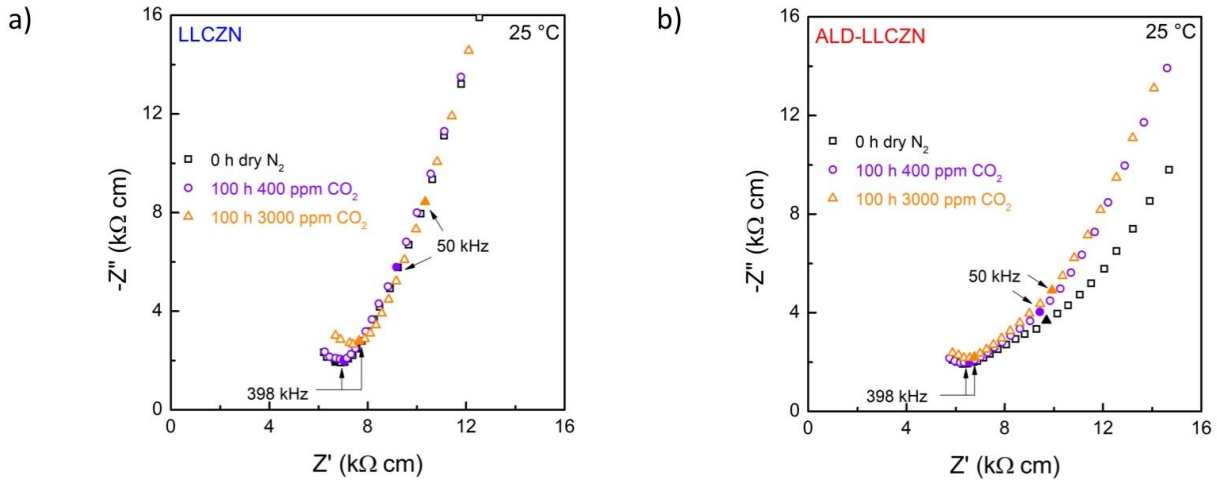

Figure 6.4 Impedance spectra of $Li_7La_{2.75}Ca_{0.25}Zr_{1.75}Nb_{0.25}O_{12}$ under 400 ppm CO_2/N_2 for 100 h for a) uncoated and b) Al_2O_3 coated.

Rather than going directly from 400 ppm CO_2/N_2 to 3000 ppm CO_2, a variety of CO_2 concentrations were analyzed. Figure 6.5a and b shows the normalized total resistance for each measurement for both the uncoated and coated samples, respectively. The total resistance value was obtained from the real part of the impedance just before the low-frequency spike. This value was then normalized by multiplying by a/l, where a is the area and l is the thickness of the electrodes. Upon reaching approximately 1000 h and 3000 ppm CO_2/N_2 it is noted that the total resistance of the uncoated sample has increased 8.2% when compared to the first resistance value collected under dry N_2. However, samples with the Al_2O_3 coating only show a 1.4% increase over the same time and CO_2 concentrations range. To provide further credibility to the results, another sample of each of the ALD-coated and uncoated Li-garnets were exposed to accelerated CO_2 increase test as shown in Figure 6.5c and d. After exposure to pure CO_2, the increase in resistance

compared to dry N_2 for the uncoated sample was 7.6%, almost the same as the other uncoated sample exposed to 3000 ppm CO_2, while the ALD-coated sample appears to have decreased resistance. This leads us to believe that in addition to lowering the interfacial resistance at the Li | garnet interface, the Al_2O_3 coating may act as a protecting layer toward reactions with CO_2.

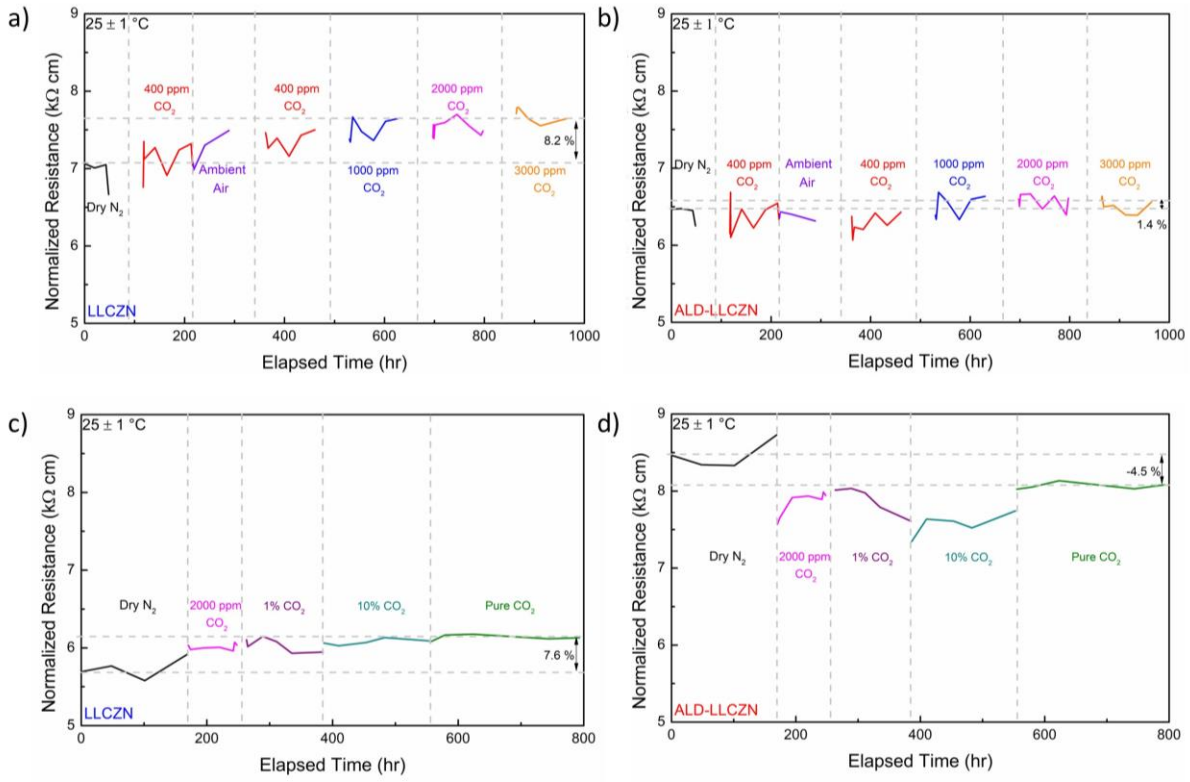

Figure 6.5. Summary of LLCZN impedance in all CO_2 concentrations for (a) uncoated (b) Al_2O_3 coated up to 3000 ppm CO_2. (c) and (d) show normalized impedance up to pure CO_2 for the uncoated and coated samples, respectively.

6.2.2 Ionic stability of $Li_7La_{2.75}Ca_{0.25}Zr_{1.75}Nb_{0.25}O_{12}$ under 3% H_2O

We had taken a similar approach as CO_2 stability for humidity stability. Both Al_2O_3 coated and uncoated samples were transferred from the Ar glovebox to the impedance chamber. The chamber was purged with dry Ar for a minimum of 100-h prior to starting 3% H_2O tests. Purging was performed to ensure no humidity or CO_2 was present prior to starting measurements and confirm

the sample impedance does not change under inert atmospheres. Upon the introduction of 3% H_2O/Ar at 25 ^oC, the emergence of an additional semi-circle in the Nyquist plot was observed. Figure 6.6a and b show the Nyquist plots under dry Ar, 3 % H_2O/Ar (95 h), and recovery Ar (93 h) at 25 °C for the uncoated and coated samples, respectively. The Nyquist plot after exposure to 3% H_2O in the coated samples successfully fit with $R_b(CPE_{gb}R_{gb})CPE_e$ equivalent circuit, Figure 5.6b. Where R_b and R_{gb} are the resistances from the bulk and grain boundary, respectively; CPE_{gb} and CPE_e are the capacitance effects from the grain boundary and Au electrode, respectively. The capacitance associated with the fitted equivalence circuit can be calculated using equation (3.4). Based on this calculation, the additional semi-circle has a capacitance in the order of 10^{-10} F, lying in the range of grain boundary capacitance.[68] Due to the lack of an identifiable semi-circle in the uncoated sample could not be fitted, however, we believe the increase in impedance is also from grain boundary resistance.

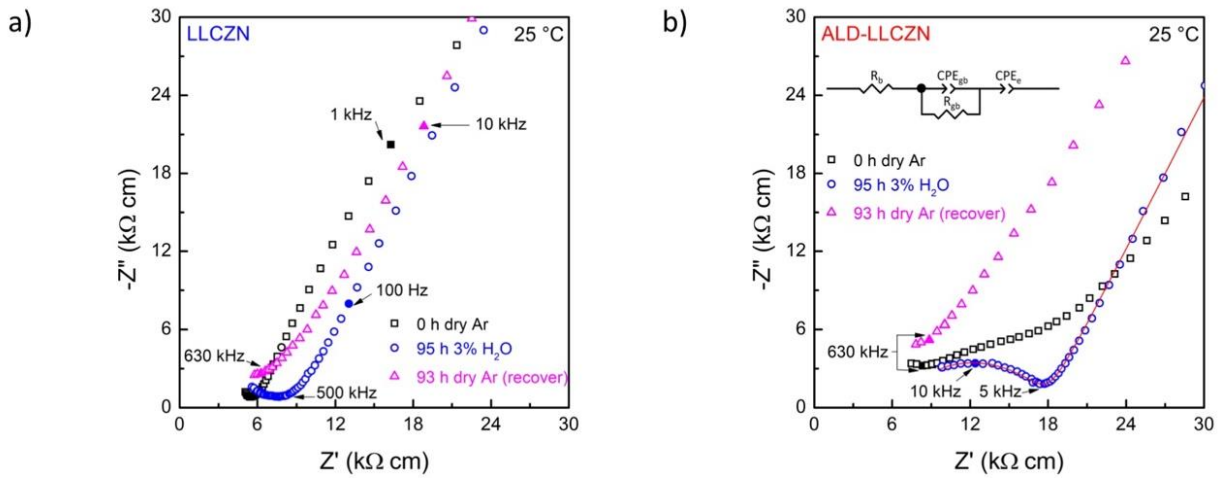

Figure 6.6. Nyquist plots of a) uncoated and b) coated LLCZN samples under dry Ar (black square), 95 h 3% H_2O (blue circle), and upon recovery with 93 h dry Ar (pink triangle). Coated samples exposed to 3% H_2O were fit using $R_b(CPE_{gb}R_{gb})CPE_e$ equivalent circuit, red line shows fit.

Within 1 hour of removing the humidified Ar, the impedance would begin to recover and the grain boundary contributions would begin to retreat. Cycling was performed with numerous samples of both Al_2O_3 coated and uncoated, confirming the reproducibility. Figure 6.7a and b show the normalized total resistance in both dry and humidified Ar. Given that both the Al_2O_3 coated and uncoated samples display the grain-boundary resistance increase in the presence of 3% H_2O, the coating is believed not to act a protecting layer against reactions with humidity unlike reactions with CO_2.

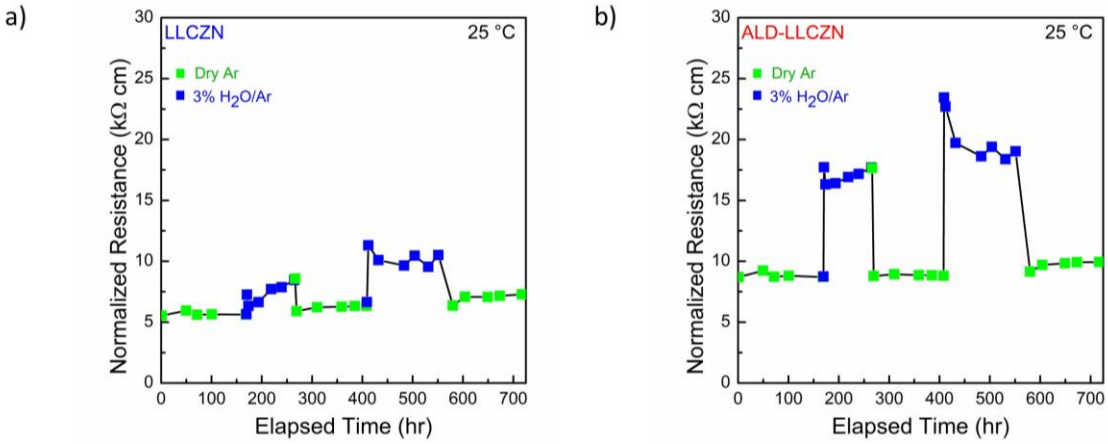

Figure 6.7. Summary of total resistance of samples in dry and humidified Ar for uncoated a) and coated b).

6.2.3 Ionic stability of $Li_7La_{2.75}Ca_{0.25}Zr_{1.75}Nb_{0.25}O_{12}$ under CO_2 and 3% H_2O

Combining the findings of CO_2 atmospheres and humidified Ar, the effect of CO_2 containing gases as a 'recovery' gas was investigated. Following reactions (6.1) and (6.2), after 3% H_2O exposure, the garnet sample should become protonated followed by a LiOH coating which will further react with CO_2 forming a Li_2CO_3 passivation layer. As before, the sample was exposed to 3% H_2O/Ar for 4 hours, enough time to induce the increased grain-boundary impedance. After the 4-hours, 3%

H_2O was removed and 400 ppm CO_2 was introduced, similar to what was seen with the impedance would recover. The experiment was repeated with pure CO_2 and again recovery was observed, as seen in Figure 6.8a and b for both uncoated and coated, respectively. The mechanism for the appearance of grain-boundary like response in the impedance spectra is not yet clear. One possible explanation is that in humid environments, water may adsorb onto the grain boundaries of the polycrystalline garnet material, impeding the Li-ion transport. When the 3% H_2O is removed and dry gas flow is reintroduced, the dry moving gas allows for the adsorbed water to be removed and the impedance to return to that of initial values. The presence of dry gas flow is not necessary as the samples will also begin to recover as soon as 3% H_2O is removed.

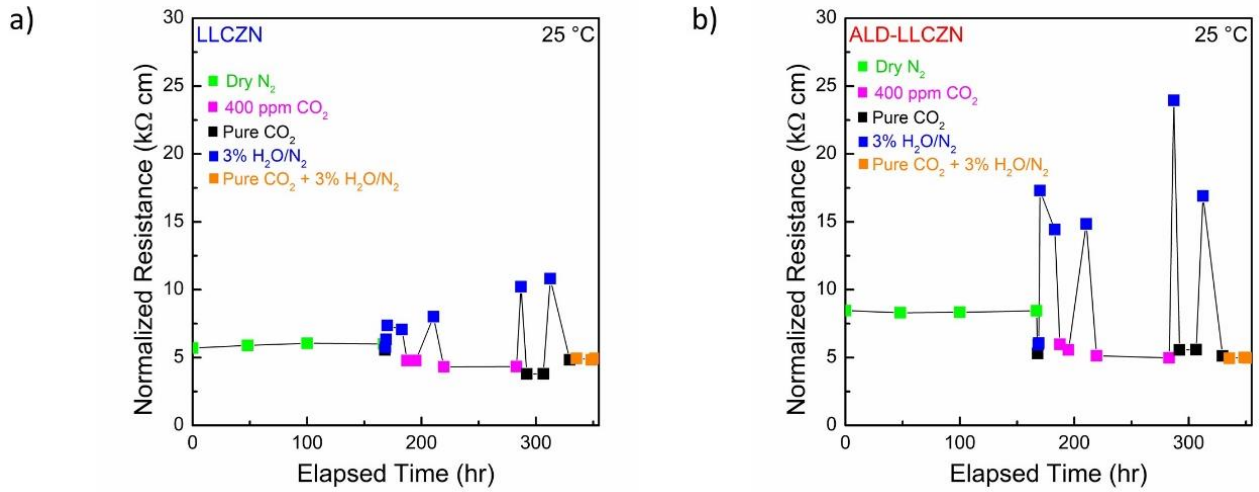

Figure 6.8. Overview of total ionic resistance of a) uncoated and b) coated LLCZN samples when alternated between humidified and CO_2 rich environments.

6.2.4 Morphology and topography studies of $Li_7La_{2.75}Ca_{0.25}Zr_{1.75}Nb_{0.25}O_{12}$ after CO_2 and humidity exposure

6.2.4.1 Topography imaging of $Li_7La_{2.75}Ca_{0.25}Zr_{1.75}Nb_{0.25}O_{12}$ in ambient air

Topography imaging was performed using atomic force microscopy (AFM). The untreated samples were polished like those for electrical conductivity measurements, but with additional

steps of polishing in cloth with 7 and 0.3 µm alumina powder to ensure that the roughness won't impede continuous scanning of the AFM tip. The Al_2O_3 already allowed for a smooth enough surface to be imaged. AFM imaging of LLCZN was conducted under ambient air at room temperature. Images were collected every hour for 5-hours and an additional image collected after 22-hours of exposure to ambient air. The uncoated pristine samples (0 h) shows a maximum height of 690 nm, whereas after 5-hours in ambient air the maximum height became 727 nm and 860 nm after 22-hours (Figures 6.9b-d). Although there is an increase in height, the increase is not concentrated in one area, rather the increase was uniformly distributed. The uniform distributed height increase is likely from a Li_2CO_3 layer formation on the surface of the garnet sample. Similar height increase over the duration of imagining was also seen for the coated samples (Figure 6.9f-h). Figure 6.9 shows the obtained AFM images after the exposure to ambient air for the uncoated and coated LLCZN samples.

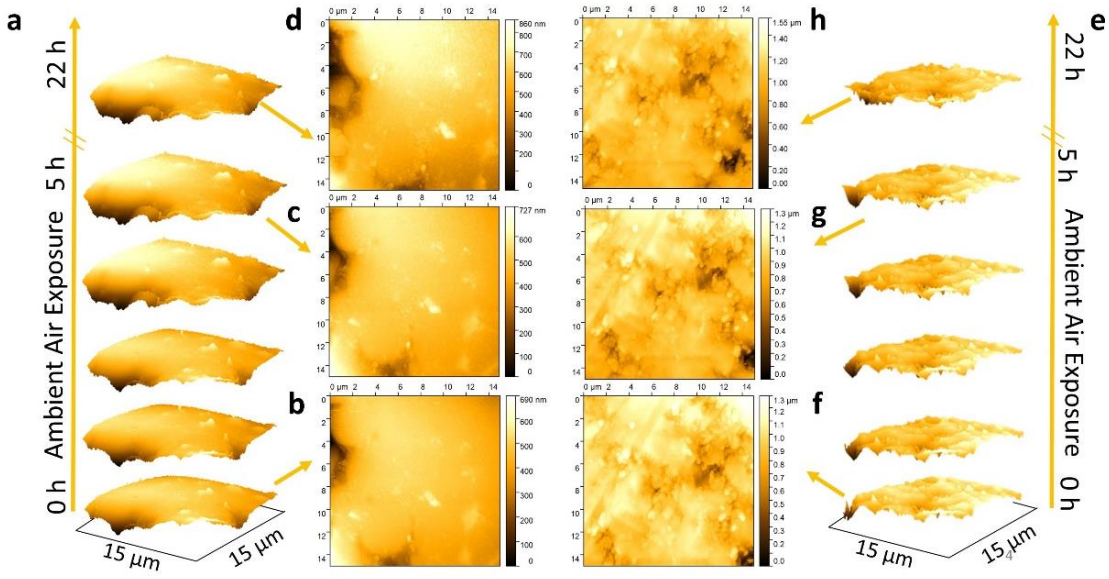

Figure 6.9. AFM imaging of (a-d) uncoated and (e-h) ALD-coated sample. (a) and (e) shows the observed images after every hour of exposure in ambient air of uncoated and ALD-coated samples, respectively. The samples were also left overnight and imaged the following day (after 22 h).

6.2.4.2 In-situ topography studies of $Li_7La_{2.75}Ca_{0.25}Zr_{1.75}Nb_{0.25}O_{12}$ under 3% H_2O.

To investigate is topography of the samples under humid environments, in-situ AFM images were taken of samples under 3% H_2O. The sample was transferred to an environmental AFM chamber allowing the mimic of 3% H_2O/N_2 while imaging was performed. Imaging was collected every hour for 5-hours in the presence of 3% H_2O/N_2, Figure 6.10. When comparing the topography of the pristine (0 h) sample to the topography after 5-hour of 3% H_2O/N_2 exposure, distinct droplet formations are observed, seen in the top left corner of Figures 6.10b and c. For the uncoated sample, the droplet like features show a diameter ~1-2 μm. It is worth noting that this is the is the approximately the same time duration for a prominent increased in grain-boundary to be observed from the electrochemical impedance spectroscopy.

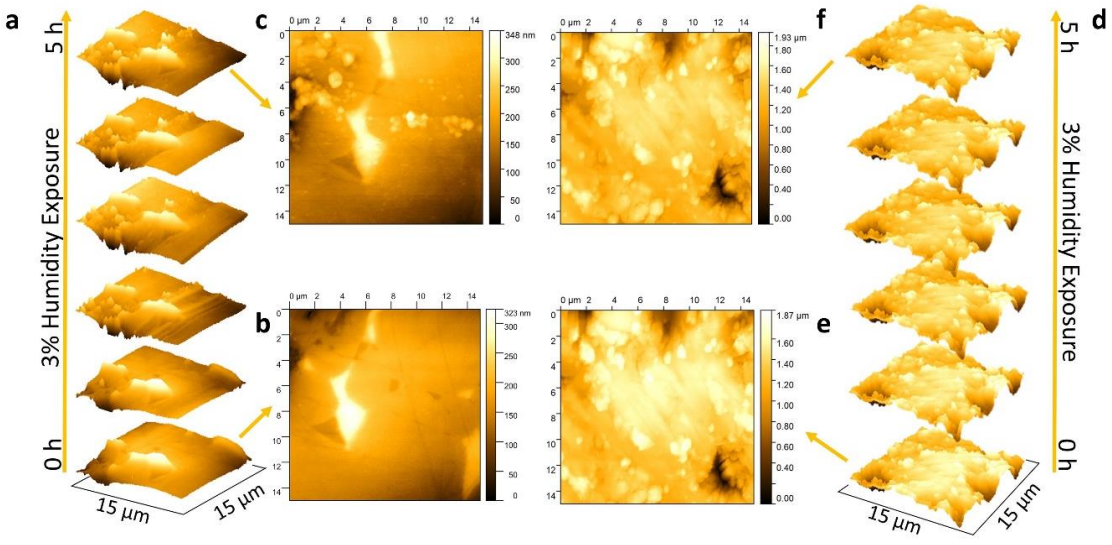

Figure 6.10. AFM imaging of (a-c) uncoated and (d-f) ALD-coated sample. (a) and (d) shows the observed images after every hour of exposure in 3% H_2O/N_2 of uncoated and ALD-coated samples, respectively.

6.2.4.3 In-situ scanning electron microscopy studies of $Li_7La_{2.75}Ca_{0.25}Zr_{1.75}Nb_{0.25}O_{12}$ under humidity.

Environmental scanning electron microscopy (E-SEM) images were collected for the uncoated $Li_7La_{2.75}Ca_{0.25}Zr_{1.75}Nb_{0.25}O_{12}$ sample in the presence of humidity. The relative humidity was held at approximately 90 %, while the sample was between 13-17 ^oC, this kept the sample just above the dew point for the given pressure within the vacuum chamber. Within 30 minutes, the pores filled with water followed by the entire surface becoming flooded, Figure 6.11 show the time-resolved in-situ scanning electron microscopy images. After removing the humidity and elevating the temperature of the sample to 25 ^oC, the water within the pores evaporated leaving behind a LiOH layer, seen in the last panel of Figure 6.11.

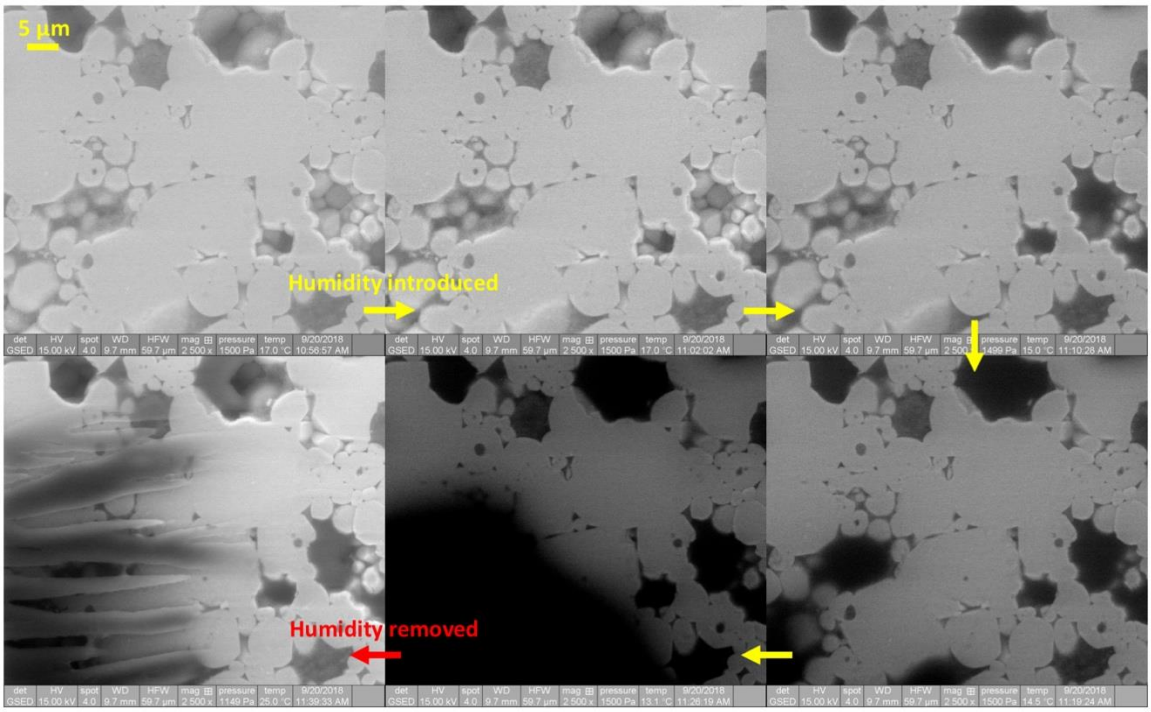

Figure 6.11 In-situ scanning electron microscopy images of LLCZN in a humid atmosphere.

Coupling the AFM and in-situ SEM images, it is seen that in the presence of humidity, it appears that water will adsorb to the surface of the lithium-garnet and thus encase the grains with water. As a result, the EIS spectra indicates a grain-boundary resistance increase in the presence of humidity. Although the mechanism for the increase in grain boundary impedance is still not clear. One possible explanation is that in humid environments, water may adsorb onto the grain boundaries of the polycrystalline garnet material, impeding the Li-ion transport. Which can be evaporated upon removal of humidity.

6.3 Summary

To summarize, lithium-garnet $Li_7La_{2.75}Ca_{0.25}Zr_{1.75}Nb_{0.25}O_{12}$ were coated with a thin Al_2O_3 layer in order to reduce interfacial resistance with Li. Lithium-garnet materials are reported to react with CO_2 and 3% H_2O, forming Li_2CO_3. However, based on EIS studies presented here, when the Al_2O_3 coating is applied, the Li-ion conductivity is not drastically affected by the CO_2 rich atmospheres whereas uncoated samples are. An ~ 8 % increase in resistance is observed for uncoated samples, where coated show ~ 1 % resistance increase over nearly 1000 h in 3000 ppm CO_2. In the presences of 3% H_2O, both the coated and uncoated samples show large grain-boundary like resistance increases, upon removal of 3% H_2O, the resistance will resume to that of original dry Ar/N_2 like conditions. AFM images suggest that a Li_2CO_3 layer is formed on the surface by a uniformly distributed height increase in ambient conditions. In-situ humidified AFM and SEM imaging has revealed that water may absorb to the surface and sit within the grain boundaries, potentially impeding the Li-ion mobility.

Chapter Seven: **Conclusions and future work**

7.1 Conclusions

The main focus of this study was to develop an understanding of the chemical and electrochemical stability of lithium-garnets in aqueous solution, with humidity and CO_2, and metallic Li. The conclusions of each chapter that have been derived from this thesis have been divided into the subsections below.

7.1.1 Conclusions on aqueous stability of lithium-garnet $Li_{6.5}La_{2.5}Ba_{0.5}ZrTaO_{12}$

In Chapter 4, $Li_{6.5}La_{2.5}Ba_{0.5}ZrTaO_{12}$ was prepared via solid-state synthesis at elevated temperatures, in air. Samples were treated with either water, D_2O, 1 M LiOH, 1 M LiCl, or brine (0.1 M LiCl, 0.1 M $NaNO_3$, 0.1 M K_2CO_3) for up to 10 days. Thermogravimetric analysis reveals that $Li_{6.5}La_{2.5}Ba_{0.5}ZrTaO_{12}$ undergoes a Li^+/H^+ reaction, based on the loss of crystalline water in the temperature range 200-550 ^oC. Powder form samples more readily undergo ion-exchange compared to pellet. In both power and pellet form, samples treated with D_2O would show the least ion-exchange followed by water, 1 M LiOH, and 1 M LiCl. XRD confirmed that the cubic garnet-type crystal structure was retained after aqueous solution treatment, suggesting a topotactic reaction. Variable temperature XRD also shows upon heating the protonated sample up to 650 ^oC, the garnet structure is still retained, although the crystalline water would have left. More intensive studied with TEM and ED further support that the garnet-type crystal structure is retained after treatment with solution. The Li-ion conductivity was monitored daily, in all cases samples would show an increase in conductivity within the first 10 days with respect to time zero but would stabilize thereafter.

7.1.2 Conclusions on electrochemical stability of lithium garnets $Li_{6.5}La_{2.5}Ba_{0.5}ZrTaO_{12}$ and $Li_7La_{2.75}Ca_{0.25}Zr_{1.75}Nb_{0.25}O_{12}$

7.1.2.1 Electrochemical stability of $Li_{6.5}La_{2.5}Ba_{0.5}ZrTaO_{12}$

Having developed an understanding of the ionic and structural stability of $Li_{6.5}La_{2.5}Ba_{0.5}ZrTaO_{12}$ in aqueous media, further investigations on the stability with Li were performed to determine the feasibility of using lithium-garnets in aqueous Li-O_2 cells. Using DC polarization and Li symmetric cells, lithium was successfully plated and stripped at current densities of 39 84, and 169 $\mu A\ cm^2$, doing so the area specific interfacial resistance was determined to be 473 $\Omega\ cm^2$. Combining the findings in Chapter 4, the lithium-garnet $Li_{6.5}La_{2.5}Ba_{0.5}ZrTaO_{12}$ was employed as a protective layer for an aqueous Li-O_2 cell, with a stable ~3 V observed when 0.1 M LiOH, 1 M LiOH, and 1 M LiCl electrolytes were used.

7.1.2.2 Electrochemical stability of $Li_7La_{2.75}Ca_{0.25}Zr_{1.75}Nb_{0.25}O_{12}$

To further understand the electrochemical stability of lithium-garnets, $Li_7La_{2.75}Ca_{0.25}Zr_{1.75}Nb_{0.25}O_{12}$ was investigated to determine the electrochemical stability window. Cyclic voltammetry show that the lithium-garnet is stable up to 6 V vs. Li/Li^+, suggesting its potential use with high voltage cathode materials. Hebb-Wagner DC polarization experiments reveal that lithium-garnets are predominantly Li-ion conductors, with transference values ~0.99.

7.1.3 Conclusions on gaseous stability of lithium-garnet $Li_7La_{2.75}Ca_{0.25}Zr_{1.75}Nb_{0.25}O_{12}$

Al_2O_3 coating via atomic layer deposition on lithium-garnet, $Li_7La_{2.75}Ca_{0.25}Zr_{1.75}Nb_{0.25}O_{12}$ samples were investigated for its potential as a protective layer against reactions with 3% H_2O and CO_2. Samples without the Al_2O_3 showed an 8.2 % increase in Li-ion resistance based on EIS when exposed to CO_2 for 1000 h and up to 3000 ppm. Whereas samples with the Al_2O_3 coating only showed a Li-ion resistance increase of 1.4 %. When a similar experiment was performed with pure

CO_2, uncoated samples showed an increase of 7.6% (over 800 h) and coated showed -4.5% over the sample exposure. Suggesting the Al_2O_3 protects lithium-garnets from reactions with CO_2.

The same cannot be said when exposed to 3% H_2O. Samples with and without Al_2O_3 coatings show large grain-boundary resistance increases, which are recoverable upon the reintroduction of dry Ar, N_2, ambient air or CO_2. Based on AFM and SEM imaging, humidity appears to cause water to form on the surface of the grains and potentially impede the Li-ion mobility, however the mechanism is still unclear.

7.2 Future work

Below are summarized suggestions for future work in extension to the current work reported in this thesis.

- The studies performed have determined the total conductivity which is dominated by Li-ion migration, however, potential proton contribution to the total conductivity in the protonated garnets must be determined. Neutron diffraction studied of protonated samples can determine the site(s) at which the ion-exchange occurs. By determination of these sites, this may also reveal the potential migration pathway of protons. Further solid-state NMR studies can help lead insight towards proton migration (and pathways) within the lithium-garnet structure.
- Many of the aqueous stability studies were performed on a 10-day time scale, this is well below the requirement for batteries intended for commercial use. To further investigate the stability of lithium-garnets in solution, samples should be investigated following immersion in solution after for months to years.

- The current thesis reported that garnet-type $Li_{6.5}La_{2.5}Ba_{0.5}ZrTaO_{12}$ metal oxides have potential as Li anode protective layers in aqueous Li-O_2 battery configurations. However, thin film approaches such as tape casting, sol-gel, and sputtering techniques can also be tried in order to achieve low resistance cells.
- Humidity exposure to lithium-garnet in this thesis work has evoked many questions to be answered. First of all, determination of the mechanism in which humidity interacts with the garnet surface is required. Brunauer-Emmett-Teller (BET) studies can be performed to follow the absorption of water to the garnet surface along with *in-situ* impedance.

References

1. Linden, D.; Reddy, T. B., *Handbook of batteries*. 3rd ed.; McGraw-Hill: New York, 2002.

2. Manthiram, A., An Outlook on Lithium Ion Battery Technology. *ACS Cent. Sci.* **2017,** *3* (10), 1063-1069.

3. Kalhoff, J.; Eshetu, G. G.; Bresser, D.; Passerini, S., Safer Electrolytes for Lithium-Ion Batteries: State of the Art and Perspectives. *ChemSusChem* **2015,** *8* (13), 2154-2175.

4. Tarascon, J. M.; Armand, M., Issues and challenges facing rechargeable lithium batteries. *Nat.* **2001,** *414*, 359.

5. Hofstetter, K.; Samson, A. J.; Narayanan, S.; Thangadurai, V., Present understanding of the stability of Li-stuffed garnets with moisture, carbon dioxide, and metallic lithium. *J. Power Sources* **2018,** *390*, 297-312.

6. Goodenough, J. B.; Park, K. S., The Li-Ion Rechargeable Battery: A Perspective. *J. of the Am. Chem. Soc.* **2013,** *135* (4), 1167-1176.

7. Change, N. G. C., Carbon dioxide concentration | NASA Global Climate Change. **2018**.

8. Dunn, B.; Kamath, H.; Tarascon, J.-M., Electrical Energy Storage for the Grid: A Battery of Choices. *Science* **2011**, *334*, 928-935.

9. Mizushima, K.; Jones, P. C.; Wiseman, P. J.; Goodenough, J. B., Li_xCoO_2 ($0<x\leq1$): A new cathode material for batteries of high energy density. *Mater. Res. Bull.* **1980,** *15* (6), 783-789.

10. Nishi, Y., Lithium ion secondary batteries; past 10 years and the future. *J. Power Sources* **2001,** *100* (1), 101-106.

11. Blomgren, G. E., The Development and Future of Lithium Ion Batteries. *Journal of Electrochemical Society* **2017,** *164* (1), A5019-A5025.

12. Aurbach, D.; Talyosef, Y.; Markovsky, B.; Markevich, E.; Zinigrad, E.; Asraf, L.; Gnanaraj, J. S.; Kim, H.-J., Design of electrolyte solutions for Li and Li-ion batteries: a review. *Electrochimica Acta* **2004,** *50* (2), 247-254.

13. Arteaga, J.; Zareipour, H.; Thangadurai, V., Overview of Lithium-Ion Grid-Scale Energy Storage Systems. *Curr Sustainable Renewable Energy Rep*. **2018**, 4, 197.

14. EV everywhere: Grand Challenge. Energy. **2014**.

15. Bruce, P. G.; Freunberger, S. A.; Hardwick, L. J.; Tarascon, J.-M., Li–O_2 and Li–S batteries with high energy storage. *Nat. Mater* **2011,** *11*, 19-29**.**

16. Li, Y. T.; Xu, B. Y.; Xu, H. H.; Duan, H. N.; Lu, X. J.; Xin, S.; Zhou, W. D.; Xue, L. G.; Fu, G. T.; Manthiram, A.; Goodenough, J. B., Hybrid Polymer/Garnet Electrolyte with a Small Interfacial Resistance for Lithium-Ion Batteries. *Angew. Chem. Int. Ed.* **2017,** *56* (3), 753-756.

17. Manthiram, A.; Yu, X.; Wang, S., Lithium battery chemistries enabled by solid-state electrolytes. *Nat. Rev. Mater.* **2017,** *2*, 16103.

18. Thangadurai, V.; Narayanan, S.; Pinzaru, D., Garnet-type solid-state fast Li ion conductors for Li batteries: critical review. *Chem. Soc. Rev* **2014,** *43* (13), 4714-4727.

19. Goodenough, J. B.; Hong, H. Y. P.; Kafalas, J. A., Fast Na^+-ion transport in skeleton structures. *Mater. Res. Bull* **1976,** *11* (2), 203-220.

20. Thangadurai, V. W., Weppner., Recent progress in solid oxide and lithium ion conducting electrolytes research. *Ionics* **2006,** *12* (1), 81-92.

21. Cretin, M.; Fabry, P., Comparative study of lithium ion conductors in the system $Li_{1+x}Al_xA_{2-x}IV\ (PO_4)_3$ with AIV=Ti or Ge and $0 \leq x \leq 0.7$ for use as Li^+ sensitive membranes. *J. Eur. Ceram. Soc* **1999,** *19* (16), 2931-2940.

22. Savitha., T.; Selvasekarapandian., S.; Ramya., C. S.; Bhuvaneswari., M. S.; Angelo, P. C., Electrical conduction and relaxation mechanism in $Li_2AlZr[PO_4]_3$. *J. of Mater. Sci* **2007,** *14*, 5470-5475.

23. Catti, M.; Morgante, N.; Ibberson, R. M., Order–Disorder and Mobility of Li^+ in the β′- and β-$LiZr_2(PO_4)_3$ Ionic Conductors: A Neutron Diffraction Study. *J. Solid State Chem* **2000,** *152* (2), 340-347.

24. Robertson, A. D.; West, A. R.; Ritchie, A. G., Review of crystalline lithium-ion conductors suitable for high temperature battery applications. *Solid State Ionics* **1997,** *104* (1), 1-11.

25. Hong, H. Y. P., Crystal structure and ionic conductivity of $Li_{14}Zn(GeO_4)_4$ and other new Li+ superionic conductors. *Mater. Res. Bull* **1978,** *13* (2), 117-124.

26. Stramare, S.; Thangadurai, V.; Weppner, W., Lithium Lanthanum Titanates: A Review. *Chem. Mater.* **2003,** *15* (21), 3974-3990.

27. Inaguma, Y.; Liquan, C.; Itoh, M.; Nakamura, T.; Uchida, T.; Ikuta, H.; Wakihara, M., High ionic conductivity in lithium lanthanum titanate. *Solid State Commun* **1993,** *86* (10), 689-693.

28. Mazza, D., Remarks on a ternary phase in the La_2O_3 Me_2O_5 Li_2O system (Me=Nb, Ta). *Mater. Lett* **1988,** *7* (5), 205-207.

29. Thangadurai, V.; Kaack, H.; Weppner, W. J. F., Novel Fast Lithium Ion Conduction in Garnet-Type $Li_5La_3M_2O_{12}$ (M = Nb, Ta). *J. Am. Ceram. Soc.* **2003,** *86* (3), 437-440.

30. O'Callaghan, M. P.; Lynham, D. R.; Cussen, E. J.; Chen, G. Z., Structure and Ionic-Transport Properties of Lithium-Containing Garnets $Li_3Ln_3Te_2O_{12}$ (Ln = Y, Pr, Nd, Sm−Lu). *Chem.Mater* **2006,** *18* (19), 4681-4689.

31. Cussen, E. J., The structure of lithium garnets: cation disorder and clustering in a new family of fast Li^+ conductors. *Chem. Comm* **2006,** (4), 412-413.

32. Cussen, E. J., Structure and ionic conductivity in lithium garnets. *J. Mater. Chem* **2010,** *20* (25), 5167-5173.

33. Miara, L. J.; Richards, W. D.; Wang, Y. E.; Ceder, G., First-Principles Studies on Cation Dopants and Electrolyte|Cathode Interphases for Lithium Garnets. *Chem.Mater.* **2015,** *27* (11), 4040-4047.

34. Murugan, R.; Thangadurai, V.; Weppner, W., Fast Lithium Ion Conduction in Garnet-Type $Li_7La_3Zr_2O_{12}$. *Angew. Chem. Int. Ed* **2007,** *46* (41), 7778-7781.

35. Han, X. G.; Gong, Y. H.; Fu, K.; He, X. F.; Hitz, G. T.; Dai, J. Q.; Pearse, A.; Liu, B. Y.; Wang, H.; Rublo, G.; Mo, Y. F.; Thangadurai, V.; Wachsman, E. D.; Hu, L. B., Negating interfacial impedance in garnet-based solid-state Li metal batteries. *Nat. Mater* **2017,** *16* (5), 572.

36. Kumazaki, S.; Iriyama, Y.; Kim, K.-H.; Murugan, R.; Tanabe, K.; Yamamoto, K.; Hirayama, T.; Ogumi, Z., High lithium ion conductive $Li_7La_3Zr_2O_{12}$ by inclusion of both Al and Si. *Electrochem. Commun.* **2011,** *13* (5), 509-512.

37. Nyman, M.; Alam, T. M.; McIntyre, S. K.; Bleier, G. C.; Ingersoll, D., Alternative Approach to Increasing Li Mobility in Li-La-Nb/Ta Garnet Electrolytes. *Chem. Mater* **2010,** *22* (19), 5401-5410.

38. Truong, L.; Thangadurai, V., Soft-Chemistry of Garnet-Type $Li_{5+x}Ba_xLa_{3-x}Nb_2O_{12}$ (x = 0, 0.5, 1): Reversible $H^+ \leftrightarrow Li^+$ Ion-Exchange Reaction and Their X-ray, ^7Li MAS NMR, IR, and AC Impedance Spectroscopy Characterization. *Chem. Mater* **2011,** *23* (17), 3970-3977.

39. Truong, L.; Colter, J.; Thangadurai, V., Chemical stability of Li-stuffed garnet-type $Li_{5+x}Ba_xLa_{3-x}Ta_2O_{12}$ (x=0, 0.5, 1) in water: a comparative analysis with the Nb analogue. *Solid State Ionics* **2013,** *247-248*, 1-7.

40. Truong, L.; Howard, M.; Clemens, O.; Knight, K. S.; Slater, P. R.; Thangadurai, V., Facile proton conduction in H^+/Li^+ ion-exchanged garnet-type fast Li-ion conducting $Li_5La_3Nb_2O_{12}$. *J. Mater. Chem. A* **2013,** *1* (43), 13469-13475.

41. Orera, A.; Larraz, G.; Rodríguez-Velamazán, J. A.; Campo, J.; Sanjuán, M. L., Influence of Li^+ and H^+ Distribution on the Crystal Structure of $Li_{7-x}H_xLa_3Zr_2O_{12}$ ($0 \leq x \leq 5$) Garnets. *Inorg. Chem* **2016,** *55* (3), 1324-1332.

42. Galven, C.; Dittmer, J.; Suard, E.; Le Berre, F.; Crosnier-Lopez, M.-P., Instability of Lithium Garnets against Moisture. Structural Characterization and Dynamics of $Li_{7-x}H_xLa_3Sn_2O_{12}$ and $Li_{5-x}H_xLa_3Nb_2O_{12}$. *Chem. Mater* **2012,** *24* (17), 3335-3345.

43. Sanjuan, M. L.; Orera, A.; Sobrados, I.; Fuentes, A. F.; Sanz, J., Structural transition in orthorhombic $Li_{5-x}H_xLa_3Nb_2O_{12}$ garnets induced by a concerted lithium and proton diffusion mechanism. *J. Mater. Chem. A* **2018,** *6* (6), 2708-2720.

44. Truong, L.; Thangadurai, V., First Total H^+/Li^+ Ion Exchange in Garnet-Type $Li_5La_3Nb_2O_{12}$ Using Organic Acids and Studies on the Effect of Li Stuffing. *Inorg. Chem* **2012,** *51* (3), 1222-1224.

45. Galven, C.; Suard, E.; Mounier, D.; Crosnier-Lopez, M.-P.; Le Berre, F., Structural characterization of a new acentric protonated garnet: $Li_{6-x}H_xCaLa_2Nb_2O_{12}$. *J. Mater. Res* **2013,** *28* (16), 2147-2153.

46. Hofstetter, K.; Samson, A. J.; Thangadurai, V., Characterization of lithium-rich garnet-type $Li_{6.5}La_{2.5}Ba_{0.5}ZrTaO_{12}$ for beyond intercalation chemistry-based lithium-ion batteries. *Solid State Ionics* **2017**.

47. Larraz, G.; Orera, A.; Sanjuan, M. L., Cubic phases of garnet-type $Li_7La_3Zr_2O_{12}$: the role of hydration. *J. Mater. Chem. A* **2013,** *1* (37), 11419-11428.

48. Galven, C.; Fourquet, J.-L.; Crosnier-Lopez, M.-P.; Le Berre, F., Instability of the Lithium Garnet $Li_7La_3Sn_2O_{12}$: Li^+/H^+ Exchange and Structural Study. *Chemistry of Materials* **2011,** *23* (7), 1892-1900.

49. Buschmann, H.; Dolle, J.; Berendts, S.; Kuhn, A.; Bottke, P.; Wilkening, M.; Heitjans, P.; Senyshyn, A.; Ehrenberg, H.; Lotnyk, A.; Duppel, V.; Kienle, L.; Janek, J., Structure and dynamics of the fast lithium ion conductor "$Li_7La_3Zr_2O_{12}$". *Phys. Chem. Chem. Phys* **2011,** *13* (43), 19378-19392.

50. Ma, C.; Rangasamy, E.; Liang, C.; Sakamoto, J.; More, K. L.; Chi, M., Excellent Stability of a Lithium-Ion-Conducting Solid Electrolyte upon Reversible Li^+/H^+ Exchange in Aqueous Solutions. *Angew. Chem. Int. Ed* **2015,** *54* (1), 129-133.

51. O'Callaghan, M. P.; Cussen, E. J., Lithium dimer formation in the Li-conducting garnets $Li_{5+x}Ba_xLa_{3-x}Ta_2O_{12}$ ($0 < x \leq 1.6$). *Chem. Comm* **2007,** (20), 2048-2050.

52. Sharafi, A.; Yu, S.; Naguib, M.; Lee, M.; Ma, C.; Meyer, H. M.; Nanda, J.; Chi, M.; Siegel, D. J.; Sakamoto, J., Impact of air exposure and surface chemistry on Li-$Li_7La_3Zr_2O_{12}$ interfacial resistance. *J. Mater. Chem. A* **2017,** *5* (26), 13475-13487.

53. Galven, C.; Corbel, G.; Le Berre, F.; Crosnier-Lopez, M.-P., Instability of the Ionic Conductor $Li_6BaLa_2B_2O_{12}$ (B = Nb, Ta): Barium Exsolution from the Garnet Network Leading to CO_2 Capture. *Inorg. Chem* **2016,** *55* (24), 12872-12880.

54. Li, Y.; Wang, C.-A.; Xie, H.; Cheng, J.; Goodenough, J. B., High lithium ion conduction in garnet-type $Li_6La_3ZrTaO_{12}$. *Electrochem. Commun* **2011,** *13* (12), 1289-1292.

55. Nemori, H.; Matsuda, Y.; Mitsuoka, S.; Matsui, M.; Yamamoto, O.; Takeda, Y.; Imanishi, N., Stability of garnet-type solid electrolyte $Li_xLa_3A_{2-y}B_yO_{12}$ (A=Nb or Ta, B=Sc or Zr). *Solid State Ionics* **2015,** *282*, 7-12.

56. Kim, Y.; Yoo, A.; Schmidt, R.; Sharafi, A.; Lee, H.; Wolfenstine, J.; Sakamoto, J., Electrochemical Stability of $Li_{6.5}La_3Zr_{1.5}M_{0.5}O_{12}$ (M = Nb or Ta) against Metallic Lithium. *Front. Energy Res.* **2016,** *4*, 7.

57. Peng, H. J.; Wu, Q.; Xiao, L. H., Low temperature synthesis of $Li_5La_3Nb_2O_{12}$ with cubic garnet-type structure by sol-gel process. *J. Sol-Gel Sci.Technol* **2013,** *66* (1), 175-179.

58. Ohta, S.; Kobayashi, T.; Asaoka, T., High lithium ionic conductivity in the garnet-type oxide $Li_{7-X}La_3(Zr_{2-X}, Nb_X)O_{12}$ (X=0–2). *Journal of Power Sources* **2011,** *196* (6), 3342-3345.

59. Yu, S.; Schmidt, R. D.; Garcia-Mendez, R.; Herbert, E.; Dudney, N. J.; Wolfenstine, J. B.; Sakamoto, J.; Siegel, D. J., Elastic Properties of the Solid Electrolyte $Li_7La_3Zr_2O_{12}$ (LLZO). *Chem. Mater* **2015,** *28* (1), 197-206.

60. Monroe, C.; Newman, J., The Impact of Elastic Deformation on Deposition Kinetics at Lithium/Polymer Interfaces. *J. Electrochem. Soc* **2005,** *152*, A396-A404.

61. Stone, G. M.; Mullin, S. A.; Teran, A. A.; D. T. Hallinan, J.; Minor, A. M.; Hexemer, A.; Balsara, N. P., Resolution of the Modulus versus Adhesion Dilemma in Solid Polymer Electrolytes for Rechargeable Lithium Metal Batteries. *J. Electrochem. Soc* **2012,** *159*, A222-A227.

62. Lin, D.; Liu, Y.; Cui, Y., Reviving the lithium metal anode for high-energy batteries. *Nat. Nano* **2017,** *12* (3), 194.

63. Kotobuki, M.; Munakata, H.; Kanamura, K.; Sato, Y.; Yoshida, T., Compatibility of $Li_7La_3Zr_2O_{12}$ Solid Electrolyte to All-Solid-State Battery Using Li Metal Anode. *J. Electrochem. Soc* **2010,** *157* (10), A1076-A1079.

64. Cheng, L.; Chen, W.; Kunz, M.; Persson, K.; Tamura, N.; Chen, G. Y.; Doeff, M., Effect of Surface Microstructure on Electrochemical Performance of Garnet Solid Electrolytes. *ACS Appl. Mater. Interfaces* **2015,** *7* (3), 2073-2081.

65. Wang, C.; Gong, Y.; Liu, B.; Fu, K.; Yao, Y.; Hitz, E.; Li, Y.; Dai, J.; Xu, S.; Luo, W.; Wachsman, E. D.; Hu, L., Conformal, Nanoscale ZnO Surface Modification of Garnet-Based Solid-State Electrolyte for Lithium Metal Anodes. Nano Lett **2016**, 12, 565-571.

66. Luo, W.; Gong, Y. H.; Zhu, Y. Z.; Fu, K. K.; Dai, J. Q.; Lacey, S. D.; Wang, C. W.; Liu, B. Y.; Han, X. G.; Mo, Y. F.; Wachsman, E. D.; Hu, L. B., Transition from Superlithiophobicity to Superlithiophilicity of Garnet Solid-State Electrolyte. *J.Am. Chem. Soc* **2016,** *138* (37), 12258-12262.

67. Luo, W.; Gong, Y. H.; Zhu, Y. Z.; Li, Y. J.; Yao, Y. G.; Zhang, Y.; Fu, K.; Pastel, G.; Lin, C. F.; Mo, Y. F.; Wachsman, E. D.; Hu, L. B., Reducing Interfacial Resistance between Garnet-Structured Solid-State Electrolyte and Li-Metal Anode by a Germanium Layer. *Adv. Mater* **2017,** *29* (22), 7.

68. Irvine, J. T. S.; Sinclair, D. C.; West, A. R., Electroceramics: Characterization by Impedance Spectroscopy. *Adv. Mater* **1990,** *2* (3), 132-138.

69. West, A., *Solid State Chemistry and its Applications*. Wiley: 1991.

70. Brug, G. J.; van den Eeden, A. L. G.; Sluyters-Rehbach, M.; Sluyters, J. H., The analysis of electrode impedances complicated by the presence of a constant phase element. *J. Electroanal. Chem* **1984,** *176* (1), 275-295.

71. Huggins, R. A., Simple method to determine electronic and ionic components of the conductivity in mixed conductors a review. *Ionics* **2002,** *8* (3), 300-313.

72. Thangadurai, V.; Weppner, W., $Li_6ALa_2Ta_2O_{12}$ (A = Sr, Ba): Novel Garnet-Like Oxides for Fast Lithium Ion Conduction. *Adv. Funct. Mater* **2005,** *15* (1), 107-112.

73. Narayanan, S.; Hitz, G. T.; Wachsman, E. D.; Thangadurai, V., Effect of Excess Li on the Structural and Electrical Properties of Garnet-Type $Li_6La_3Ta_{1.5}Y_{0.5}O_{12}$. *J. Electrochem. Soc* **2015,** *162* (9), A1772-A1777.

74. Huang, X.; Lu, Y.; Guo, H.; Song, Z.; Xiu, T.; Badding, M. E.; Wen, Z., None-Mother-Powder Method to Prepare Dense Li-Garnet Solid Electrolytes with High Critical Current Density. *ACS Appl. Energy Mater* **2018**, 10, 5355-5365.

75. Dobretsov, E. A.; Mateyshina, Y. G.; Uvarov, N. F., Influence of lithium oxide excess and alumina on grain boundary resistance of $Li_{6.75}La_3Zr_{1.75}Nb_{0.25}O_{12}$ solid electrolyte. *Solid State Ionics* **2017,** *299*, 55-59.

76. Li, Y.; Han, J.-T.; Wang, C.-A.; Vogel, S. C.; Xie, H.; Xu, M.; Goodenough, J. B., Ionic distribution and conductivity in lithium garnet $Li_7La_3Zr_2O_{12}$. *J. Power Sources* **2012,** *209*, 278-281.

77. Awaka, J.; Kijima, N.; Hayakawa, H.; Akimoto, J., Synthesis and structure analysis of tetragonal $Li_7La_3Zr_2O_{12}$ with the garnet-related type structure. *J. Solid State Chem* **2009,** *182* (8), 2046-2052.

78. Xie, H.; Li, Y.; Goodenough, J. B., Low-temperature synthesis of $Li_7La_3Zr_2O_{12}$ with cubic garnet-type structure. *Mater. Res. Bull* **2012,** *47* (5), 1229-1232.

79. Kokal, I.; Somer, M.; Notten, P. H. L.; Hintzen, H. T., Sol–gel synthesis and lithium ion conductivity of $Li_7La_3Zr_2O_{12}$ with garnet-related type structure. *Solid State Ionics* **2011,** *185* (1), 42-46.

80. Narayanan, S.; Epp, V.; Wilkening, M.; Thangadurai, V., Macroscopic and microscopic Li^+ transport parameters in cubic garnet-type "$Li_{6.5}La_{2.5}Ba_{0.5}ZrTaO_{12}$" as probed by impedance spectroscopy and NMR. *RSC Advances* **2012,** *2* (6), 2553-2561.

81. Ramzy, A.; Thangadurai, V., Tailor-Made Development of Fast Li Ion Conducting Garnet-Like Solid Electrolytes. *Acs Applied Materials & Interfaces* **2010,** *2* (2), 385-390.

82. Wu, J.-F.; Pang, W. K.; Peterson, V. K.; Wei, L.; Guo, X., Garnet-Type Fast Li-Ion Conductors with High Ionic Conductivities for All-Solid-State Batteries. *ACS Appl. Mater. Interfaces* **2017,** *9* (14), 12461-12468.

83. Narayanan, S.; Ramezanipour, F.; Thangadurai, V., Dopant Concentration–Porosity–Li-Ion Conductivity Relationship in Garnet-Type $Li_{5+2x}La_3Ta_{2-x}Y_xO_{12}$ ($0.05 \leq x \leq 0.75$) and Their Stability in Water and 1 M LiCl. *Inorg. Chem.* **2015,** *54* (14), 6968-6977.

84. Grillo, V.; Rossi, F., Stem_cell: A software tool for electron microscopy.
part 2 analysis of crystalline materials. *Ultramicroscopy* **2013,** *125*, 112–129

85. Safanama, D.; Adams, S., High efficiency aqueous and hybrid lithium-air batteries enabled by $Li_{1.5}Al_{0.5}Ge_{1.5}(PO_4)_3$ ceramic anode-protecting membranes. *J. Power Sources* **2017,** *340*, 294-301.

86. He, P.; Zhang, T.; Jiang, J.; Zhou, H., Lithium–Air Batteries with Hybrid Electrolytes. *J. Phys. Chem. Lett* **2016,** *7* (7), 1267-1280.

87. Wu, J.-F.; Chen, E.-Y.; Yu, Y.; Liu, L.; Wu, Y.; Pang, W. K.; Peterson, V. K.; Guo, X., Gallium-Doped $Li_7La_3Zr_2O_{12}$ Garnet-Type Electrolytes with High Lithium-Ion Conductivity. *ACS Appl. Mater. Interfaces* **2017,** *9* (2), 1542-1552.

88. Sharafi, A.; Kazyak, E.; Davis, A. L.; Yu, S.; Thompson, T.; Siegel, D. J.; Dasgupta, N. P.; Sakamoto, J., Surface Chemistry Mechanism of Ultra-Low Interfacial Resistance in the Solid-State Electrolyte $Li_7La_3Zr_2O_{12}$. *Chem. Mater* **2017,** *29* (18), 7961-7968.

89. Wang, C.; Xie, H.; Zhang, L.; Gong, Y.; Pastel, G.; Dai, J.; Liu, B.; Wachsman, E. D.; Hu, L., Universal Soldering of Lithium and Sodium Alloys on Various Substrates for Batteries. *Adv. Energy Mater.* **2017,** *8* (6), 1701963.

90. Liu, B. Y.; Gong, Y. H.; Fu, K.; Han, X. G.; Yao, Y. G.; Pastel, G.; Yang, C. P.; Xie, H.; Wachsman, E. D.; Hu, L. B., Garnet Solid Electrolyte Protected Li-Metal Batteries. *ACS Appl. Mater. Interfaces* **2017,** *9* (22), 18809-18815.

91. Fu, K. K.; Gong, Y. H.; Liu, B. Y.; Zhu, Y. Z.; Xu, S. M.; Yao, Y. G.; Luo, W.; Wang, C. W.; Lacey, S. D.; Dai, J. Q.; Chen, Y. N.; Mo, Y. F.; Wachsman, E.; Hu, L. B., Toward garnet electrolyte-based Li metal batteries: An ultrathin, highly effective, artificial solid-state electrolyte/metallic Li interface. *Sci. Adv.* **2017,** *3* (4), 11.

92. Zhou, C.; Samson, A. J.; Hofstetter, K.; Thangadurai, V., A surfactant-assisted strategy to tailor Li-ion charge transfer interfacial resistance for scalable all-solid-state Li batteries. Sustainable Energy Fuels **2018**, *2*, 2165.

93. Geiger, C. A.; Alekseev, E.; Lazic, B.; Fisch, M.; Armbruster, T.; Langner, R.; Fechtelkord, M.; Kim, N.; Pettke, T.; Weppner, W., Crystal Chemistry and Stability of "$Li_7La_3Zr_2O_{12}$" Garnet: A Fast Lithium-Ion Conductor. *Inorg. Chem.* **2011,** *50* (3), 1089-1097.

94. Shimonishi, Y.; Toda, A.; Zhang, T.; Hirano, A.; Imanishi, N.; Yamamoto, O.; Takeda, Y., Synthesis of garnet-type $Li_{7-x}La_3Zr_2O_{12-1/2x}$ and its stability in aqueous solutions. *Solid State Ionics* **2011,** *183* (1), 48-53.

Appendix: Copyrights

Copyright Clearance Center RightsLink®

Home | Account Info | Help

Title: Present understanding of the stability of Li-stuffed garnets with moisture, carbon dioxide, and metallic lithium

Author: Kyle Hofstetter,Alfred Junio Samson,Sumaletha Narayanan,Venkataraman Thangadurai

Publication: Journal of Power Sources

Publisher: Elsevier

Date: 30 June 2018

© 2018 Elsevier B.V. All rights reserved.

Logged in as:
Kyle Hofstetter
Account #:
3001260248

LOGOUT

Please note that, as the author of this Elsevier article, you retain the right to include it in a thesis or dissertation, provided it is not published commercially. Permission is not required, but please ensure that you reference the journal as the original source. For more information on this and on your other retained rights, please visit: https://www.elsevier.com/about/our-business/policies/copyright#Author-rights

BACK | CLOSE WINDOW

Copyright © 2018 Copyright Clearance Center, Inc. All Rights Reserved. Privacy statement. Terms and Conditions.
Comments? We would like to hear from you. E-mail us at customercare@copyright.com

ECS Copyright and Permissions

NOTICE: Beginning Monday, April 10, 2017, ECS has partnered with the Copyright Clearance Center (CCC) in order to manage permission requests.

- This service will allow authors to immediately receive permission, and will eliminate the need to complete ECS's permission request form.
- As of Monday, April 10, 2017, ECS will no longer accept permission request forms through email. All future requests must be made through CCC.
- Please note that there may be fees involved, depending on the type of material and reuse requested.
- **As has always been ECS's policy, authors are NOT required to request permission to reproduce their own figures or tables.**

Before requesting permission, please confirm the open access status of the article. **ECS does not hold the copyright on the open access articles published in its journals.** Please follow reuse instructions given by Creative Commons for its various licenses.

Copyright Clearance Center RightsLink®

Home | Create Account | Help

Title: Characterization of lithium-rich garnet-type Li6.5La2.5Ba0.5ZrTaO12 for beyond intercalation chemistry-based lithium-ion batteries

Author: Kyle Hofstetter,Alfred Junio Samson,Venkataraman Thangadurai

Publication: Solid State Ionics

Publisher: Elsevier

Date: May 2018

© 2017 Elsevier B.V. All rights reserved.

LOGIN

If you're a copyright.com user, you can login to RightsLink using your copyright.com credentials.

Already **a RightsLink user** or want to learn more?

Please note that, as the author of this Elsevier article, you retain the right to include it in a thesis or dissertation, provided it is not published commercially. Permission is not required, but please ensure that you reference the journal as the original source. For more information on this and on your other retained rights, please visit: https://www.elsevier.com/about/our-business/policies/copyright#Author-rights

BACK | CLOSE WINDOW

Copyright © 2018 Copyright Clearance Center, Inc. All Rights Reserved. Privacy statement. Terms and Conditions.
Comments? We would like to hear from you. E-mail us at customercare@copyright.com